Methods to extract and quantify retinal blood vessels and optic nerve head from optical coherence tomography data in neurological disorders

by

Ella Maria Kadas

A dissertation submitted to the Fachbereich Mathematik und Informatik, Freie Universität Berlin in partial fulfillment of the requirements for the degree of doctor rerum naturalium

– Dr. rer. nat. –

Defended April 19, 2016

Freie Universität Berlin

Referees:

Prof. Dr. Konrad Polthier, Freie Universität Berlin

Prof. Dr. Ingrid Hotz, Linköping University Sweden

Abstract

The eye's retina is considered to be part of the central nervous system with similar structure and cellular composition like the brain. Thus, it has gained an important role in identifying structural changes that provide useful diagnostic information in many neurological disorders. Over the last decade, innovative advances in optical imaging technology have allowed us to identify these changes in the retinal architecture. Especially optical coherence tomography (OCT) has become a powerful imaging modality in ophthalmology and vision science. OCT non-invasively acquires in micrometer resolution, three-dimensional (3D), cross-sectional images of biological tissues in vivo, producing in-depth views of the retina. With the 3D data sets, we can use 3D modeling, and detection tools to allow more intuitive visualization and quantification of the structure in the data set, similar to the 3D tools created for magnetic resonance imaging or computed tomographic scans.

However, current OCT technology being mainly applied in the analysis and quantification of ophthalmological diseases, lacks tailored image analysis methods for many changes caused by neurological disorders. The focus of this thesis lies on the development of segmentation and analysis methods to quantify two major components of the retina in confocal scanning laser ophthalmoscopy (cSLO data - 2D image) and in OCT data (3D OCT volume data), the retinal blood vessels, and the optic nerve head (ONH). The difficulty in developing robust and accurate methods for detecting these structures consists in the heterogeneous aspect of the data, coming from the natural anatomical diversity of the subjects, artifacts during data acquisition, especially in patients rather than in data from healthy control, and most importantly from certain structural changes that occur in the data during the disease course.

We present four approaches for extracting features from the retinal vasculature and for the ONH in multiple sclerosis (with its subtypes), neuromyelitis optica spectrum disorder and idopathic intracranial hypertension. The first two approaches focus on the detection of the vasculature in SLO images. We propose a new 2D model of the vessel profile that accounts for the central reflex seen in this particular image type in order to quantify the vessel inner and outer boundary. Furthermore we developed new filter response measures for vessel enhancement based on Morlet wavelet, the Hessian tensor, and an optimal oriented flux approach, and tested their capability of correctly detecting the vessel inner and outer boundary, curvature especially in junction regions. In case of the ONH, we present a robust approach in detecting a reference surface for the volume computation in atrophic and swelled ONH. Moreover, we present a novel algorithm for the detection of the ONH center directly in the 3D OCT volume. The basic idea of this method is to use the information from the computed reference surface to reduce the computation to a sub-volume (a reduced volume) in the ONH region. Furthermore we address several challenges present in our data: motion artifacts due to eye/head movements by using a modified thin plate spline fitting that is able to model the natural curvature of the retina, artifacts arising from the shadows created by the presence of blood vessel by incorporating contextual textural features in a 3D grow-cut setting.

We evaluate our methods in various clinical settings. To demonstrate the effectiveness of our novel methods, we applied them on various patient and healthy control datasets.

Acknowledgements

First, I would like to thank my academic adviser, Prof. Dr. Konrad Polthier, for guiding this work and sharing his expertise, but also for his support throughout the years. I thank Prof. Dr. Ingrid Hotz for refereeing and for the constructive comments. I would also like to thank Alexander U. Brandt, head of the Neurodiagnostic Laboratory for giving me the opportunity to work in this exciting research area and for providing an excellent research environment. His energy and creative thoughts have encouraged me to try new approaches even when one seemed to have reached a dead end. Also I would like to thank Prof. Friedemann Paul, head of AG Paul, NeuroCure Clinical Research Center at Charité University Berlin for sharing his medical knowledge.

I am grateful for having written this thesis in a dynamic team with wonderful colleagues and for their invaluable advise and constant support, but also for their friendship and the experiences we have shared even outside work. I am particularly grateful to Hanna Zimmermann, Timm Oberwahrenbrock, Sebastian Papazoglou for their invaluable advises and constant support, their inspiring discussions, constructive and critical remarks and most of all for their patience. I have learned and benefited so much from members of our Neurodiadnostic Laboratory that is constantly growing, and I am happy to have the opportunity to continue working with them. I want to also thank Anna Wawrzinek and Ulrich Reitebuch, Christoph von Tycowicz and Christian Schulz, members of the mathematical geometry processing group for their collaboration and helpful suggestions.

Finally, I would like to give special thanks to my family for their support and love throughout this work.

Contents

List of Abbreviations

BM	Bruch's Membrane
BMO	Bruch's Membrane Opening
CCSVI	Chronic Cerebrospinal Venous Insufficiency
CIS	Clinical Isolated Syndrome
CLAHE	Contrast Limited Adaptive Histogram Equalization
CNS	Central Nervous System
DG	Dual-Gaussian
FDOG	First-Order Derivative Of Gaussian
GEE	Generalized Estimation Equation
GCIPL	Ganglion Cell and Inner Plexiform Layer
ICC	Intraclass Correlation Coefficient
IIH	Idopathic Intracranial Hypertension
ILM	Inner Limiting Membrane
INL	Inner Nuclear Layer
HRT	Heidelberg Retina Tomograph
IS/OS	Inner Segments - Outer Segments Junction
MF	Matched Filter
MS	Multiple Sclerosis
MW	Multiple Wavelet
NCO	Neural Canal Opening
NMOSD	Neuromyelitis Optica Spectrum Disorder
OCT	Optical Coherence Tomography
ON	Optic Neuritis
ONH	Optic Nerve Head
ONHH	Optic Nerve Head Height

ONHV	Optic Nerve Head Volume
ONL	Outer Nuclear Layer
OOF	Optimal Oriented Flux
OP	Orientation Pyramid
OPL	Outer Plexiform Layer
PPMS	Primary Progressive Multiple Sclerosis
RPE	Retinal Pigment Epithelium
ROI	Region Of Interest
RNFL	Retinal Nerve Fiber Layer
RRMS	Relapsing Remitting Multiple Sclerosis
SDOCT	Spectral Domain Optical Coherence Tomography
SMF	Sub-band Multiresolution Filtering
SPMS	Secondary Progressive Multiple Sclerosis
TMV	Total Macular Volume
TPS	Thin Plate Spline

Chapter 1

Introduction

Medical image analysis is an interdisciplinary field of science. Therefore, research questions always arise from two different perspectives: from the clinician's point of view, that has specific questions about a certain disease and needs quantifiable measures extracted from the image data for further comparison with other clinical parameters, and the algorithmic side, that is concerned with specific technical problems. This thesis deals with segmentation and analysis of three-dimensional (3D) spectral domain optical coherence tomography (SDOCT) data and two-dimensional (2D) confocal scanning laser ophthalmoscopy (cSLO) data of the retina. We propose four algorithms to extract structures of the retina. These comprise the blood vessels, the inner limiting membrane (ILM), the retinal pigment epithelium (RPE) and the optic nerve head (ONH) center. The choice of these specific structures was motivated by the need of automated tools for the analysis of the changes that the retina might undergo under the effect of neurological disorders. The difficulty in developing robust and accurate methods for detecting these structures consists in the heterogeneous aspect of the data, coming from the natural anatomical diversity of the subjects, artifacts during data acquisition, especially in patients compared to data from healthy controls, and most importantly from certain structural changes that occur in the data during the disease course. Especially these later changes represent the greatest challenge in the algorithm developing process, as assumptions about the data in healthy subjects no longer hold and the patterns seen are difficult to model. The goal of this chapter is to motivate our research, and to list our main contributions. Finally, an overview of the whole thesis is given.

1.1 Motivation

The eye's retina is formed during embryogenesis from neural tissue and can thus be considered part of the central nervous system (CNS) with similar structure and cellular composition like the brain [Purves et al., 2001].

Over the last decade, innovative advances in ocular imaging technology have allowed us to identify structural changes in the retinal architecture that correlate with tissue-specific mechanisms of the CNS. Especially SDOCT has become a powerful imaging modality in ophthalmology and vision science. SDOCT non-invasively acquires high-resolution, 3D, cross-sectional images of biological tissues in vivo, producing in-depth views of the retina. However, with optical coherence tomography (OCT) being originally an ophthalmo-logic tool, most research and developed imaging algorithms have been performed in ophthalmology with the focus on different anatomical changes, which are not or only in part applicable to neurological disorders. Also, the majority of studies has been done when OCT was still a 2D technique. There are two main structures that will be the focus of this research project: the retinal blood vessel network and the ONH.

Retinal blood vessel segmentation

The motivation for segmentation and analysis of the retinal blood vessel network has two components, a medical one, and a technical one. There has been extensive work on retinal blood vessel segmentation based on fundus photography [Chaudhuri et al., 1989, Gang et al., 2002, Hoover et al., 2000, Soares et al., 2006, Sofka and Stewart, 2006, Staal et al., 2004, Zhang et al., 2015]. The characteristics of vessels play an important role in a variety of medical diagnoses in ophthalmology with a special focus on diabetic retinopathy, a severe disease which causes blindness among working age people [Franklin and Rajan, 2014]. Also, new studies have shown that retinal vascular caliber has been linked with increased cardiovascular risk and is predictive of cardiovascular pathology, including stroke and coronary heart disease [Sun et al., 2008]. Despite these results, little is known about vascular retinal changes in neurological disorders. Therefore, one aim of the research is to develop specialized image segmentation techniques to detect the retinal vasculature and analyze the different parameters extracted from this structure in neurological disorders.

Furthermore, cerebral veins gained increasing attention in the treatment of multiple sclerosis (MS). A concept termed chronic cerebrospinal venous insufficiency (CCSVI) was introduced suggesting that compromised cerebral venous outflow might contribute to MS pathology [M. and Z., 2012]. However, several studies could not confirm cerebro-cervical venous congestion, but instead showed either normal or reduced veins compared to healthy subjects [Diaconu et al., 2012]. Yet, little is known about retinal veins in MS to support or object the CCSVI hypothesis.

The technical aspect focuses on the detection of retinal blood vessels to be further used as landmarks for the analysis of other anatomical structures in the retina, as for example the ONH region. Unlike the brain cortical surface, the surface of the ONH region presents no known folds or visible landmarks [Gibson et al., 2010]. Therefore, the identification of specific topographic features and local shape structures such as blood vessels is a key prerequisite to obtain anatomically meaningful registrations for further analysis.

ONH volume computation

The ONH is the retina's central structure where all nerve fibers converge and form the optic nerve connecting the retina with the visual brain areas. It is a prime target for structural changes both in the form of swelling and destruction.

With OCT being originally a mainly ophthalmologic tool, most ONH research has been performed in opthalmological diseases like glaucoma. Glaucoma is the second-leading cause of blindness characterized by gradual damage to the optic nerve and resultant visual field loss. The hallmark of glaucoma is cupping of the optic disc, which is the visible manifestation of the ONH 3D structure [Abràmoff et al., 2010]. In neurological disorders like multiple sclerosis or neuromyelitis optica spectrum disorders, neuroinflammatory diseases, acute optic neuritis (ON) is a characteristic or even crucial manifestation of the disease [Zimmermann et al., 2014]. ON is an inflammatory attack to the optic nerve. After initial swelling due to edema in the acute phase, degeneration of the retina occurs [Balcer, 2006, Schneider et al., 2013]. A case of extreme swelling of the ONH occurs in idiopathic intracranial hypertension (IIH), which can lead to vision loss.

Only recently 3D ONH imaging became available, opening ONH investigation for changes in neurological disorders. While stereo fundus photography provides the ability to extract some

3D shape information of the ONH [Juan et al., 2010], only SDOCT provides true 3D information [Abràmoff et al., 2009, Bhavna et al., 2014, Hu et al., 2010a]. These studies focus on different anatomical changes, which are not or only in part applicable to neurological disorders. Thus, current methods regularly fail when applied in neurological conditions like ONH swelling. Our main goal was to segment the RPE, that provides a reference surface for the ONH volume, as well as the ONH center computation. When specific image analysis methods are potentially available for neurological disorders, retinal OCT imaging can become a powerful tool as "window to the brain” in many neurological disorders. The applications range from initial differential diagnosis of several neurologic conditions, longterm control of changes, to therapy monitoring. Consequently, this scientific field is currently highly dynamic and covers many relevant neurological disorders.

1.2 Summary of main achievements

Our objective in this work is to build a framework of methods to extract features from the retinal vasculature from 2D cSLO data and for the ONH in 3D SDOCT data. These methods should be specially tailored for neurological disorders like MS (with its subtypes), neuromyelitis optica spectrum disorder (NMOSD) and IIH. In our research the following objectives were obtained:

- **Detection of blood vessel inner and outer diameter in cSLO images presented in Section 3.2**
  We developed a tool to extract the diameter of blood vessels in order to investigate differences in patients with MS compared to healthy control (HC), and to test the hypothesis of CCSVI in the retinal vasculature. Vessels in the cSLO image, unlike fundus photographs present a strong central reflex. To correctly identify the vessel we constructed a 2D model of the vessel profile. Furthermore we incorporated this method in a semi-automated tool for the use in a clinical study.

- **Detection of the entire blood vasculature in cSLO images presented in Section 3.3**
  The retinal vessel network can serve as a map of landmarks for further analysis of the ONH, and for registration for follow-up scans. In order to detect the whole vessel network we derived different *vesselness* filters, a notion introduced by [Frangi et al., 1998] to

denote filters that enhance vessels, and improved some existing techniques, for enhancing tubular structures. We defined more adequate enhancing measures by incorporating information about the vessel directionality and diameter in a multi-scale setting.

- **RPE lower boundary segmentation for ONH volume computation presented in Chapter 4**

  RPE lower boundary can serve as a reliable reference surface for ONH volume computation. Thus we developed an automatic segmentation approach for computing ONH volume from 3D SDOCT scans that is robust and applicable in healthy, but most importantly in swelled ONH. In the case of extreme swelling like in IIH data, RPE detection can become extremely challenging as ONH OCT scans tend to have regions of strong varying intensity values caused by the edema. Additionally, scans are characterized by an increased intrinsic speckle noise making a reliable differentiation of intraretinal layers challenging to impossible.

- **Bruch's membrane opening points detection for ONH center and ONH volume computation presented in Chapter 5**

  Bruch's membrane opening (BMO) points were shown to provide reliable landmarks even in case of strong changes in the ONH structure. Therefore we developed a fully automated BMO points detection algorithm that is tailored to detect ONH features in very heterogeneous data directly in the 3D volume. We address several major challenges present in our data: motion, distortions artifacts due to eye/head movements but more important anatomical structure modifications due to atrophy or swelling. To this end, we developed a two-stage thin-plate spline fitting (TPS). By deriving a modified multi-scale wavelet filter, we suppressed the shadows artifacts produced by the presence of vessels. In contrast to previous methods that use characteristics of data of glaucomatous eyes (atrophic ONH), our approach is able to handle atrophic, normal and swelled ONH. In particular, we devised reliable features by combining texture analysis in the context of a sub-band filtering technique and integrate this hybrid analysis in a 3D grow-cut based segmentation setting.

1.3 Publications

The content of this thesis builds on the following papers:

Ella Maria Kadas, Falko Kaufhold, Christian Schulz, Friedemann Paul, Konrad Polthier and Alexander U. Brandt,
3D optic nerve head segmentation in idiopathic intracranial hypertension,
Bildverarbeitung für die Medizin 2012, Informatik aktuell, pages 262-267, 2012.

Falko Kaufhold, Ella Maria Kadas, Christoph Schmidt, Hagen Kunte, Jan Homann, Hanna Zimmermann, Timm Oberwahrenbrock, Lutz Harms, Konrad Polthier, Alexander U. Brandt and Friedemann Paul,
Segmentation of the optic disc in 3D oct scans of the optic nerve head,
PLoS ONE, Jan. 2012.

Philipp Albrecht, Christine Blasberg, Sebastian Lukas, Marius Ringelstein, Ann-Kristin Müller, Jens Harmel, Ella Maria Kadas, David Finis, Rainer Gutho, Orhan Aktas, Hans-Peter Hartung, Friedemann Paul, Alexander U. Brandt, Peter Berlit, Axel Methner and Markus Krälmer,
Retinal pathology in idiopathic moyamoya angiopathy detected by optical coherence tomography,
Neurology, Apr. 2015.

and several posters:

Ella Maria Kadas, Timm Oberwahrenbrock, Hanna Zimmermann, Sebastian Papazoglou, Friedemann Paul, Konrad Polthier and Alexander U. Brandt,
Quantification of retinal vessels in multiple sclerosis,
ECTRIMS European Committee for treatment and research in multiple sclerosis conference (ECTRIMS Congress Lyon 2012).

Ella Maria Kadas, Janine Mikolajczak, Wolf Lagreze, Hanna Zimmermann, Friedemann Paul and Alexander U. Brandt,
Robust optic nerve head analysis based on 3d optical coherence tomography,
NANOS North American Neuro-Ophthalmology society (NANOS Congress San Diego 2015).

Hanna Zimmermann, Ella Maria Kadas, Alina Freing, Falko Kaufhold, Friedemann Paul and Alexander U. Brandt,
Characterizing neuronal damage in multiple sclerosis using optic nerve head volume,
ECTRIMS European Committee for treatment and research in multiple sclerosis (ECTRIMS Congress Lyon 2012).

Hanna Zimmermann, Ella Maria Kadas, Timm Oberwahrenbrock, Friedemann Paul and Alexander U. Brandt,
Optic nerve head volume as a marker for neuronal damage after optic neuritis in multiple sclerosis and neuromyelitis optica ,
ACTRIMS American Committee for treatment and research in multiple sclerosis-ECTRIMS European Committee for treatment and research in multiple sclerosis (MS Boston Congress 2014).

1.4 Overview of the thesis

This thesis is structured in 7 chapters, where:

- In Chapter 2 we introduce the mathematical and computational background used and adapted in our algorithms. Also, the background information regarding the anatomy of the anterior visual system is presented, explaining the role of the retina and its connection to the brain as part of the central nervous system in vision. We also discuss the structures of the retina and their changes and characteristics in neurological disorders. The blood vessels and the ONH are two components of the retina that are studied in this work. The different imaging techniques to visualize these components are presented, with special focus on optical coherence tomography, that constitutes the technique used in this research.

- In Chapter 3 we present the two algorithms used for the retinal blood vessel detection. In Section 3.2, we describe a semi-automated algorithm for the detection of retinal vessel diameter, validate and evaluate the measurements obtained with our algorithm in a clinical study with MS and HC data. In Section 3.3 we present three approaches developed to detect the entire retinal vasculature, and compare their performance.
- In Chapter 4 we present a robust method for detecting a reference surface for optic nerve head volume computation even in the case of extremely swollen optic nerve head.
- In Chapter 5 we describe methods for the ONH volume computation derived from the detection of the ONH center, that is tailored to account for various characteristics in several neurological disorders.
- In Chapter 6 we discuss the advantages, performance and drawbacks of the algorithms developed and compare them to previous methods.
- In Chapter 7 we summarize concluding remarks and possible future avenues of research.

Chapter 2

Background

In this chapter we introduce mathematical and computational key concepts that were modified and adapted in the development of our approaches to extract the retinal blood vessel profile, the entire retinal vasculature, and to compute the ONH volume. Also several anatomical structures are presented in order to understand the role of the retina in the visual system, as well as its connection to the central nervous system. We also briefly describe the retinal anatomy, with the focus on the retinal blood vessels and the ONH, as these structures represent the main features that we extract and analyze in our research. There are several imaging techniques that are extensively used mainly in ophthalmology to visualize the structures previously mentioned. We describe some of these techniques in order to understand previous approaches that have been proposed for the analysis of the retinal blood vessels, ONH, and retinal layers. Especially SDOCT with its capability of acquiring high-resolution, 3D, cross-sectional images of the retina, has become a powerful imaging modality in ophthalmology and vision science, and is the imaging technique used in our studies. As we are interested in analyzing the blood vessels, and the ONH in neurological disorders, we describe important characteristics of the retina in MS, NMOSD and IIH. Also we present important OCT parameters for the retina and its changes that have been established in previous studies.

2.1 Computational and mathematical approaches for retinal feature extraction

This section introduces mathematical and computational concepts that were modified and adapted in the development of our approaches to address different technical aspects when segmenting the retinal blood vessel, the RPE lower boundary and the BMO points (the last two structures both employed in ONH volume computation).

2.1.1 Basics and Notations

I represents a n-dimensional gray scale image $I{:}\Omega \rightarrow \mathbb{R}$, with the image domain $\Omega \subset \mathbb{R}^n$. Vectors, and vector-valued functions are represented by bold lower-case letters, i.e. $\boldsymbol{v}$ and $\boldsymbol{v}(\boldsymbol{x})$. $\boldsymbol{v}^{\boldsymbol{T}}$ denotes the transpose of vector $\boldsymbol{v}$.

Scalar fields

A scalar field is defined as a map $s(\boldsymbol{x})$, $\boldsymbol{x} \in \Omega$ that assigns a scalar to each point in the domain Ω.

Vector fields

A vector field is defined as a map $\boldsymbol{v}(\boldsymbol{x})$, $\boldsymbol{x} \in \Omega$, that assigns an n-dimensional vector $\boldsymbol{v} = (v_1, ..., v_n)^T$ to each point in the domain Ω. Unless normalized, vectors encode a direction and a magnitude. The gradient of a smooth scalar field $s(\boldsymbol{x})$ is defined by the first order spatial derivative of the scalar field. It is given by

$$\nabla s = \left(\frac{\partial s}{\partial x_1}, ..., \frac{\partial s}{\partial x_n} \right), \tag{2.1}$$

where $\frac{\partial s}{\partial x_i}$ denotes the partial derivative in the ith component of $\boldsymbol{x}$. The gradient points towards the direction of strongest change in the scalar field. Divergence of a n-dimensional vector field $\boldsymbol{v}(\boldsymbol{x})$, with $n \in \{2, 3\}$, can be defined as

$$\text{div } \boldsymbol{v} = \sum_1^n \frac{\partial v_i}{\partial x_i}. \tag{2.2}$$

If a flow field $\boldsymbol{v}(\boldsymbol{x})$ is considered as transporting mass then a positive divergence value at a specific location can be interpreted that mass spreads outward from that point. A negative divergence value indicates a sink location and zero divergence that mass is transported with neither loss nor gain. A vector field that is divergence free has neither sources nor sinks of mass.

Tensors

Tensors are multi-linear mappings that generalize and extend the concept of scalars, vectors and matrices. In fact, tensors of order zero are scalars and tensors of order one are vectors. Tensors are independent of specific reference frames, that is, they are invariant under coordinate transformations. More precisely, the tensor components change according to the transformation into another basis but the characteristics of the tensor are preserved. Consequently, tensors can be analyzed using any convenient reference frame. In this thesis we deal only with tensors up to order two. Order two tensor allows to encode anisotropic properties which vary as function of direction. In computer science mostly tensors using the indicial notation appear. Thus a second order tensor $T \in \mathbb{R}^{n \times n}$ can be represented by a $(n \times n)$ square matrix T. However, it requires a fixed coordinate basis. Generally, in this case the tensor is represented with respect to a specific Cartesian basis, thus uniquely defined by its components and represented as a matrix. For a two dimensional tensor, this leads to a 2×2 matrix representation:

$$T = \begin{pmatrix} T_{11} & T_{12} \\ T_{21} & T_{22} \end{pmatrix} \tag{2.3}$$

Given a tensor T in indicial notation, T is called

- symmetric if $T_{ij} = T_{ji}$
- asymmetric if $T_{ij} \neq T_{ji}$
- anti-symmetric or skew-symmetric if $T_{ij} = -T_{ji}$

If for all non-zero vectors $\boldsymbol{v}$

- if $\boldsymbol{v^T} T \boldsymbol{v} > 0$, T is called positive definite
- if $\boldsymbol{v^T} T \boldsymbol{v} \geqslant 0$, T is called positive semi-definite
- otherwise T is called indefinite

Symmetric 2D tensors are defined by the three independent scalars T_{11}, T_{22}, $T_{12} = T_{21}$. For specific reference frames, however, the tensor representation becomes more simple. Symmetric tensors can be represented as diagonal matrices. The basis for such a representation is given by the eigenvectors corresponding to the diagonal matrix. A vector $\boldsymbol{v}$ is called eigenvector of

T according to the eigenvalue λ if $T\boldsymbol{v} = \lambda\boldsymbol{v}$. The eigenvalues are defined as the roots of the characteristic polynomial. The complete transformation of T from an arbitrary basis into the eigenvector basis is given by

$$U^T T U = \begin{pmatrix} \lambda_1 & 0 \\ 0 & \lambda_2, \end{pmatrix} \tag{2.4}$$

where the diagonal elements λ_1, λ_2 are the eigenvalues and U is the orthogonal matrix that is composed of the normalized eigenvectors, $U = (\boldsymbol{v_1}, \boldsymbol{v_2})$.

Symmetric tensors have real eigenvalues, and the normalized eigenvectors constitute an orthonormal basis. The diagonalization is computed numerically via singular value decomposition, or principal component analysis. Positive definite tensors have eigenvalues and a determinant greater than zero. For semi-positive definite tensors the same holds for greater or equal than zero. For indefinite tensors none of these assumptions can be made.

Unless stated differently, eigenvalues are named λ_1, λ_2 and $\boldsymbol{v_1}$, $\boldsymbol{v_2}$ are the corresponding eigenvectors, such that always $\lambda_1 \leq \lambda_2$. Accordingly, λ_1 is referred to as the minor eigenvalue and λ_2 as the major eigenvalue. The eigenvectors represent the directions of maximal and minimal variation encoded by the tensor, the eigenvalues give the maximal magnitude of this variation, sometimes also referred to as amplitude.

Invariants of a tensor are scalar functions of the tensor components which remain constant under a basis change.

- $I_1 = tr(T) = \lambda_1 + \lambda_2$
- $I_2 = \frac{1}{2}(tr(T)^2 - tr(T^2)) = \lambda_1\lambda_2$
- $I_3 = det(T) = \lambda_1\lambda_2$

Flux

The flux of a vector field over the closed boundary of a region is the quantification of the amount of the vectors, which flows into or out of that region along the boundary surface normal direction. Mathematically, in the Euclidean space, the flux of a vector field **v** over the closed boundary of a region S is defined as:

$$F_C = \int_{\partial S} \langle \boldsymbol{v}, \mathbf{n} \rangle \, dA, \tag{2.5}$$

where dA is the infinitesimal area on closed boundary ∂S, $\boldsymbol{n}$ is the outward normal of ∂S. It provides a measure of how well the vector field are aligned with the normal vectors of the surface. By convention positive flux leaves a closed surface, and negative flux enters a closed surface. Inward/Outward flux depends on the sign of $\boldsymbol{n}$.

2.1.2 Scale-space representation of image data

Scale is a very important concept in the human vision. When one looks at a scene, its contents is instantaneously viewed at multiple scales. This fact, that objects appear in different ways depending on the scale they are observed, has an important influence on the process of describing them in the computer vision and image processing context. The content of each pixel or voxel of an image is the result of a physical observation. A key notion is the one of sampling. Each observation is done through a multi-size aperture, where the aperture size is represented by the scale parameter. When analyzing an unknown scene, there is usually no way to *a priori* know what scales are appropriate for extracting the relevant information. The information that can be obtained is determined by the relationship between the size of the structures in the scene and the size (resolution) of the operators applied. Also the questions of what represents *relevant information* and which computation should be done at which scale depends on the goal of the analysis, and its application field.

In order to restrict the space of possibilities, one starts with the assumption that no prior information is available about the objects in the image, namely one considers an "uncommitted vision system" and represents the input data at multiple scales. This involves generating a parameter class of derived signals in which the fine-scale information is sequentially suppressed. One important requirement is that the structures at coarse scales in the multi-scale representation should be derived as simplifications of corresponding structures at finer scales. The new parameter represents the resolution of the image. The stack of images as, see Figure 2.1 is called the scale-space. Scale-space theory offers a solid mathematical framework to model the multi-scale nature of image data [Lindeberg, 1994]. A main result is that convolution by the Gaussian kernel and its derivatives is established as the unique scale-space filter [Lindeberg, 1994].

The derivation of Gaussian scale space has been accomplished in many ways. A fundamental approach has been presented by [Witkin, 1983], discussing the blurring properties of one-dimensional signals. The extension to more-dimensional images was made in 1984 by

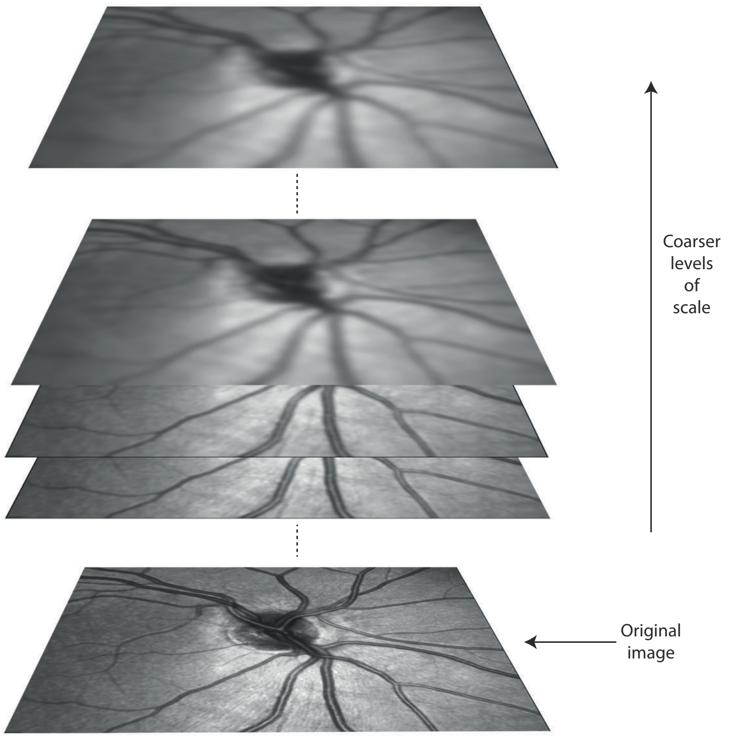

FIGURE 2.1: A multi-scale representation of a signal (image) is an ordered set of derived signals at different levels of scale.

[Koenderink, 1984], who, also, was the one to give the first proof of the necessity of Gaussian smoothing for generating a scale-space representation. He showed that this scale-space representation of images may be viewed as the solution of the diffusion equation. [Koenderink, 1984] motivates the diffusion equation formulation by stating two criteria. *Casuality*: any feature at a coarse level of resolution should be derived from one (or more) at a finer level of resolution, i.e, "no spurious features" should be generated when the resolution is reduced. The reverse doesn't need to be true. *Homogeneity and isotropy*: The blurring is required to be space invariant.

[Lindeberg, 1994] considered those kernels in one dimension that share the property of not introducing new local extrema under convolution. In order to show that these kernel are represented by the Gaussian, he combined the semi-group structure with additional conditions: "the non-creation of local extrema", the existence of a continuous scale parameter and, the kernels are required to be symmetric and satisfy smoothness in the scale direction.

Although these two works are the start of scale-space theory in the Western literature the idea was already twenty years old. The Japanese Taoizo Iijima, as [Weickert et al., 1999] presented, wrote a paper deriving the Gaussian as unique filter.

In the following we present the motivation of using Gaussian smoothing based on work presented by [Florack, 1993]. In his approach an image is just a physical observation of a scene of the real world. Local image structure depends on resolution. The smallest scale of interest will be called the *"inner scale"*, whereas the largest scale of interest will be called the *"outer scale"*. The *"inner scales"* are limited to a finite range determined by the resolution of the sampling device (grid size) and by the field of view. If we consider additional constraints (stated as axioms later in this subsection), one arrives at the Gaussian filter family, as a physical motivation and a mathematical model for multi-scale representation of the data.

Scale and resolution

In his approach I can be interpreted also as the luminance of an observed scene, which has the initial luminance I_0. Consider also σ as the width of the aperture function in the spatial domain, and $\boldsymbol{\omega}$ the spatial frequency vector. Also the physical sampling system should be independent of a particular coordinate system, therefore invariant under orthogonal coordinate transformation: translation and rotation.

Scale space axioms

The requirements of scale space can be stated as axioms. In essence, these represent the mathematical formulation for *uncommittedness*.

- *Spatial shift invariance* means that all locations in the field of view are *a priori* equivalent. So there is no preferred location that should be measured differently.
- *Spatial isotropy* indicates that there is no *a priori* preferred orientation, horizontal and diagonal structures are measured equally.
- *Spatial scale invariance* does not differentiate between objects of different size.
- *Linearity* signifies that there is no preferred way to combine observations.

Linear shift invariance implies that a rescaled image must be a convolution of the original image by some kernel $G(\boldsymbol{x};\sigma)$:

$$I(\boldsymbol{x};\sigma) = \{I_0 * G(\boldsymbol{x};\sigma)\}(\boldsymbol{x};\sigma), \tag{2.6}$$

$*$ is defined as the convolution operation for two arbitrary functions f and g

$$f * g = \int_{-\infty}^{\infty} f(u)g(x-u)du. \tag{2.7}$$

In the Fourier domain convolution becomes multiplication

$$I(\boldsymbol{\omega};\sigma) = I_0(\boldsymbol{\omega}) \cdot \widehat{G}(\boldsymbol{\omega};\sigma). \tag{2.8}$$

The *Pi Theorem*, see [Florack, 1993] for details, states that, because of scale invariance, there are only two independent dimensionless variables in this case. These can be chosen to be $\widehat{G} = \frac{I}{I_0}$ and $\boldsymbol{\Omega_\omega} = \sigma\boldsymbol{\omega}$. Then, according to the *Pi Theorem* $\widehat{G}(\boldsymbol{\omega};\sigma) = \frac{I}{I_0} = \widehat{G}(\boldsymbol{\Omega_\omega})$.

Spatial isotropy implies that $\widehat{G}$ depends only on the magnitude (Euclidean length) of the vector $\boldsymbol{\Omega_\omega}$, so $\widehat{G}(\boldsymbol{\Omega_\omega}) = \widehat{G}(\Omega)$. σ is chosen such that, for a fixed ω, the hypothetical zero-scale limit will leave the initial image unscaled, so

$$\lim_{\Omega \to 0} \widehat{G}(\Omega) = 1. \tag{2.9}$$

Also it is required that the infinite-scale limit gives a complete spatial averaging of the initial image

$$\lim_{\Omega \to \infty} \widehat{G}(\Omega) = 0. \tag{2.10}$$

Performing several rescalings successively should be consistent with performing a single rescaling. More specifically if σ_1, σ_2 are the scale parameters associated with two rescalings $\widehat{G}(\Omega_1)$, $\widehat{G}(\Omega_2)$ respectively, then the concatenation of these should be a rescaling $\widehat{G}(\Omega_3)$ corresponding to a scale parameter $\sigma_3 = \sigma_1 \oplus \sigma_2$. This means that the observation increases the *inner scale* and the total scaling must be consistent with performing just a single rescaling. The operator $\oplus$, with the group of positive real numbers, $\left\{\mathbb{R}_0^+;\oplus\right\}$, constitute a *commutative semi-group*. A result from the theory of semi-groups is that, see [Florack, 1993]

$$\widehat{G}(\Omega_1)\widehat{G}(\Omega_2) = \widehat{G}\left[(\Omega_1 + \Omega_2)^p\right]. \tag{2.11}$$

A general solution to this constraint is

$$\widehat{G}(\Omega) = exp\left[(\alpha\Omega)^p\right]. \tag{2.12}$$

To single out a unique scale-space kernel a final constraint on the parameter p is set. It is required that the D spatial dimension to be separable

$$\widehat{G}(\Omega) = \coprod_{i=1}^{D} \widehat{G}(\Omega_i), \tag{2.13}$$

in which Ω_i is given by the magnitude of the projection vector $(\boldsymbol{\Omega_\omega} \cdot \widehat{e_i})\widehat{e_i}$. This makes σ to a real length, so we are able to determine σ from scalings along the coordinate axes because an isotropic rescaling can be obtained either directly through $\widehat{G}(\Omega)$ or through a concatenation of rescalings $\widehat{G}(\Omega_i)$ by the same amount in each of the independent spatial directions $\widehat{e_i}$, $i = 1...D$ separately. The separability requirement fixes $p = 2$ because the length of the total projection vector is calculated by the Pythagoras formula from the magnitude of the constituent projection vectors $(\boldsymbol{\Omega_\omega} \cdot \widehat{e_i})\widehat{e_i}$. A convenient choice for is $\alpha^2 = -\frac{1}{2}$ if we want a real solution, so α^2 is real. Additionally from Equation 2.10 α^2 is negative. So finally we get the Gaussian kernel in the Fourier domain

$$\widehat{G}(\Omega) = exp(-\frac{1}{2}\Omega^2), \tag{2.14}$$

which is in the spatial domain

$$G(\boldsymbol{x};\sigma) = \frac{1}{\sqrt{2\pi\sigma^2}} exp\left(\frac{\boldsymbol{x}\cdot\boldsymbol{x}}{2\sigma^2}\right). \tag{2.15}$$

Gaussian derivatives

The Gaussian kernel is now established as the unique scale-space operator to change scale. One of the most useful results in linear scale-space theory is that the spatial derivatives of the Gaussian, together with the zero-*th* order Gaussian form a complete family of differential operators [Florack, 1993]. If we want to take the derivative of an observed image, i.e the convolution of the image with the Gaussian function, we get the following result due to the fact that we can commute the differential and the convolution operators

$$\frac{\partial}{\partial x}(I * G) = I * \frac{\partial G}{\partial x}. \tag{2.16}$$

This means that the derivative is given at a given scale. Thus, in order to differentiate discrete data, the *inner scale* is increased. This is a consequence of the *regularization* of the differentiation process. *Regularization* is the technique to make data “behave well“ when an operator is applied to it. The data could e.g. be functions, that are impossible or difficult to differentiate, or discrete data where a derivative seems to be not defined at all. In our case the discrete image is the distribution and the test function is the infinitely differentiable Gaussian kernel. Differentiation is now done by integration, i.e., by the convolution integral. It may be counterintuitive to perform a blurring operation when differentiating, but differentiation always involves some blurring. It is important to notice that the operator is regularized, not the data.

The human visual system samples the outside world on multiple scales. On the retina lie receptive fields, groups of receptors assembled in such a way that they form a set of apertures of widely varying size. Neurophysiological studies by [Young, 1987] have shown that there are receptive field profiles in the mammalian retina and visual cortex, which can be well modeled by superpositions of Gaussian derivatives.

Nonlinear scale-space

In the isotropic scale-space all structure is blurred, also the regions of particular interest like edges. In linear scale-space there is no preference: all information is processed in the same way (*uncommitness*). We consider only scale-spaces which preserve the luminance. Then the change of luminance over scale can be expressed as the divergence of a flow, where the flow denoted by F in general is a function of the local image structure given by the gradient. As noted before [Koenderink, 1984] showed that the generating equation of linear scale-space is the linear diffusion equation

$$\frac{\partial I}{\partial s} = \nabla \cdot \nabla I = \Delta I = \frac{\partial^2 I}{\partial x \partial x} + \frac{\partial^2 I}{\partial y \partial y}. \tag{2.17}$$

Note the s in the diffusion equation has the dimension of the squared spatial dimension, so it takes the role of the Gaussian variance. The relation to the standard deviation is $\sigma^2 = 2s$.

If some information of the image (like preserving edges) is incorporated, while keeping the properties of scale-space then it is possible to create the nonlinear scale-space [Nielsen et al., 1996]. There are two essential properties for a multiresolution representation to be a scale-space: the image should be simplified, and it should be possible to establish relations over scale [Florack, 1993]. We give two examples of nonlinear multiresolution representations which have the essential scale-space properties.

Gradient dependent diffusion

This case, where the flow $F = c(\|\nabla I\|)\nabla I$ is some scalar function of the gradient, was first proposed by [Perona and Malik, 1990]. They proposed F to be a decreasing function of the gradient

$$c(\boldsymbol{x}, s) = c(\|\nabla I(\boldsymbol{x}, s)\|) = e^{-\frac{c(\|\nabla I\|)^2}{k^2}}, \tag{2.18}$$

k is a parameter controlling the diffusivity, and s represents the scale(time). So that the nonlinear diffusion equation becomes

$$\frac{\partial I}{\partial s} = \nabla \cdot (c \nabla I). \tag{2.19}$$

In this process the diffusion directions are always collinear to the image gradient ∇I and its perpendicular $\nabla I^{\perp}$.

Tensor dependent diffusion

In this case the flow $F = D(S)\nabla I$ is no longer a function of a scalar entity as above, but a function of a tensor. An example is the structure tensor as given by [Weickert, 1999] in 2D

$$S_0 = G(x, y; \sigma) * \begin{pmatrix} \frac{\partial^2 I}{\partial x^2} & \frac{\partial^2 I}{\partial x \partial y} \\ \frac{\partial^2 I}{\partial y \partial x} & \frac{\partial^2 I}{\partial y^2} \end{pmatrix}, \tag{2.20}$$

where σ is called the integration scale. This tensor captures the orientation of the local structure, when integrated over the volume determined by the integration scale. The eigenvectors of this tensor give the principle directions of the structure. A diffusion tensor D which is a function of the structure tensor S can be designed such that diffusion is done along edges and not across them, as it will be explained in detail in Subsection 2.1.3.

2.1.3 Coherence enhancing diffusion

Structure tensors are matrix representations of partial derivative information. In the field of image processing and computer vision, it is typically used to represent the gradient or "edge" information. It is a more powerful description of local patterns as opposed to the directional derivative, providing a local description of the anisotropy in a neighborhood of an image. A simple structure descriptor is the image gradient. As seen in Subsection 2.1.2 the image gradient of a discrete image I is given by ∇I_σ, the gradient of a Gaussian-smoothed version of I, $I_\sigma = G_\sigma * I$. $*$ denotes the convolution operation and G_σ is a Gaussian kernel with standard deviation σ. At $\boldsymbol{x} = (x, y)^T$ the kernel is given by

$$G_\sigma(\boldsymbol{x}) := \frac{1}{2\pi\sigma^2} e^{\left(-\frac{|\boldsymbol{x}|^2}{2\sigma^2}\right)}, \tag{2.21}$$

where σ denotes the noise scale, and it makes the edge detector ignorant of details smaller than $O(\sigma)$. The magnitude of the gradient, $\|\nabla I_\sigma\|$, reflects the maximum change in pixel values, and the phase $\theta = tan^{-1}\left(\frac{\partial I_\sigma}{\partial x} / \frac{\partial I_\sigma}{\partial y}\right)$ is directed along the orientation corresponding to the maximum change. Although ∇I_σ is useful for detecting edges, it is unsuited for finding isotropic structures, where there is no preferred direction of the gradient. In this case, the magnitude is zero. An example is a black circle on a white background, where we have gradient information, but no preferred phase, it zeros itself out, thus $\|\nabla I_\sigma\| = 0$. The same result is reached if the original input is a uniform region, for example, a region containing the same gray values. Again $\|\nabla I_\sigma\| = 0$ as there is no gradient information.

To make the structure descriptor invariant under sign changes, ∇I_σ is replaced by its tensor product $S_0(\nabla I_\sigma) = \nabla I_\sigma (\nabla I_\sigma)^T$ [Brox et al., 2006]. This matrix is symmetric and positive semi-definite, and its eigenvalues By convolving S_0 component-wise with a Gaussian G_ρ the structure tensor is obtained as

$$S_\rho(\nabla I_\sigma) = G_\rho * (\nabla I_\sigma \nabla I_\sigma^T). \tag{2.22}$$

The structure tensor written in matrix form $S_\rho = \begin{pmatrix} S_{11} & S_{12} \\ S_{21} & S_{22} \end{pmatrix}$ is a symmetric, positive semi-definite matrix, since it results from averaging of symmetric positive semi-definite matrices.

TABLE 2.1: Eigenvalue classification of the structure tensor in 2D images

Condition	Rank(S_ρ)	Description
$\lambda_1 = \lambda_2 = 0$	0	I is constant in the neighborhood ρ.
$\lambda_1 > 0$, $\lambda_2 = 0$	1	I, in the neighborhood ρ varies along the direction $\boldsymbol{v_1}$ and is constant along the direction $\boldsymbol{v_2}$; the gradient of I is always a multiple of $\boldsymbol{v_1}$.
$\lambda_1 > 0$, $\lambda_2 > 0$	2	The gray values change in all directions in the neighborhood ρ; then $\boldsymbol{v_1}$ is the direction that is maximally aligned with the gradient; in the special case when $\lambda_1 = \lambda_2$, we speak of an isotropic gray value structure as it changes equally in all directions.

Gaussian smoothing not only improves the orientation information with regard to noise, but also creates a scale-space with the integration scale ρ. This scale parameter determines the size of the neighborhood considered for the structure analysis. Besides the information on orientation and magnitude of structures, which is already present in the gradient, the structure tensor measures the homogeneity of orientations within the neighborhood of a pixel [Medioni et al., 2000]. This information can be extracted by using the eigendecomposition

$$S_\rho = \begin{bmatrix} \boldsymbol{v_1} & \boldsymbol{v_2} \end{bmatrix} \begin{bmatrix} \lambda_1 & 0 \\ 0 & \lambda_2 \end{bmatrix} \begin{bmatrix} \boldsymbol{v_1} \\ \boldsymbol{v_2} \end{bmatrix}, \tag{2.23}$$

where λ_1, λ_2 are the eigenvalues of S_ρ and $\boldsymbol{v_1}$, $\boldsymbol{v_2}$ are the corresponding eigenvectors. In order to be consistent with the notation introduced by [Weickert, 1999] we consider $\lambda_1 \geq \lambda_2$. These values, λ_1, λ_2 represent the ρ-weighted average of the square of the directional derivative of I_σ along $\boldsymbol{v_1}$, $\boldsymbol{v_2}$ respectively. If we take a close look at the eigenvalues we can distinguish the cases summarized in Table 2.1.

The eigenvector $\boldsymbol{v_2}$ corresponding to the smallest eigenvalue determines the dominant orientation of the local structure, while the trace of S_ρ, $tr(S_\rho) = S_{11} + S_{22}$, determines its magnitude. It is the orientation with the lowest fluctuations, the so called *coherence orientation*. The coherence in 2D image data is often expressed by λ_1/λ_2 or by the measure $(\lambda_1 - \lambda_2)^2$ [Brox et al., 2006], yet also other measures based on the eigenvalues may be reasonable. In this sense the *coherence* is defined as a measure of the relative discrepancy between the two eigenvalues of the tensor. It is an indicator of the degree of anisotropy of the gradient in the window ρ, namely how strongly is it biased towards a particular direction (and its opposite) [Medioni et al., 2000]. For example the expression $(\lambda_1 - \lambda_2)^2$ becomes large for anisotropic structures.

Although structure tensors are applicable to many domains, they have gained a considerable interest in the image processing and computer vision domains. Using gradient-based structure tensors, local patterns of contours and surfaces may be inferred through a diffusion process [Arseneau and Cooperstock, 2006]. We are especially interested in the coherence enhancing diffusion described by [Weickert, 1999], for its capability of enhancing *flow-like* structures.

The goal of anisotropic diffusion filtering is to adapt locally to the data but also to the direction of smoothing. It allows, for example, to smooth along image edges while inhibiting smoothing across edges. The nonlinear diffusion filtering result $u(\boldsymbol{x}, s)$, with a scale parameter $s \geq 0$, of a scalar initial image I is given as the solution of a diffusion equation

$$\frac{\partial u}{\partial s} = \mathrm{div}\ (D \nabla u), \tag{2.24}$$

D denotes the diffusion tensor. I is taken as initial condition,

$$u(\boldsymbol{x}, 0) = I(\boldsymbol{x}) \tag{2.25}$$

and boundary conditions

$$\langle D \nabla u, \boldsymbol{n} \rangle = 0. \tag{2.26}$$

$\boldsymbol{n}$ denotes the outer normal and $\langle ., . \rangle$ the usual Euclidean scalar product.

Flow-like structure enhancement

[Weickert, 1999] derived the diffusion tensor for 2D images based on the eigenvalues of the structure tensor, by requiring that the diffusion should act like a smoothing process mainly along the coherence direction v_2 (with the previous notation) and the smoothing should increase with the coherence $(\lambda_1 - \lambda_2)^2$. Thus D should have the same eigenvectors as the structure tensor, but with eigenvalues defined as

$$\mu_1 := \alpha$$
$$\mu_2 := \begin{cases} \alpha \text{ if } \lambda_1 = \lambda_2 \\ \alpha + (1-\alpha)e^{\frac{-C}{(\lambda_1-\lambda_2)^2}}, \text{ otherwise,} \end{cases} \tag{2.27}$$

with $C > 0$ and a small parameter $\alpha \in (0, 1)$.

Note in flat regions we have $\mu_1 = \mu_2 = \alpha$ and the tensor D is defined to be isotropic. Along the image contours, we have $\mu_1 > \mu_2 > 0$ and D is anisotropic, mainly directed by the smoothed direction $\boldsymbol{v_2}$. This approach significantly improved the smoothing orientation, simultaneously reducing noise. Note also that the anisotropic diffusion has been defined as the case where the diffusivity is a scalar function varying with the location in the image. The diffusion proposed by [Perona and Malik, 1990], presented in Subsection 2.1.2, limits the smoothing of an image near the pixels with a high gradient magnitude (edge pixels). As the diffusion near an edge is very weak, the noise smoothing near the edge is also small.

2.1.4 Hessian based vesselness for vessel segmentation

In order to analyze the local behavior of an image I, differentiation is computed in the setting of the linear scale space theory, by defining it as a convolution with derivatives of Gaussian as introduced in Subsection 2.1.2

$$\frac{\partial}{\partial x} I(\boldsymbol{x}, \sigma) = s^{\gamma} I(\boldsymbol{x}) * \frac{\partial}{\partial x} G(\boldsymbol{x}, \sigma). \tag{2.28}$$

The parameter γ was introduced by [Lindeberg, 1998] to define a family of normalized derivatives. This normalization is particularly important for a fair comparison of the response of differential operators at multiple scales. [Lindeberg, 1998] suggested that if there is no preference of vessels with particular width, γ should be set to 1. The Gaussian kernel is defined as in Equation 2.21. Note some important properties of the Gaussian and its second derivative, that makes these kernel so attractive for vessel enhancement. Gaussian blurring can reduce the influence of noise and properly shape the intensity on the vessel cross section into a Gaussian profile, so as to ensure a large value of the second derivative across the vessel cross section, even in the case of a plateau-like profile or in slight intensity variation at the vessel center. Its second derivative kernel at scale σ generates a probe kernel that measures the contrast between the regions inside and outside the range $(-\sigma, \sigma)$ in the direction of the derivative, therefore tuning the filter response to a specific vessel scale, see Figure 2.2A and B.

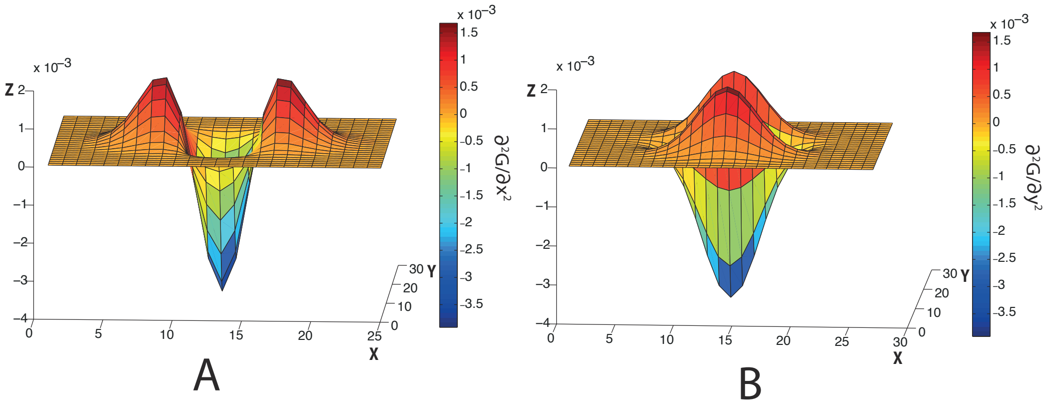

FIGURE 2.2: The second order derivative of a Gaussian kernel probes inside/outside contrast of the range $(-\sigma, \sigma)$. In this example $\sigma = 2.5$. A. $\frac{\partial^2 G}{\partial x^2}$. B. $\frac{\partial^2 G}{\partial y^2}$

A common method for vessel enhancement filtering is based on the eigenanalysis of the Hessian matrix that captures the second order structure of local intensity variations in the proximity of each pixel. [Frangi et al., 1998] analyzed the meaning of the Hessian eigenvalues and gave an intuitive geometrical interpretation of the eigensystem. As we are working on a 2D image, the Hessian matrix is given as:

$$H_{\sigma_s}(I) = \begin{pmatrix} \frac{\partial^2 I}{\partial x^2} & \frac{\partial^2 I}{\partial x \partial y} \\ \frac{\partial^2 I}{\partial y \partial x} & \frac{\partial^2 I}{\partial y^2}. \end{pmatrix} \tag{2.29}$$

The Hessian matrix H_{σ_s} is calculated at the position $\boldsymbol{x}$ and scale σ_s. By eigenvalue decomposition we have: a small eigenvalue λ_1 with its corresponding eigenvector $\boldsymbol{v_1}$ indicating the direction of a tubular structure and a large eigenvalue λ_2 associated with the eigenvector $\boldsymbol{v_2}$ perpendicular to the tubular structure. Table 2.2 summarizes the conditions for the eigenvalues of the Hessian for the detection of different structures that we can find while applying this decomposition in a discrete image.

Frangi's vessel enhancement

TABLE 2.2: Possible patterns in 2D depending on the value of the eigenvalues λ_k, $k \in 1, 2$. The eigenvalues are ordered $|\lambda_1| \leq |\lambda_2|$, sgn is the sign function

λ_1	λ_2	orientation pattern
$\lvert\lambda_1\rvert \approx 0$	$\lvert\lambda_2\rvert \approx 0$	noise no preferred direction
$\lvert\lambda_1\rvert \approx 0$	$\lvert\lambda_2\rvert \gg 0$, $sgn(\lambda_2) = -1$	tubular structure (bright)
$\lvert\lambda_1\rvert \approx 0$	$\lvert\lambda_2\rvert \gg 0$, $sgn(\lambda_2) = 1$	tubular structure (dark)
$\lvert\lambda_1\rvert \gg 0$, $sgn(\lambda_1) = -1$	$\lvert\lambda_2\rvert \gg 0$, $sgn(\lambda_2) = -1$	blob structure (bright)
$\lvert\lambda_1\rvert \gg 0$, $sgn(\lambda_1) = 1$	$\lvert\lambda_2\rvert \gg 0$, $sgn(\lambda_2) = 1$	blob structure (dark)

The *vesselness* feature $V(\sigma_s)$ proposed by [Frangi et al., 1998] is calculated at the position $\boldsymbol{x}$ using the equation for the “dissimilarity measure” R_B defined as

$$R_B = \frac{\lambda_2}{\lambda_1} \tag{2.30}$$

and the equation for the "second order structuredness" S defined as

$$S = \sqrt{\lambda_1^2 + \lambda_2^2} \tag{2.31}$$

as

$$V(\sigma_s) = \begin{cases} 0, \text{if } \lambda_1 > 0 \\ e^{-\frac{R_B^2}{2\beta^2}}(1 - e^{-\frac{S^2}{2c^2}}), \end{cases} \tag{2.32}$$

where β and c are constants which control the sensitivity of the filter. R_B accounts for the deviation from blob-like structures, but can not differentiate background noise from real vessels. Since the background pixels have a small magnitude of derivatives ($\approx$ 0) and, thus small eigenvalues($\approx$ 0). In regions with high contrast compared to the background, S will become larger since at least one of the eigenvalues will be large in magnitude ($\gg$ 0). Thus S helps to distinguish between noise and background.

The scale so far is a free parameter: if the scale to choose is unknown, one would calculate them all. It is known that an operator gives maximal output if its size (in this context the scale parameter) is tuned best to the object [Lindeberg, 1994]. In practice calculations of the *vesselness* are performed for certain range of scales $\sigma_1, ..., \sigma_n$. σ represents a real length, pixels or voxel, which also incorporates the image resolution (μm or mm). The range is taken from the smallest to the thickest expected vessel thickness with an increment of 1.0 to enhance vessels with different thicknesses. The thickness of the vessels is either known a priori (for example from the anatomical information, data acquisiton type, and image resolution), or can be approximated by direct measurements. Also note that in this setting we use an isotropic scaling, i.e. σ is the same along each coordinate axis. The results are combined by a weighted maximum projection

$$V(\boldsymbol{x}) = \max_{s_{min} \leq s \leq s_{max}} V_{\sigma_s}(\boldsymbol{x}). \tag{2.33}$$

To see an example of the *vesselness* response, consider the ideal white vessel on a black background, see Figure 2.3A.

The image has the size 128×128 with a vessel radius of 4 pixels at the image center to the left and right. The result of taking the maximum response over a range of 10 scales, $\sigma \in \{1, 2.., 10\}$ is shown in Figure 2.3B. Each σ is given in pixels. Figure 2.3C shows that the maximum of the *vesselness* response is obtained at $\sigma = 5$ pixels, the red circle in the image. Figure 2.3D shows the response of the *vesselness* at the row in the middle of the vessel (the red arrow in Figure 2.3A) at each scale. Again we can see that the maximum response is obtained at $\sigma = 5$ pixels.

The method was developed for CT angiography images, but it has been applied in a wide variety of vessel segmentation algorithms and detection of tubular objects in different modalities. With a far better background suppression performance and the flexibility of changing parameters, Frangi's method is generally considered the most satisfactory among these methods [Olabarriaga et al., 2003]. However, as the Hessian matrix is a local quantity, any Hessian matrix based measures depending upon the eigenvalues and the eigenvectors will be sensitive to local intensity structures and also intensity abnormalities, noise which can give false positive results, and discontinuous responses along vessel direction. These effects are undesirable for both vessel enhancement and visualization improvement. Moreover, it tends to suppress junctions since junctions cannot be characterized as a curvilinear model. Also one of the disadvantages is the computational requirement. As [Frangi et al., 1998] proposed, the method calculates the Hessian matrix and the given measures for increasing neighborhood sizes, until the neighborhood is bigger than the expected thickest vessel. Given high resolution images, this can easily increase from 20 to 30 iterations per pixel [Budai et al., 2013].

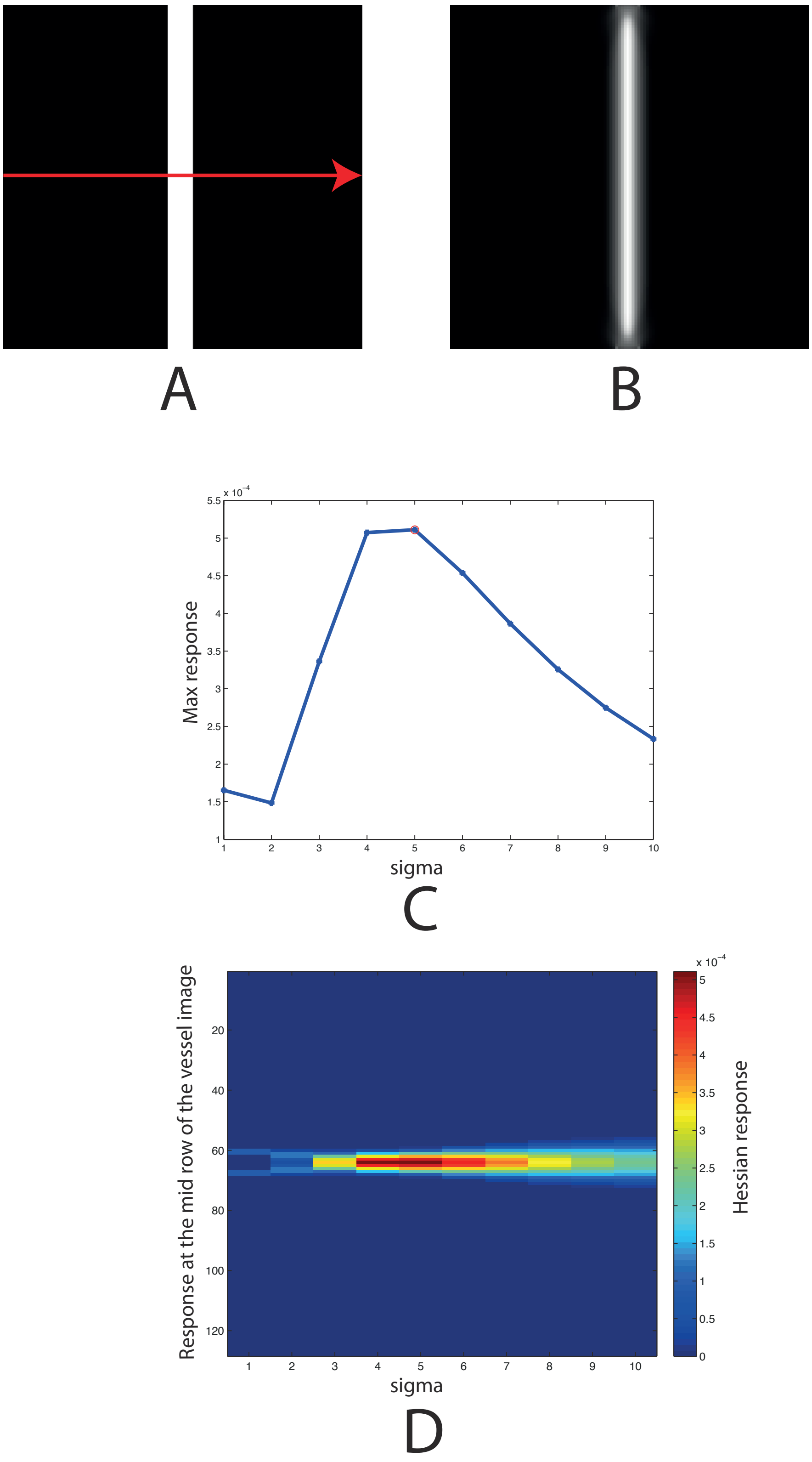

FIGURE 2.3: A. An example of a blood vessel white on a black background. The image has the size 128×128 with a vessel radius of 4 pixels at the image center to the left and right. B. The maximum *vesselness* response taken over a range of scales $\sigma \in \{1, 2.., 10\}$ pixels. C. A graph showing the maximum *vesselness* response at each scale. The red circle shows the maximum point of the *vesselness* response over all scales. D. The *vesselness* response at the middle row through the vessel (red arrow in Figure A) for each scale.

2.1.5 Optimally oriented flux as a descriptor for tubular structures

With the motivation to address the problem of segmenting thin elongated structures in grey value images, [Vasilevskiy and Siddiqi, 2002] derived the geometric flow which maximizes the rate of increase of flux of an auxiliary vector field through a curve or a surface.

Let $C(p,t)$ be a smooth family of closed curves evolving in the plane. Here t parametrizes the family and p parametrizes the given curve. Without loss of generality, assume that $0 \leqslant p \leqslant 1$, i.e. that $C(0,t) = C(1,t)$. Consider also a vector field $\boldsymbol{V}$ defined for each point $(x,y)^T \in \mathbb{R}^2$. The total inward flux of the vector field through the curve is given by the contour integral

$$F_t = \int_0^1 \langle \mathbf{V}, \mathbf{N} \rangle \left\| \frac{\partial C}{\partial p} \right\| dp = \int_0^{L(t)} \langle \mathbf{V}, \mathbf{N} \rangle \, ds, \tag{2.34}$$

where $L(t)$ is the Euclidean length of the curve and N is the normal to C. Intuitively, the inward flux through a planar closed curve provides a measure of how well the curve is aligned with the direction perpendicular to the vector field. The main theoretical result of [Vasilevskiy and Siddiqi, 2002] is that the direction in which the inward flux of the vector field **V** through the curve C is increasing most rapidly is given by

$$\frac{\partial C}{\partial t} = \text{div } (\mathbf{V})\mathbf{N}. \tag{2.35}$$

In other words, the flow which maximizes the rate of increase of the total inward flux is obtained by moving each point of the curve in the direction of the inward normal by an amount proportional to the divergence of the vector field.

The intuition behind using the flux maximizing flow for blood vessel segmentation is illustrated in Figure 2.4A. Here a cross section through an idealized blood vessel (a bright region in a uniform darker background) is depicted. It is clear that if one considers the gradient of the image ∇I to be the vector field **V** whose inward flux through the evolving surface is to be maximized, then the optimal configuration is for the evolving surface to align itself locally to the blood vessel boundaries.

For the analysis of tubular structures, it is useful to compute flux in a 2D circular region. Therefore, the chosen flux value at a particular location is the maximum (magnitude) flux over the range of radii, corresponding to a range of blood vessel widths see Figure 2.4B. Normalization over the scales is simply done by division by the number of entries in the discrete sum that approximates Equation 2.35.

Optimally Oriented Flux

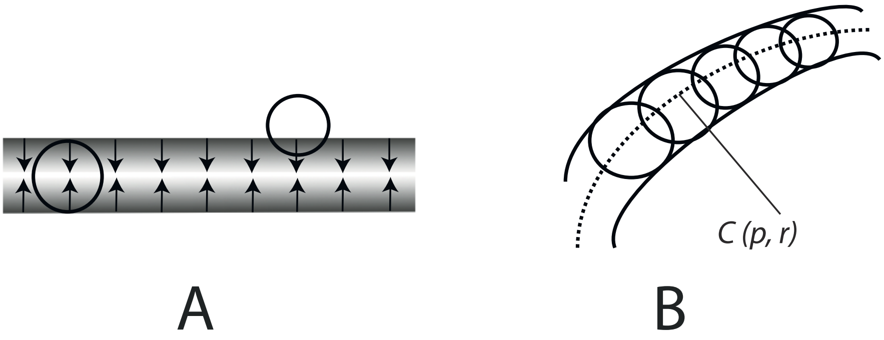

FIGURE 2.4: A. An illustration of the gradient vector field in the vicinity of a blood vessel (the vessel has high intensity compared to the background). Assuming a uniform background intensity, at its centerline, the total outward flux at the scale of the vessel's width is negative. Outside the vessel, at a smaller scale, the total outward flux is positive. B. A curvilinear structure is represented as an envelope of a family of circles with continuously changing center points and radii, where p represents the location of a point in the original image domain, $r \in [0, r_{max}]$ represents the radius of the circle centered at p (r_{max} is the largest allowed thickness of the vessel to be captured), $C(p, r)$ represents a path composed by center points of a family of circles.

[Law and Chung, 2008] introduced the concept of optimally oriented flux (OOF) to detect 3D curvilinear structures. This concept is completely different than the flux based approach introduced by [Vasilevskiy and Siddiqi, 2002] which is included in a global energy to be minimize along the tubular structures, while flux defined by [Law and Chung, 2008] is a local feature which allows to define a local metric in order to minimize a path energy. At a position $\boldsymbol{x}$ the OOF is defined by outward oriented flux along a direction $\boldsymbol{\rho}$. It is calculated by projecting the image gradient, denoted here as $\mathbf{v} = \nabla I$, along the direction of $\boldsymbol{\rho}$ prior to the computation of the flux in a local circular region D_r.

$$f(\mathbf{x}, r, \boldsymbol{\rho}) = \int_{\partial D_r} [(\mathbf{v}(\boldsymbol{x} + \mathbf{h}) \cdot \boldsymbol{\rho})\boldsymbol{\rho}] \cdot \mathbf{n} dL, \tag{2.36}$$

where D_r represents a circular region with radius r, dL is the infinitesimal length on boundary ∂D_r, $\boldsymbol{\rho} = (\rho_1, \rho_2)^T$ is the direction along which the gradient is projected, $\mathbf{n} = (n_1, n_2)^T$ is the outward unit normal of ∂D_r, $\mathbf{v} = (v_1, v_2)^T$ is the gradient of an image I, $\mathbf{h} = r\mathbf{n}$, thus

$$f(\mathbf{x}, r, \boldsymbol{\rho}) = \begin{pmatrix} \rho_1 & \rho_2 \end{pmatrix} \underbrace{\begin{pmatrix} \int_{\partial D_r} v_1(\mathbf{x} + r\mathbf{n}) n_1 dL & \int_{\partial D_r} v_2(\mathbf{x} + r\mathbf{n}) n_1 dL \\ \int_{\partial D_r} v_1(\mathbf{x} + r\mathbf{n}) n_2 dL & \int_{\partial D_r} v_2(\mathbf{x} + r\mathbf{n}) n_2 dL \end{pmatrix}}_{\text{Qr,x}} \begin{pmatrix} \rho_1 \\ \rho_2 \end{pmatrix} \tag{2.37}$$

$$= \boldsymbol{\rho}^T Q_{r,x} \boldsymbol{\rho}.$$

Each entry in the matrix $Q_{r,x}$, at the ith row and jth column can be rewritten as

$$q_{r,x}^{i,j} = \int_{\partial D_r} v_i(\boldsymbol{x} + r\boldsymbol{n}) n_j dL = \int_{\partial D_r} [v_i(\boldsymbol{x} + r\boldsymbol{n})\boldsymbol{e_j}] \cdot \boldsymbol{n} dL, \tag{2.38}$$

where $\boldsymbol{e_1}$, $\boldsymbol{e_2}$ are the unit vectors along x, respectively y directions. Using the divergence theorem each $q_{r,x}^{i,j}$ can be expressed by

$$q_{r,x}^{i,j} = \int_{D_r} \text{div}\,[v_i(\boldsymbol{x} + \boldsymbol{y})\boldsymbol{e_j}] dS = \int_{D_r} \frac{\partial}{\partial \boldsymbol{e_j}} v_i(\boldsymbol{x} + \boldsymbol{y}) dS, \tag{2.39}$$

where $\mathbf{y}$ is the position vector inside the circle D_r. In practice, $\mathbf{v}$ is obtained from a Gaussian smoothed image, which ensures the differentiability of the discrete image signal I, see Subsection 2.1.2, $\mathbf{v} = \nabla(G_\sigma * I)$ where G_σ is a Gaussian function and $*$ represents the convolution operation. σ is taken to be 1. Thus $v_i(\boldsymbol{x}) = (G_{\boldsymbol{e_i},\sigma} * I)(\boldsymbol{x})$. $G_{\boldsymbol{e_i}}, \sigma$ is the first derivative of Gaussian along the direction $\boldsymbol{e_i}$. Furthermore, the surface integral in Equation 2.39 can be extended to the whole image domain Ω using a step function 1_{D_r} given as

$$1_{D_r} = \begin{cases} 1, \sqrt{x^2 + y^2} \le r \\ 0, \text{otherwise.} \end{cases} \tag{2.40}$$

Thus Equation 2.39 becomes

$$q_{r,x}^{i,j} = \int_{\Omega} 1_{D_r}(\boldsymbol{y})[G_{\boldsymbol{e_i}\boldsymbol{e_j},\sigma} * I)(\boldsymbol{x} + \boldsymbol{y})] dS = [(1_{D_r} * G_{\boldsymbol{e_i}\boldsymbol{e_j},\sigma})(\boldsymbol{x})] * I(\boldsymbol{x}), \tag{2.41}$$

where $G_{\boldsymbol{e_i}\boldsymbol{e_j},\sigma}$ is the second derivative of G. Hence Equation 2.36 becomes

$$f(\mathbf{x}, r, \boldsymbol{\rho}) = \boldsymbol{\rho}^T [(1_{D_r} * G_{\boldsymbol{e_i}\boldsymbol{e_j},\sigma})(\boldsymbol{x})] * I(\boldsymbol{x}) \boldsymbol{\rho}. \tag{2.42}$$

To detect vessels having higher intensity than the background region, one would be interested in finding the vessel direction which minimizes $f(\mathbf{x}, r, \boldsymbol{\rho})$, i.e. we are looking for $\underset{\boldsymbol{\rho}}{\operatorname{argmin}} f(\mathbf{x}, r, \boldsymbol{\rho})$. By differentiating the above equation with respect to $\boldsymbol{\rho}$, minimization of function f is in turn acquired as solving a generalized eigenvalue decomposition problem.

Solving the generalized eigendecomposition problem gives two eigenvalues, $\lambda_1(\boldsymbol{x}, r)$ and $\lambda_2(\boldsymbol{x}, r)$, where $\lambda_1(\boldsymbol{x}, r) \leq \lambda_2(\boldsymbol{x}, r)$ and two eigenvectors $\boldsymbol{\omega_1}(\boldsymbol{x}, r)$ and $\boldsymbol{\omega_2}(\boldsymbol{x}, r)$, i.e. $\lambda_1(\boldsymbol{x}, r) = f(\boldsymbol{x}, \boldsymbol{\omega_1}(\boldsymbol{x}, r), r)$ and $\lambda_2(\boldsymbol{x}, r) = f(\boldsymbol{x}, \boldsymbol{\omega_2}(\boldsymbol{x}, r), r)$.

As the evaluation of Equation 2.36 is grounded on analyzing image gradients along the boundary of the disc D_r, the OOF detection results are only induced when the disc boundary touches the object boundary. Along the vessel direction, $\boldsymbol{\omega_2}(\boldsymbol{x}, r)$, $|\lambda_2(\boldsymbol{x}, r)| \approx 0$ inside the vessel as the image gradient $\|\boldsymbol{v}(\boldsymbol{x})\| \approx 0$ along $\boldsymbol{\omega_2}(\boldsymbol{x}, r)$. Along $\boldsymbol{\omega_1}(\boldsymbol{x}, r)$, $|\lambda_1(\boldsymbol{x}, r)|$ depends on r of the local disc D_r and the position $\boldsymbol{x}$, the position where OOF is evaluated. To exemplify the variation of $|\lambda_1(\boldsymbol{x}, r)|$ see Figure 2.5 as following:

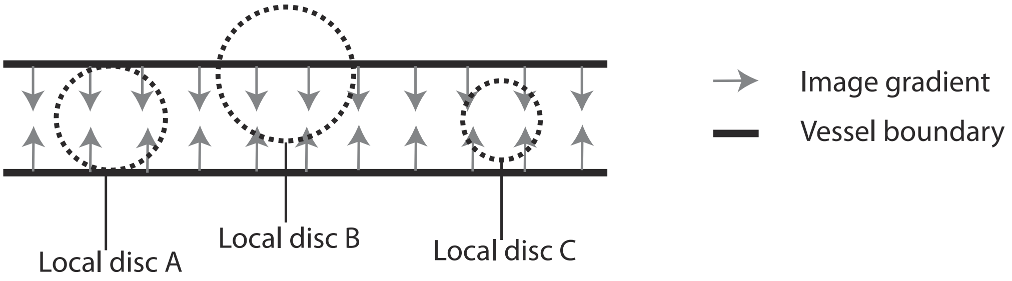

FIGURE 2.5: Three examples of computing OOF using different radii at various positions at a vessel

- for the local disc A when r is the radius of the vessel, and $\boldsymbol{v}(\boldsymbol{x})$ is projected along $\boldsymbol{\omega_1}(\boldsymbol{x}, r)$, the projected gradient at the contacting positions between the boundary of D_r is aligned along the orientation of D_r outward unit normal $\frac{\boldsymbol{n}(\boldsymbol{x})}{\|\boldsymbol{n}(\boldsymbol{x})\|}$, i.e. $\frac{\boldsymbol{v}(\boldsymbol{x})\cdot\boldsymbol{\omega_1}(\boldsymbol{x},r)}{\|\boldsymbol{\omega_1}(\boldsymbol{x},r)\|}\frac{\boldsymbol{\omega_1}(\boldsymbol{x},r)}{\|\boldsymbol{\omega_1}(\boldsymbol{x},r)\|} = c\frac{\boldsymbol{n}(\boldsymbol{x})}{\|\boldsymbol{n}(\boldsymbol{x})\|}$, c is a constant. Thus $|\lambda_1(\boldsymbol{x}, r)| \gg 0$ and $\lambda_1(\boldsymbol{x}, r) < 0$.

- for the local disc B at the contacting position between the boundary of D_r, the image gradients $\boldsymbol{v}(\boldsymbol{x})$ that point to the center of the vessel are not aligned along the disc outward unit normal $\frac{\boldsymbol{n}(\boldsymbol{x})}{\|\boldsymbol{n}(\boldsymbol{x})\|}$. Therefore $|\lambda_1(\boldsymbol{x}, r)|$ will be smaller than in case of the local disc A.

- for local disc C there is no contacting position between the boundary of D_r and the vessel boundary. Thus $|\lambda_1(\boldsymbol{x}, r)| \approx 0$ and random.

To see an example of the OOF response, consider the ideal white vessel on a black background, see Figure 2.6A. The image has the size 128×128 with a vessel radius of 4 pixels at the image center to the left and right. The result of taking the maximum response over a range of 10 radii, $r \in \{1, 2.., 10\}$ is shown in Figure 2.6B. Each radius is given in pixels. Figure 2.6C shows that the maximum of the OOF response is obtained at $r = 5$ pixels, the red circle in the image. Figure 2.6D shows the response of the OOF at the row in the middle of the vessel (the red arrow in Figure 2.6A) at each radius. Again we can see that the maximum response is obtained at $r = 5$ pixels. Some important properties of the OOF are

- it discovers the structure direction by finding an optimal projection axis which minimizes the oriented flux.
- detection response is induced from the intensity discontinuities at the object boundary when the local circle touches the object boundary of the structure.
- it can be utilized to distinguish between regions inside and outside curvilinear structures.
- it is localized at the boundary of the local spherical region (distinct from the Hessian matrix, OOF does not consider the region in the vicinity of the structure where a nearby object is possibly present, thus is robust against the disturbance introduced by closely located objects)
- it allows the possibility of defining measures for identifying structures in a specific shape (not only curvilinear) by using combinations of its eigenvalues
- multi-scale detection is easy to integrate, as the normalization for the detection of OOF using a set of radii (r in Equation 2.36) requires only dividing the computational result of Equation 2.36 by $2\pi r$ (the length of the circular region)
- by using fast Fourier transform, the complexity of evaluating Equation 2.39 and thus Qr, x is $O(NlogN)$ compared to using the conventional spatial implementation in the entire image domain with pixels is $O(KN)$ (K is the number of orientation samples taken on the circumference of the circle)

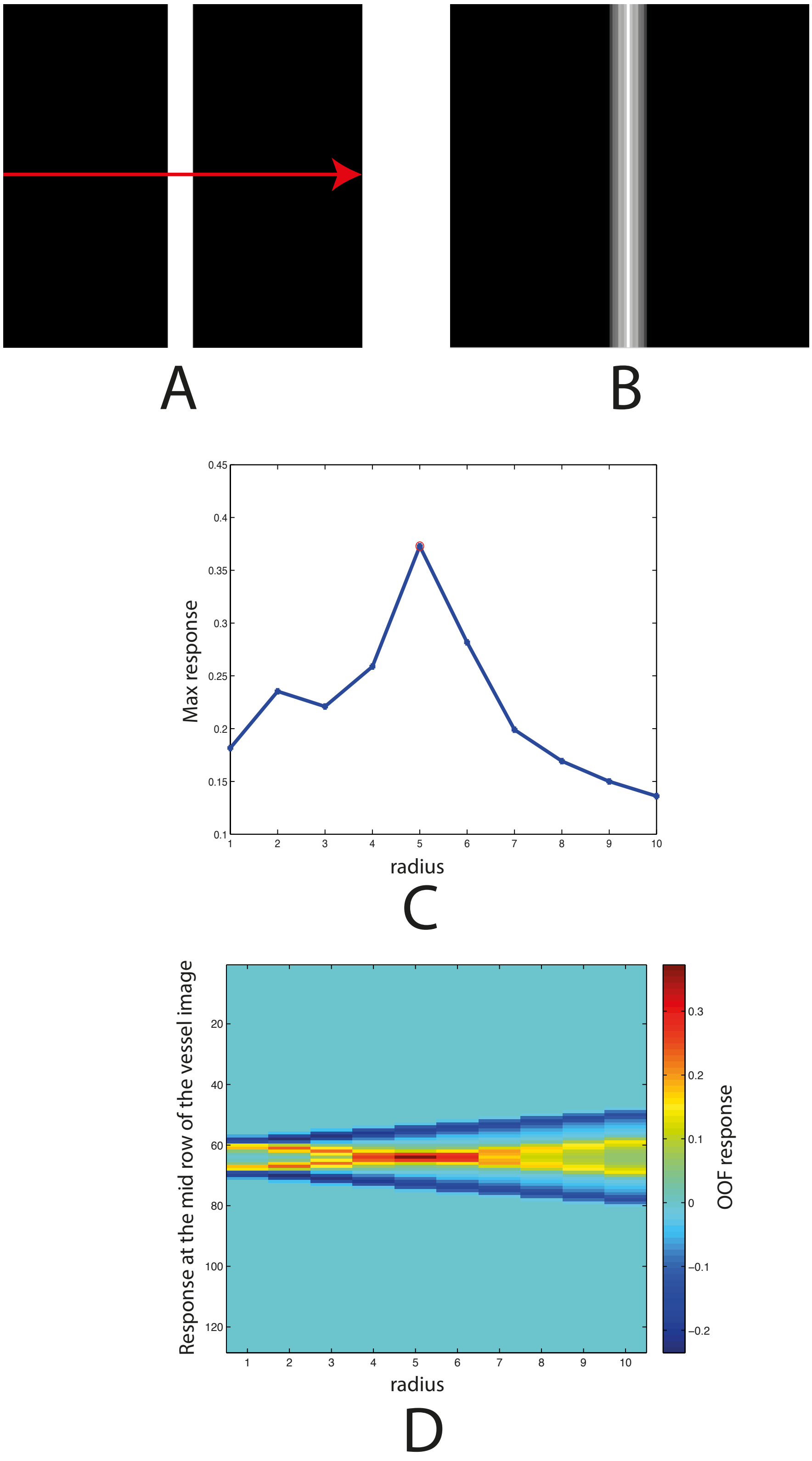

FIGURE 2.6: A. An example of a blood vessel white on a black background. The image has the size 128×128 with a vessel radius of 4 pixels at the image center to the left and right. B. The maximum OOF response taken over a range of radii $r \in \{1, 2.., 10\}$ pixels. C. A graph showing the OOF response at each radius. The red circle shows the maximum point of the OOF response. D. The OOF response at the middle row through the vessel (red arrow in Figure A) for each radius.

OOF has been developed to supply information of curvilinear structures for extracting vessels in a vascular image [Law and Chung, 2008]. Its performance has been extensively tested in vascular images in phase contrast magnetic resonance angiographic volumes (the image intensity represents the blood flow speed inside the vasculature). The challenges for extraction algorithms are represented by the presence of closely located vessels due to the complicated geometry of vascular structures, and the small and low intensity vessels in images with relatively high background noise level. The OOF based method was capable of discovering the small separation between the closely located vessels and in high level noise conditions. Furthermore, for tracking curvilinear structure centerlines, it was able to estimate the structure direction and to guide the centerline tracking process in a robust way.

2.1.6 Thin plate spline

TPS is a commonly used basis function for representing coordinate mappings from $\mathbb{R}^2$ to $\mathbb{R}^2$. This interpolation algorithm was borrowed from continuum mechanics and was introduced to morphometrics by [Bookstein, 1989]. It generates a deformation grid (mapping function) between two point configurations that maps the actual points exactly and is otherwise as smooth as possible. The spline surface represents a thin metal sheet that is constrained not to move at grid points. The construction is based on choosing a function that minimizes an integral that represents the bending energy of the resulting surface. Let v_i denote the target function values at locations in the plane, with $i = 1, 2, ..., p$. We assume that the locations (x_i, y_i) are all different and are not collinear. The idea of TPS is to choose a function $f(x, y)$ that exactly interpolates the data points (x_i, y_i) and minimizes the bending energy

$$E_f = \iint_{\mathbb{R}^2} \left[\left(\frac{\partial^2 f}{\partial x^2} \right)^2 + \left(\frac{\partial^2 f}{\partial x \partial y} \right)^2 + \left(\frac{\partial^2 f}{\partial y^2} \right)^2 \right] dxdy. \tag{2.43}$$

This least bent surface is given by the following equation

$$f(x, y) = a_1 + a_x x + a_y y + \sum_{i=1}^{p} w_i U(\|(x_i, y_i) - (x, y)\|), \tag{2.44}$$

where $U(r) = r^2 \log r$. The first three terms correspond to the linear part which defines a flat plane that best matches all control points (this can be seen as a least square fitting). The last term corresponds to the bending forces provided by n control points. There is a coefficient w_i for each control point.

In order for $f(x, y)$ to have square integrable second derivatives, it is requiered that

$$\sum_{i=1}^{p} w_i = 0 \tag{2.45}$$

and

$$\sum_{i=1}^{p} w_i x_i = \sum_{i=1}^{p} w_i y_i = 0. \tag{2.46}$$

Together with the interpolation conditions, $f(x_i, y_i) = v_i$, this yields a linear system for the TPS coefficients

$$L = \begin{bmatrix} K & P \\ P^T & O \end{bmatrix} \begin{bmatrix} \boldsymbol{w} \\ \boldsymbol{a} \end{bmatrix} = \begin{bmatrix} \boldsymbol{v} \\ \boldsymbol{o} \end{bmatrix}, \tag{2.47}$$

where $K_{ij} = U(\|(x_i, y_i) - (x_j, y_j)\|)$, the distance between two control points, the *ith* row of P is $(1, x_i, y_i)$, O is a 3×3 matrix of zeros, $\boldsymbol{o}$ is a 3×1 column vector of zeros, $\boldsymbol{w}$ and $\boldsymbol{v}$ are column vectors formed from w_i and v_i, respectively, and $\boldsymbol{a}$ is the column vector with elements a_1, a_x, a_y. We will denote the $(p+3) \times (p+3)$ matrix of this system by $L = \begin{bmatrix} K & P \\ P^T & O \end{bmatrix}$; note that L is nonsingular as shown in [Powell, 1996]. Therefore the data defines the function f uniquely. To find the unknown coefficients, that is the matrix $\begin{bmatrix} \boldsymbol{w} \\ \boldsymbol{a} \end{bmatrix}$, we can either find the inverse L^{-1}, or solve it as a linear system. Since L is by definition symmetric, the last system in Equation 2.47 can be easily solved with for instance a LU decomposition. When there is noise in the specified values v_i, one may wish to relax the exact interpolation requirement by means of regularization. This is accomplished by minimizing:

$$H[f] = \sum_{i=1}^{n} (v_i - f(x_i, y_i))^2 + \lambda E_f. \tag{2.48}$$

The regularization parameter λ, a positive scalar between 0 and 1, controls the amount of smoothing. The limiting case of $\lambda = 0$ reduces to a least square approximation by a linear polynomial. TPS coefficients in the regularized case can be solved by replacing the matrix K by $K + \lambda I$, where I is the $p \times p$ identity matrix. A 2D TPS can be fit to a 3D segmented surface to obtain a smooth (smoothness controlled by λ) 3D reference plane with respect to which the dataset is flattened. The limitation of this method consists in the fact that since inverting L is an $O(p^3)$ operation, consequently solving for the TPS coefficients can be very expensive when p is large.

An example of a 2D TPS surface with 10 control points and different regularization parameters is given in Figure 2.7A with $\lambda = 0$, Figure 2.7B with $\lambda = 0.5$, Figure 2.7C with $\lambda = 1$.

2.2 Anterior visual system

In order to explain the role of the retina and its connection to the CNS we present in this section some basic anatomical background about the anterior visual system.

2.2.1 Visual pathway

The human visual system is a complex system and requires communication between its major sensory organ, the eye, and the core of the central nervous system, the brain, to interpret external stimuli into sight images. Vision depends mainly on one sensory organ, the eye. The human eye is one of the most complicated structures as illustrated in Figure 2.8A, and it requires many components to allow our advanced visual capabilities. The eye has three major layers:

- the sclera, which maintains, protects, and supports the shape of the eye and includes the cornea
- the choroid, which provides oxygen and nourishment to the eye and includes the pupil, iris, and lens
- the retina, which allows us to piece images together

All vision is based on the perception of electromagnetic rays. These rays, in the form of light, must pass through the cornea, which focuses the rays. They then enter the eye through the pupil, the black aperture at the front of the eye. The pupil acts as a gatekeeper, allowing as much or as little light to enter as is necessary to see an image properly. The pigmented area around the pupil is the iris. Along with supplying a person's eye color, the iris is responsible for acting as the pupil's stop. Two layers of muscles contract or dilate the pupil to change the amount of light that enters the eye. Behind the pupil is the lens, similar in shape and characteristics to a camera

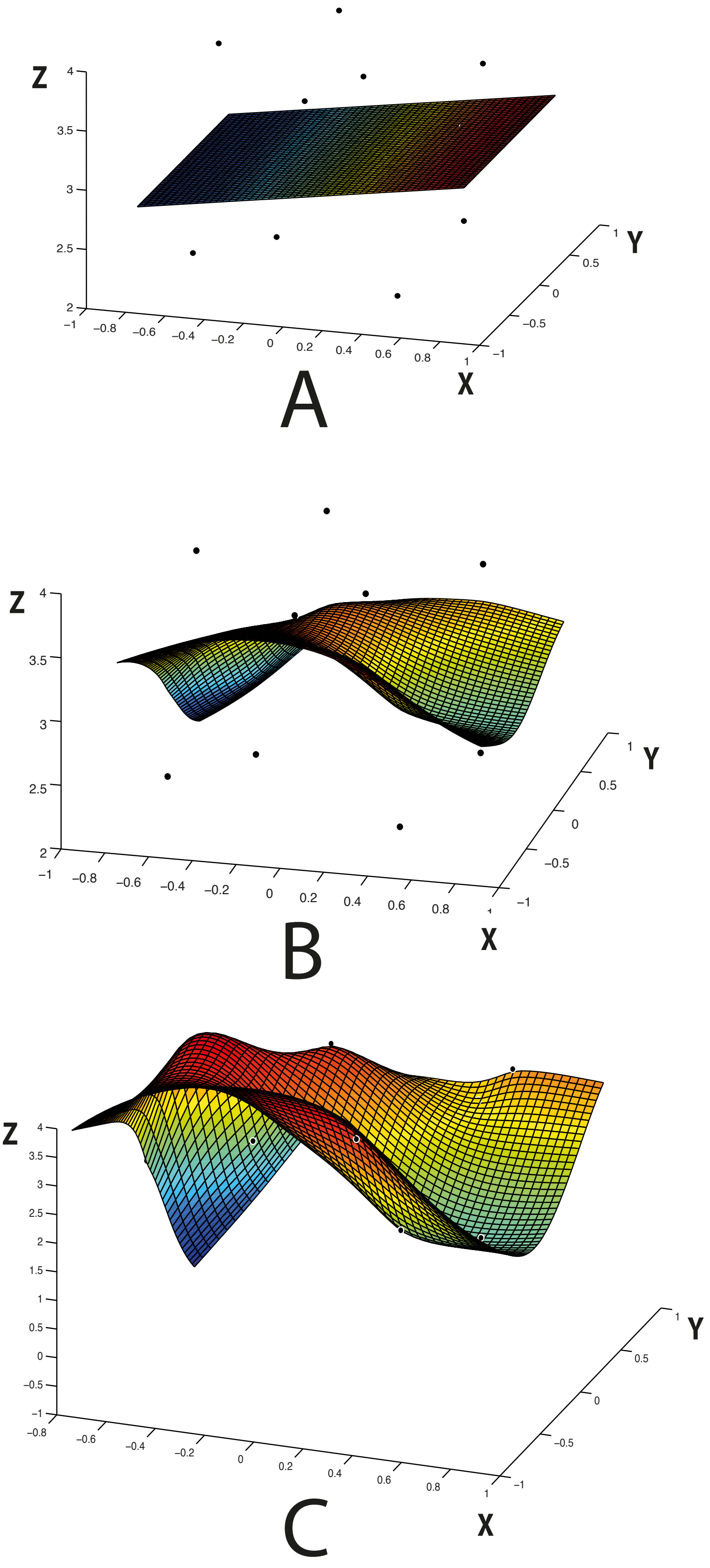

FIGURE 2.7: 2D TPS surface with 10 control points (black dots) and different regularization parameters. A. $\lambda = 0$. B. $\lambda = 0.5$. C. $\lambda = 1$.

lens. Together with the cornea, the lens adjusts the focal length of the image being seen onto the back of the eye, the retina. Visual reception occurs at the retina where photoreceptor cells called cones and rods give an image color and shades. The image is transduced into neural impulses and then transferred through the optic nerve to the brain for processing, see Figure 2.8C. The visual cortex in the brain interprets the image to extract form, meaning, memory and context [UTHMedicalSchool].

2.2.2 Retina anatomy and structures

The retina is a complex structure approximately 0.5 mm thick consisting of alternating layers of cell bodies and cell processes and lines the back of the eye [Kolb]. It is formed during embryogenesis from neural tissue, therefore, part of the central nervous system. It contains five types of neurons: the visual receptor cells (the rods and cones), the horizontal cells, the bipolar cells, the amacrine cells, and the retinal ganglion cells, see Figure 2.8A. The innermost layers are located nearest the vitreous chamber, whereas the outermost layers are located adjacent to the retinal pigment epithelium and choroid. The structures and layers seen in the retina are as illustrated in Figure 2.9, and are described briefly below:

- ILM is the boundary between the retina and the vitreous body.
- Retinal Nerve Fiber Layer (RNFL) consists of unmyelinated axons of the ganglion cells that form the optic nerve.
- Ganglion Cell Layer (GCL) contains the nuclei of the ganglion cells.
- Inner Plexiform Layer (IPL) contains axons of bipolar, and the dendrites of the amacrine and ganglion cells.
- Inner Nuclear Layer (INL) contains the nuclei of horizontal, bipolar, amacrine and Müller cells.
- Outer Plexiform Layer (OPL) consists of photoreceptor axons, and dendrites of horizontal and bipolar cells.
- Outer Nuclear Layer (ONL) consists of the cell bodies of the photoreceptor (both rods and cones) cells.

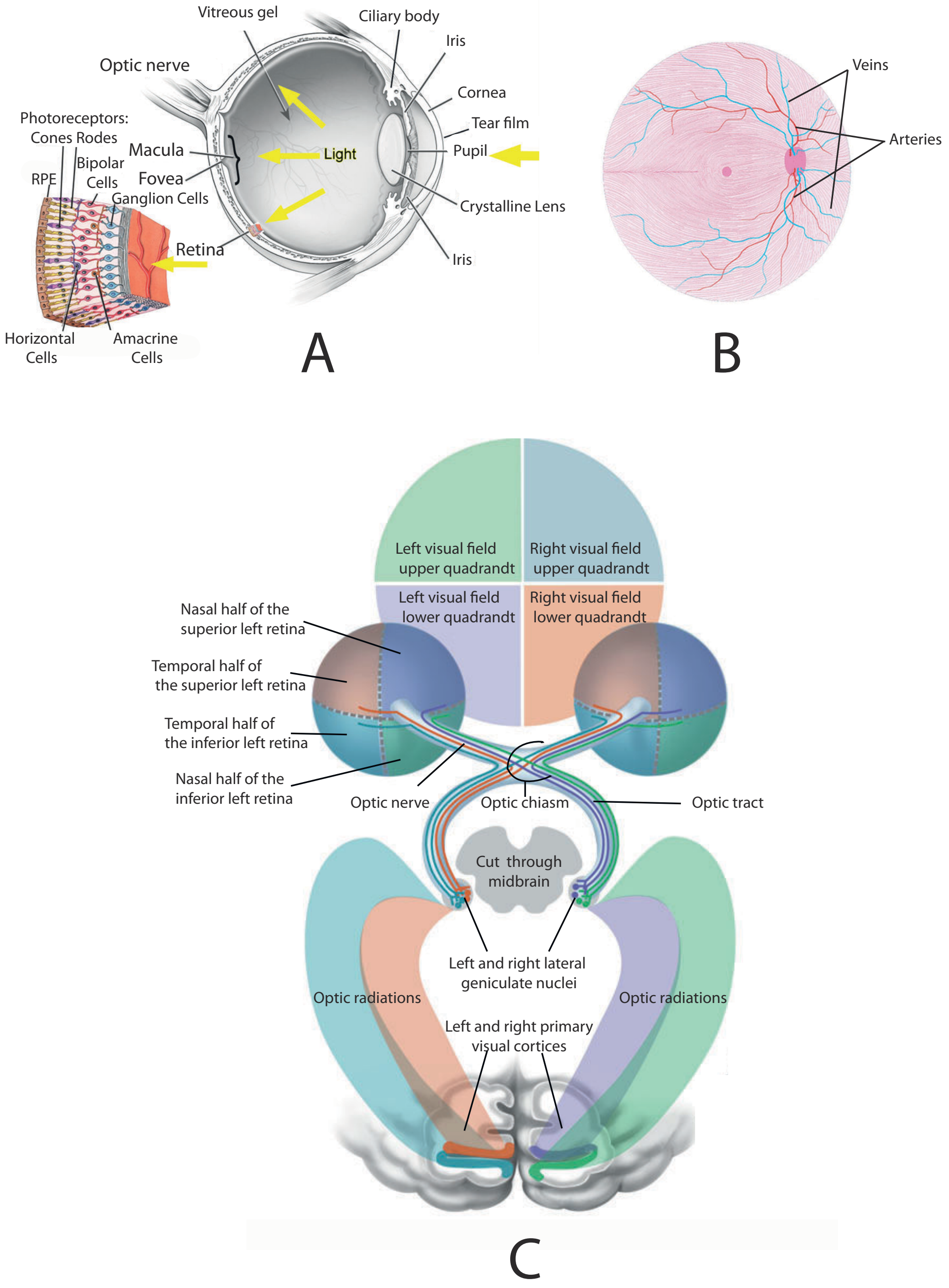

FIGURE 2.8: A. Gross anatomy of the human eye and detail of the retina [Fuensanta and Doble, 2012]. B. Schematic representation of the course of the ganglion cells axons in the retina before they exit through the optic nerve and of the retinal vessel distribution [UTHMedicalSchool]. C. The visual pathway. The quadrants of the visual fields are color-coded to show transmission of information to the retinae and to the primary visual cortices where the image is first perceived. Modified image from [Stedman'sMedicalDictionary, 2015]

- The inner segments (IS) consists of the photoreceptors.
- The inner segments-outer segments (IS/OS) consists of the junction between the inner segments and the outer segments .
- RPE is a single layer of cells between the retina and the choroid.

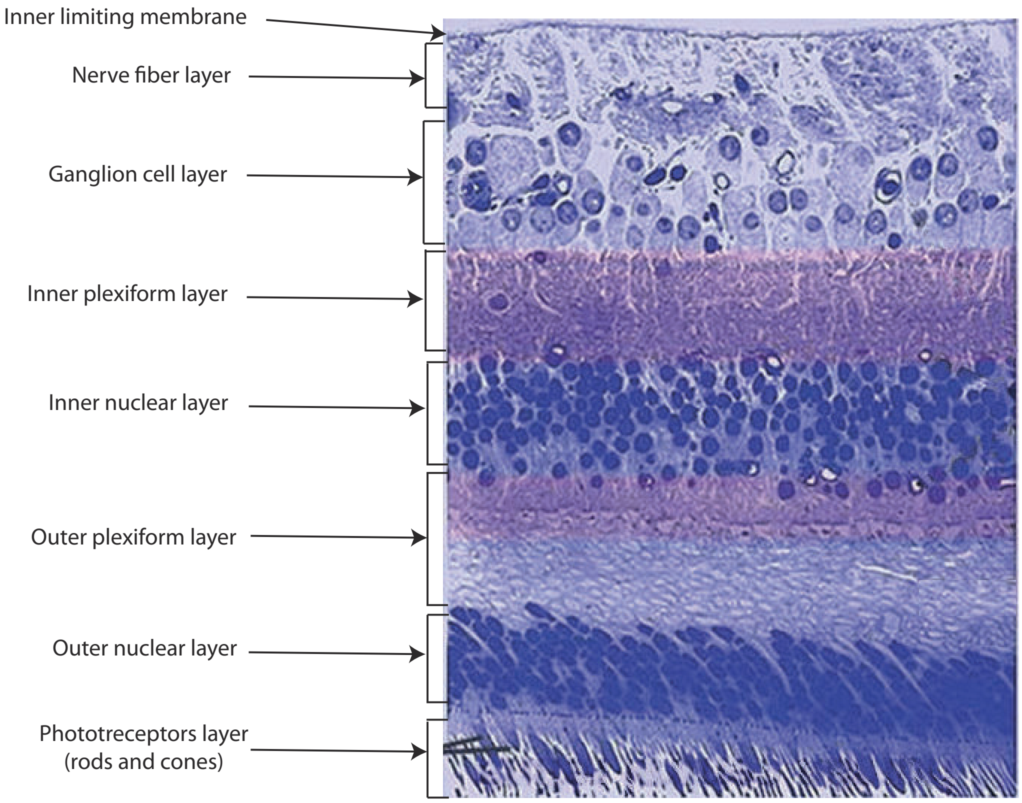

FIGURE 2.9: Light micrograph presenting a cross section of the retina, image modified from [Kolb].

Light passing through the cornea, lens and vitreous must pass through most of the retinal layers before reaching the light-sensitive portion of the photoreceptors; the outer segment in the receptor layer. In the region of the fovea where the image of the central visual field center is focused, the retina consists of fewer layers thereby minimizing the obstacles to forming a clear image on the fovea. The area around the fovea, the surrounding macula, is thicker because it contains the cell bodies and processes of retinal neurons receiving information from the receptors in the fovea.

The axons of the retinal ganglion cells form the nerve fiber layer of the retina on their course to the optic disc illustrated in Figure 2.8B. At the optic disc, these exit the eye and form the optic nerve. The fibers of the optic nerve that originate from ganglion cells in the nasal half of the retina cross in the optic chiasm to the opposite optic tract see Figure 2.8C. Consequently, each optic tract has within it axons representing the contralateral half of the visual field.

2.2.3 Retinal blood supply

Usually, the only arterial blood supply to the inner retina is from the central retinal artery that runs along the inferior margin of the optic nerve sheath and enters the eye at the level of the optic nerve head as illustrated in Figure 2.10A. Within the optic nerve, the artery divides to form two major trunks and each of these divides again to form the superior nasal and temporal and the inferior nasal and temporal arteries that supply the four quadrants of the retina. The retinal venous branches are distributed in a similar pattern. The major arterial and venous branches and the successive divisions of the retinal vasculature are present in the nerve fiber layer close to the internal limiting membrane as seen in Figure 2.10B. The retinal arterial circulation in the human eye is a terminal system with no communication with other arterial systems. Thus, the blood supply to a specific retinal quadrant comes exclusively from the specific retinal artery and vein that supply that quadrant. Any blockage in blood supply therefore results in infarction.

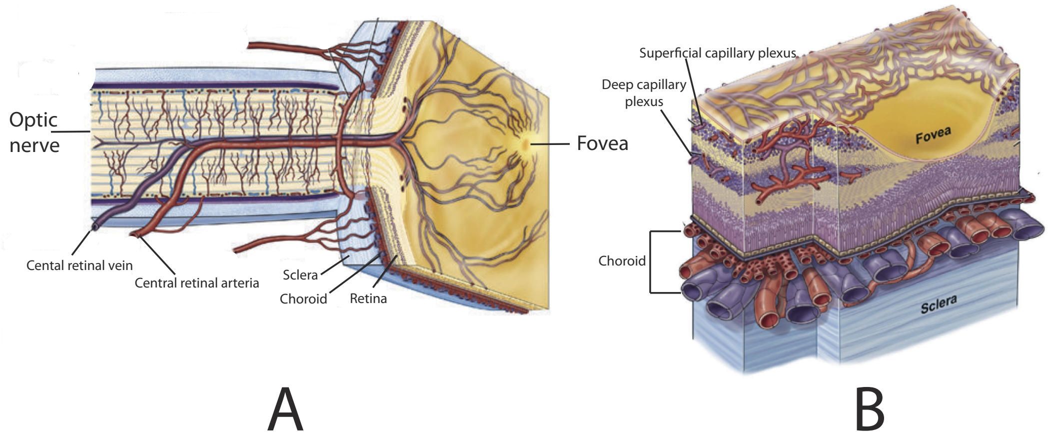

FIGURE 2.10: A. Drawing of the human eye along the superior–inferior axis through the optic nerve, showing the vascular supply to the retina and choroid. The retinal vessels are supplied by the central retinal artery. B. Drawing showing the vasculature of the retina and choroid. Retinal arterioles and venules lie on the vitreal surface of the retina while capillary plexi lie in just beneath the surface and in the inner nuclear layer. Drawings adapted from [Anand-Apte and Hollyfield, 2011]

The arteries and veins generated from the retinal arteries and veins form an extensive capillary network in the inner retina as far as the external border of the inner nuclear layer. This can be visualized in Figure 2.10B. The arteries around the optic nerve are approximately 100 μm in diameter with 18 μm thick walls. These decrease in diameter in the branched arteries located in the deeper retina to around 15 μm. The major branches of the central vein close to the optic disk have a lumen of nearly 200 μm with a thin wall made up of a single layer of endothelial cells having a thin basement membrane (0.1 μm) [Anand-Apte and Hollyfield, 2011].

2.2.4 Optic nerve head

The optic nerve has, by convention, been divided anatomically into four regions: intraocular, intraorbital, intracanalicular and intracranial. The first of these, the intraocular portion, is approximately 3 mm in length and is the focus of our research. Once the optic nerve exits the eye, there is an intraorbital portion. The optic nerve then passes into the optic canal - the intracanalicular. Upon exiting the optic canal, the nerve runs an intracranial course, until it reaches the optic chiasm. The optic nerve is enclosed in meningeal sheaths in its intraorbital and intracanalicular portions; these sheaths are continuous with those that line the brain. The intraocular portion of the optic nerve begins where 1.2 to 2.0 million ganglion cell axons converge and turn 90° to start their exit from the eye [Stedman'sMedicalDictionary, 2015].

The ONH illustrated in Figure 2.11 is the location where the ganglion cell axons leave the eye to form the optic nerve. There are no photosensitive cells at this region and is thus, insensitive to light and is called the blind spot. The optic nerve head also shows a number of large blood vessels as this is the location from which the vessels that supply the ocular tissue enter and leave the eye. The optic disc or ONH is a vertically oval structure containing a peripheral 'rim' composed primarily of neural tissue (as well as blood vessels and supporting cells) and, usually but not always, a more central depression known as the 'cup' that is devoid of neural tissue. The outer-most limit of the optic disc is known as the disc margin, and clinicians identify this landmark ophthalmoscopically as a reflective 'halo' or crescent at the innermost periphery of the neuroretinal rim. Clinicians usually refer to this sign, and therefore to the disc margin, as 'Elschnig's ring'. The disc margin represents an important landmark as it defines the extent to which neural tissue is confined to the ONH and as such is of central importance in defining the size of the ONH. It is also a key landmark in the quantification of structural parameters used in ONH imaging.

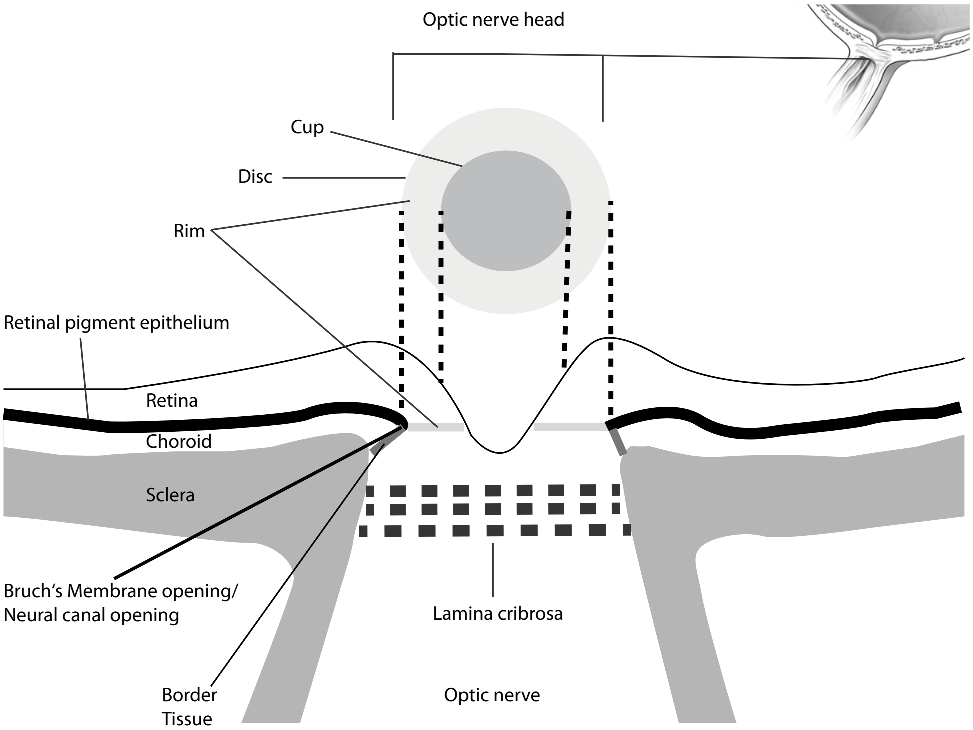

FIGURE 2.11: Anatomy of the optic nerve head, image modified from [Fuensanta and Doble, 2012].

There is considerable variability in optic disc size within populations, with disc area ranging from approximately 0.80 mm^2 to approximately 6.00 mm^2. Optic disc size has been observed to follow a near Gaussian distribution and in the non-highly myopic white population the mean optic disc area is 2.5 mm^2 . Men have larger optic discs than women. Optic discs are generally larger in black subjects, with average disc area being approximately 12% bigger compared to white subjects [Strouthidis et al., 2009a].

Bruch's Membrane Opening

The neural canal opening (NCO), see Figure 2.11, is a 3D planar structure that occurs at the level of the RPE and the Bruch's membrane (BM) and marks the anatomic entrance to the neural canal. This structure is referred to as the BMO in the literature and in non-human primate eyes, the NCO colocalizes to the BMO. The anatomy in humans is more complicated than in primates, and these separate structures can't truly be discerned in SD-OCT images [Strouthidis et al., 2009a], therefore we will use them interchangeably. The BM is the anterior surface of the choroid and the BMO is the location at which the optic nerve passes through this membrane.

The border tissue of Elschnig, see Figure 2.11, is a flange or strut of connective tissue arising from the sclera to meet BM and, in doing so, acting as the junction between the innermost termination of the choroid and the adjacent retinal ganglion cell axon bundles.

The lamina cribrosa, see Figure 2.11, is effectively a connective tissue 'scaffold' that anchors the bundles of optic nerve axons to each other and to the walls of the scleral canal. Along with the peripapillary sclera that surrounds the intraocular optic nerve, the lamina cribrosa represents the chief load-bearing tissue of the ONH [Strouthidis et al., 2009a].

2.3 Retinal imaging techniques

Retinal imaging has developed rapidly during the last years and is now widely used in the clinical care and management of patients with retinal diseases [Abràmoff et al., 2010]. In this section we present some of the main techniques utilized for the analysis of the retina and its structures.

2.3.1 Fundus photography

Fundus camera is a specialized microscope with an attached camera designed to photograph the interior surface of the eye – retina, fovea and ONH. These photographs allow medical professionals to monitor the progression of diseases like glaucoma and macular degeneration [Abràmoff et al., 2010]. The device automatically or manually detects the pupil center. In the next step the device automatically focuses to the retina, several images are scanned and the intensity of the patient's eye illumination is set. The images scanned are evaluated and the average intensity of the image is calculated [Abràmoff et al., 2010].

2.3.2 Stereo fundus photography

Stereo photography creates two images of the same subject taken from two positions, that of the photographer's left and right eye. After being processed, the images are then presented to the appropriate eye for viewing and the viewer's brain recreates the 3D view. The goal of this process is to recreate the image as if the viewer were at the site of the photographer. These images can be further used to create a 3D reconstruction of the ONH shape [Abràmoff et al., 2010].

2.3.3 Confocal scanning laser ophthalmoscopy

cSLO is an ophthalmic non-invasive imaging technology that uses laser light to illuminate the retina. The scanning laser ophthalmoscope uses a focused laser beam to scan over the area of the fundus to be imaged. At any instant only a small spot on the fundus is illuminated, and the light returned from this spot inside the eye determines the brightness of a corresponding point (pixel). If a pinhole, called a confocal aperture, is placed in front of the detector the image obtained is said to be confocal. The volume of tissue from which back scattered light is accepted by the confocal aperture is called a voxel. In the confocal mode, an image is built up of light scattered back from a layer of voxels, and the image is thus taken from a thin section of equal thickness to the depth of a voxel. In this way an optical section is produced, as light from structures outside the plane of the voxels will not contribute to the image [Woon et al., 1992].

2.3.4 Heidelberg retina tomograph

Heidelberg Retina Tomograph (HRT) is designed to scan the retinal surface with a diode laser, which has a wavelength of 670 nm. The precision of the method is based on the principle of confocality. The scanning process is vertical and horizontal, by multiple focal plans, generating a total of 64 sections, of 384×384 pixels each. If the focal plane is moved to different depths along the optic nerve and further optical sections are acquired, the result will be a layered 3D image (tomography). These sections are computer reassembled, making the calculation of the heights of different structures of the optic disc possible [Dascalu et al., 2010].

2.3.5 Optical coherence tomography

OCT first described in 1991, is a noninvasive imaging technique that can reveal layers of the retina by looking at the interference patterns of reflected laser light. OCT became widely popular in 2002 with the release of Stratus OCT, a time-domain technology (TDOCT). Only four years later, several companies started to release the next generation technology, SDOCT, which improved upon TDOCT by capturing more data in less time at a higher axial image resolution, around 5 μ m [Schuman, 2008]. OCT is frequently compared to ultrasound, because their basic principles are analogous, with OCT using light as its source. Both methods create a cross-sectional image by measuring the echo time delay and intensity of the reflected and backscattered light or ultrasound. OCT images use this information to depict variations in optical reflectance through the depth of the tissue along a point, creating what is known as an A-scan. These single axial scans through the tissue can be gathered linearly across the tissue, making one cross-sectional image, known as a B-scan, and a collection of parallel B-scans can be used to gather a 3D data set. OCT has a much higher axial resolution than ultrasound, 10 μm for TDOCT and 5 to 7 μm for SDOCT vs 150 μm for ultrasound at a frequency of 10 MHz.

Optical coherence tomography uses low-coherence interferometry to see the time difference corresponding to the distances between structures. The process starts with a broad-bandwidth laser or superluminescent diode low-coherence light source, the beam from which travels to a beam splitter. One half of the light goes to a mirror at a known position on a reference arm, and the other goes to the sample arm, where it is scattered and reflects off of tissue structures. Light from the reference and sample arms travels back to the beam splitter and recombines to form an interference pattern, which is sensed by a photodetector. The light beams combine constructively only if the light from the tissue and the light from the reference mirror are at almost exactly the same distance. The width of the signal envelope defines the resolution of the interferometer and is determined by the coherence length of the light used; the shorter the coherence length, the finer the resolution. The coherence length is dependent on the bandwidth, with broader bandwidths producing lower-coherence light [Schuman, 2008]. Figure 2.12 presents a schematic of an SDOCT system.

The advantage of SDOCT over TDOCT consists in the use of a stationary mirror, and the

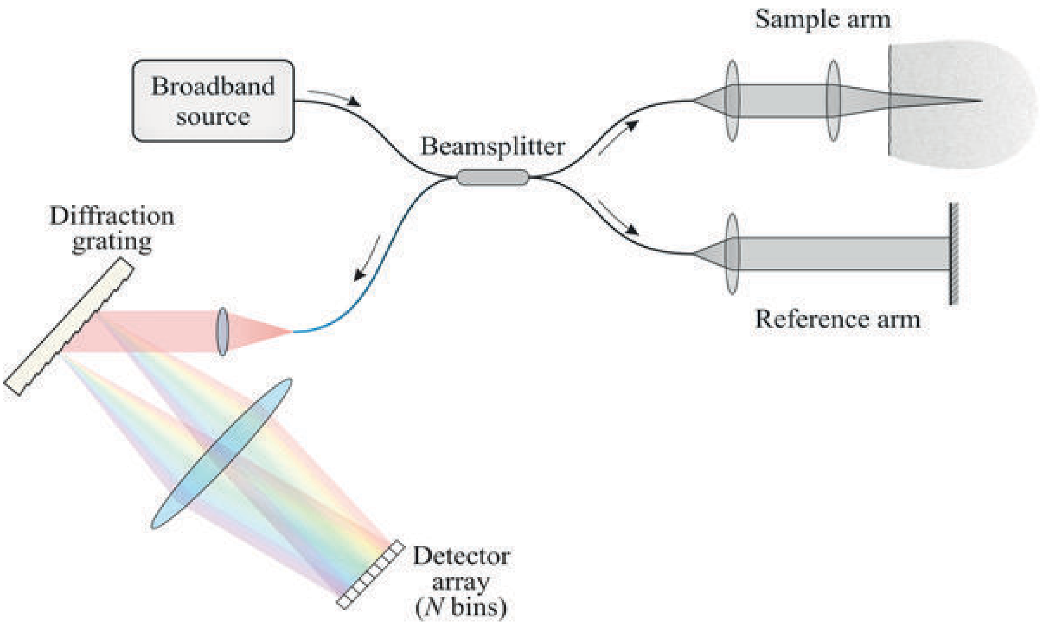

FIGURE 2.12: A. Schematic of a SDOCT system [OBEL].

interference pattern is split by a grating into its frequency components and all of these components are simultaneously detected by a charge-coupled device. The charge-coupled device has an array of photodetectors, each sensitive to a range of specific frequencies. Each frequency detected corresponds to a certain depth within the tissue after Fourier transform of the received signal, allowing all points along each A-scan to be gathered simultaneously, greatly accelerating scan speed.

Profiles of several A-scans can be observed in Figure 2.13. These A-scans can then be acquired along a transverse plane through the tissue and assembled into B-scans, as is done with TDOCT.

SDOCT is capable of acquiring 3D image data in a very short time. For example at 16,000 A-scans per second, SDOCT can acquire a B-scan image containing 2048 A-scans in 0.13 seconds [Schuman, 2008]. This faster speed allows for 3D data sets to be gathered, composed of a series of rapidly acquired B-scans. Figure 2.14 shows how a 3D scan is built upon several B-scans. These 3D data sets may be subject to motion artifacts in between B-scans, but as OCT technology improves, there is less movement artifact, since scanning time is shorter, and many SDOCT systems have also a built-in eye tracker.

With the 3D data sets, we can use 3D modeling, and detection tools to allow more intuitive visualization of the structure in the data set, similar to the 3D visualization tools created for

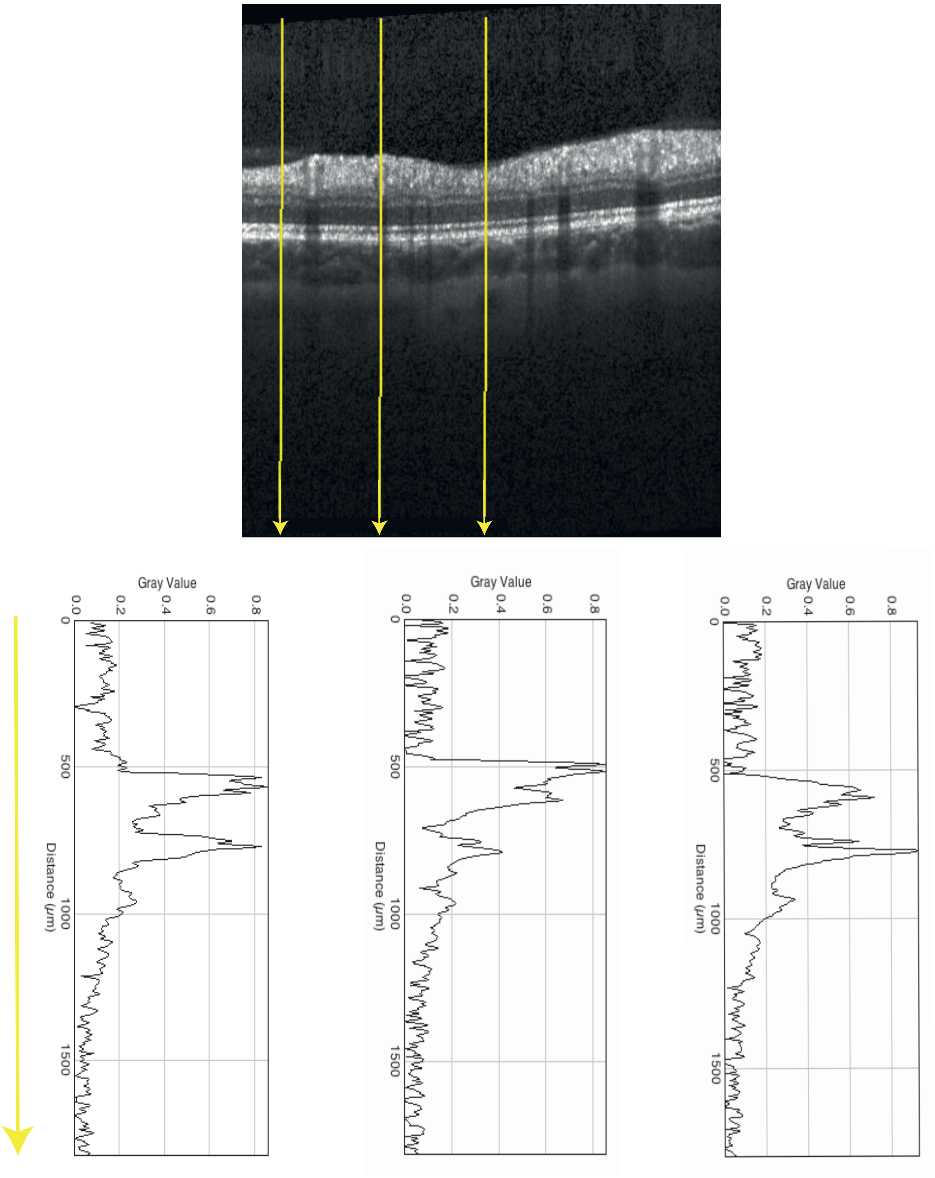

FIGURE 2.13: An optical coherence tomography cross-sectional image - B-scan (grayscale image) is built up from many A-scans.

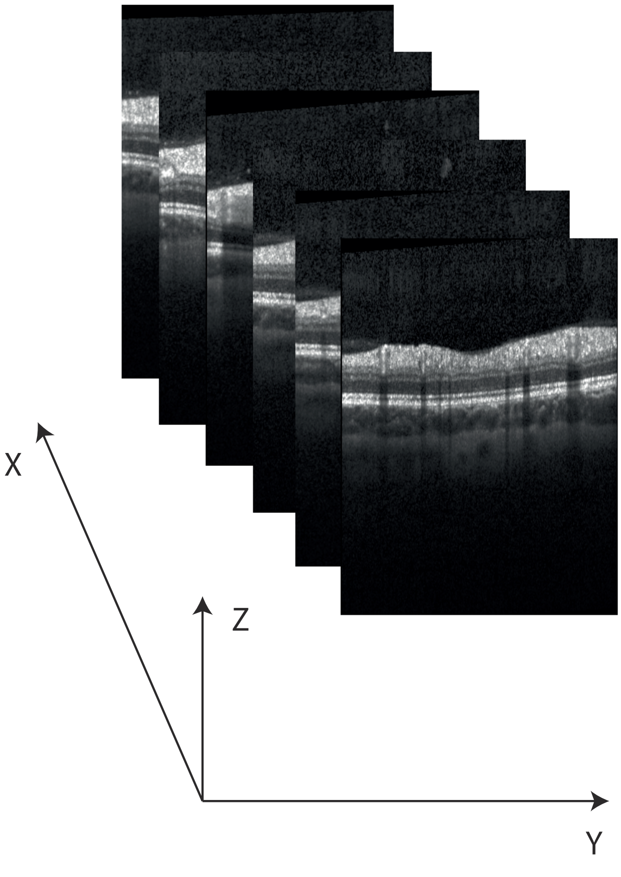

FIGURE 2.14: A 3D volume is built up from several B-scans.

magnetic resonance imaging or computed tomographic scans.

Currently, the most common four commercially available SDOCT devices in the US are: Cirrus HD-OCT (Carl Zeiss Meditec, Dublin, CA, USA), RTVue-100 (Optovue Inc., Fremont, CA, USA), Spectralis OCT (Heidelberg Engineering, Heidelberg, Germany), and Topcon 3D-OCT 2000 (Topcon Corporation, Tokyo, Japan).

2.4 Retina in neurological disorders and OCT parameters

The eye's retina, as part of the CNS with similar structure and cellular composition like the brain, has gained an important role in identifying structural changes that correlate with tissue-specific mechanisms of the CNS. SDOCT as described in 2.3.5, is a powerful imaging modality providing depth views of the retina. The application of image analysis tools in analyzing the retina range from initial differential diagnosis of several neurologic conditions, longterm control of changes to therapy monitoring. This scientific field is currently highly dynamic and covers many relevant diseases like MS, clinically isolated syndrome (CIS), NMOSD, Alzheimer's disease, Parkinson's disease, SUSAC syndrome, IIH. The main focus of our research is in MS, CIS, NMOSD and IIH.

2.4.1 Retina in MS

MS is one of the most common diseases of the CNS. It involves an immune-mediated process in which an abnormal response of the body's immune system is directed against the CNS, which is made up of the brain, spinal cord and optic nerves. There are four courses of the disease: relapsing-remitting MS (RRMS), secondary-progressive MS (SPMS), primary-progressive MS (PPMS), progressive-relapsing MS (PRMS). Today, approximately 2 500 000 people around the world have MS, and more than 140 000 in Germany. Despite the high costs for the treatment per patient and per year there is no drug that can cure MS, [DMSG]. Acute ON is the presenting symptom in 15%–20% of MS patients and occurs in up to 70% of patients during the course of the disease [Balcer, 2006]. ON is an inflammatory attack to the optic nerve. After initial swelling due to edema in the acute phase, degeneration of the retina especially in the RNFL occurs [Albrecht et al., 2007]. Figure 2.15 shows the segmented retinal layers from a macular volume OCT scan.

Standard parameters of the assessment of structural changes of the retina in MS are the peripapillary RNFL thickness from a ring scan centered at the ONH and total macular volume (TMV) of all layers. OCT ring scans with their corresponding B-scan are presented in Figure 2.16. The first OCT data from MS patients were reported in 1999. With the new generation of SDOCT, retinal imaging with enhanced resolution, and 3D scans, it is possible to detect even subtle changes in the range of a few μm. Consequently, different layers from intraretinal layer segmentation see Figure 2.15, besides the RNFL, like GCL, often combined with the IPL, (GCIPL), became an important outcome parameter in OCT studies in MS [Saidha et al., 2011]. Numerous OCT studies consistently found that ON leads to significant thinning of the RNFL with a mean RNFL reduction of approximately 20 μm after ON, which corresponds to a 20% loss in RNFL thickness [Petzold et al., 2010].

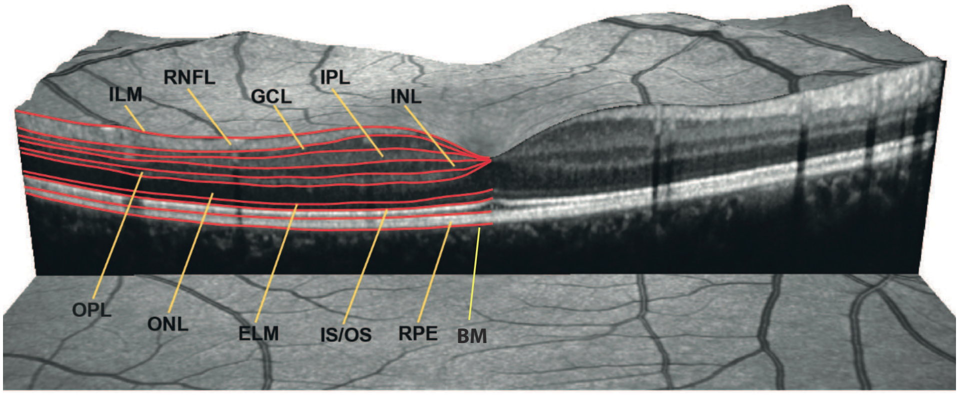

FIGURE 2.15: Retinal layer segmentation in a 3D spectral domain optical coherence tomography scan of the macula [Oberwahrenbrock et al., 2013].

Even in the absence of ON, it had been shown that the RNFL is about 10 μm thinner when compared to that of healthy controls [Talman et al., 2010].

Also recent SDOCT study in a cohort of CIS patients showed that degeneration of retinal neurons occurs very early in the course of the disease [Oberwahrenbrock et al., 2013].

Although still a very active research topic, many studies have shown relationship between RNFL and GCIPL thickness reduction and several MRI-derived measurements of brain atrophy [Gordon-Lipkin et al., 2007, Zimmermann et al., 2013].

Cerebral veins gained increasing attention in MS. A concept termed CCSVI [M. and Z., 2012] was introduced suggesting that compromised cerebral venous outflow might contribute to MS pathology. However, several studies could not confirm cerebro-cervical venous congestion,

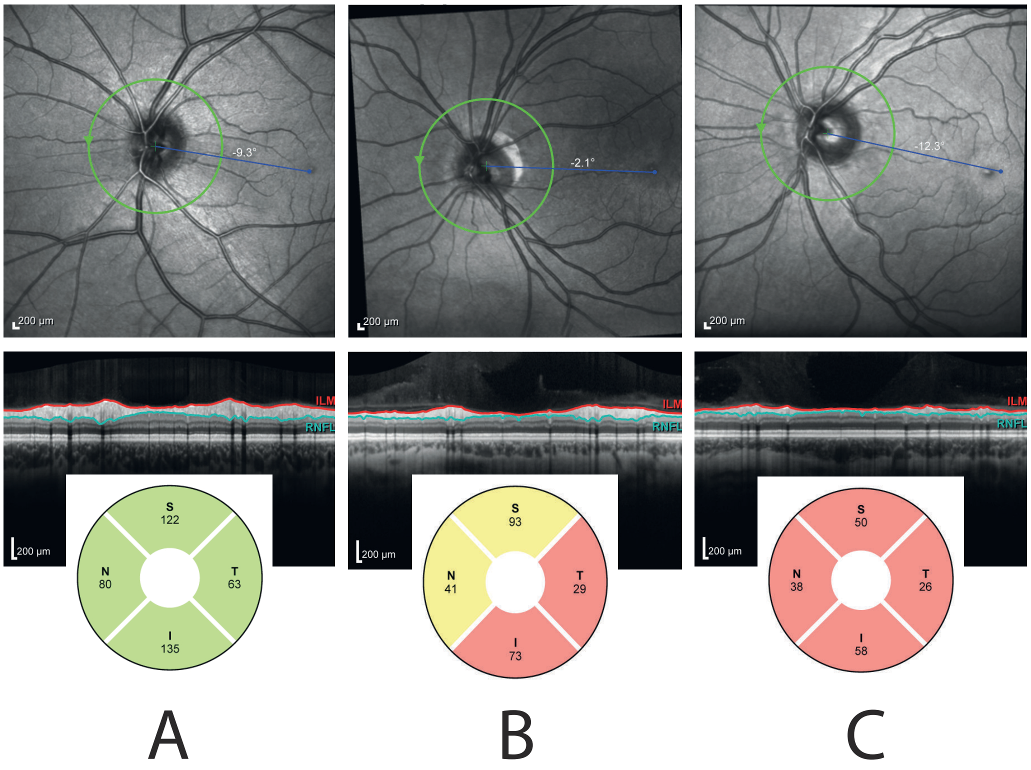

FIGURE 2.16: Comparison between HC (A), MS (B) and NMOSD (C) for RNFL thickness. The RNFL thickness is usually acquired by a peripapillary ring scan. Image analysis provides the thickness values for the overall ring, but also for the sectors: S - superior, N - nasal, I - inferior, T - temporal. A, B, C - SLO images with ring scan (green circle), and the B-scan of the acquired ring, RNFL thickness is measured between ILM (red line) and RNFL(blue line). Peripapillary RNFL thickness values in different sectors. Black numbers display the sectoral mean thickness measurements of the subject; Sectors are classified in comparison to the reference group. Green: thickness values within the fifth and 95th percentile range. Yellow: first to fifth percentile range. Red: less than the first percentile.

but instead showed either normal or reduced veins compared to HC. Yet, little is known about retinal veins in MS to support or object the CCSVI hypothesis.

In summary, the retinal imaging in OCT, in MS has allowed for assessment of structure-function correlations that make the anterior visual pathway and acute ON ideal models for testing novel agents for neuroprotection and repair but are also promising for clinical routine [Sakai et al., 2011].

2.4.2 Retina in NMOSD

Both NMOSD and MS are neuroinflammatory diseases with acute ON as a characteristic or even crucial manifestation [Zimmermann et al., 2014]. NMOSD frequently presents bilaterally and even simultaneously ON and visual impairment is often more severe and the risk of recurrence is higher than in MS. RNFL reduction after ON is more pronounced in NMOSD than in MS (55–83μm versus 74–95 μm, respectively) [Syc et al., 2012] see Figure 2.16C.

To our knowledge the only study that addresses retinal vasculature involvement in NMOSD is from [Green and Cree, 2009]. In this study vascular changes were found, including attenuation of the peripapillary vascular tree and focal arteriolar narrowing. These findings show that some of the injury seen in NMOSD may be vascularly mediated. These inner retinal vascular changes are reminiscent of blood vessel wall thickening previously reported in the optic nerve and spinal cord at autopsy, suggesting that vascular changes may be detectable during life [Green and Cree, 2009].

2.4.3 Retina in IIH

IIH, also known as pseudotumor cerebri, is a clinical syndrome of unknown etiology characterized by increased intracranial pressure (ICP) which typically affects young, obese women of childbearing age. Clinical symptoms include headache, visual disturbances, pulsating tinnitus, photopia, eye pain, diplopia and nausea. Papilledema with subsequent visual field loss is the most feared clinical consequence, which mainly determines the therapy and outcome of the syndrome. Patients with newly diagnosed IIH presented RNFL thickening compared to healthy controls, which decreased after three months under IIH treatment, visible and quantifiable in the ring scan with OCT [Heidary and Rizzo, 2010]. 3D SDOCT, ONH center scans, provides the possibility to quantify the whole volume of the swelling. The swelled ONH region in IIH patients presents as an extreme elevation of the ONH with varying sizes. Intraretinal layers are hardly recognizable due to edema as in can be observed in Figure 2.17.

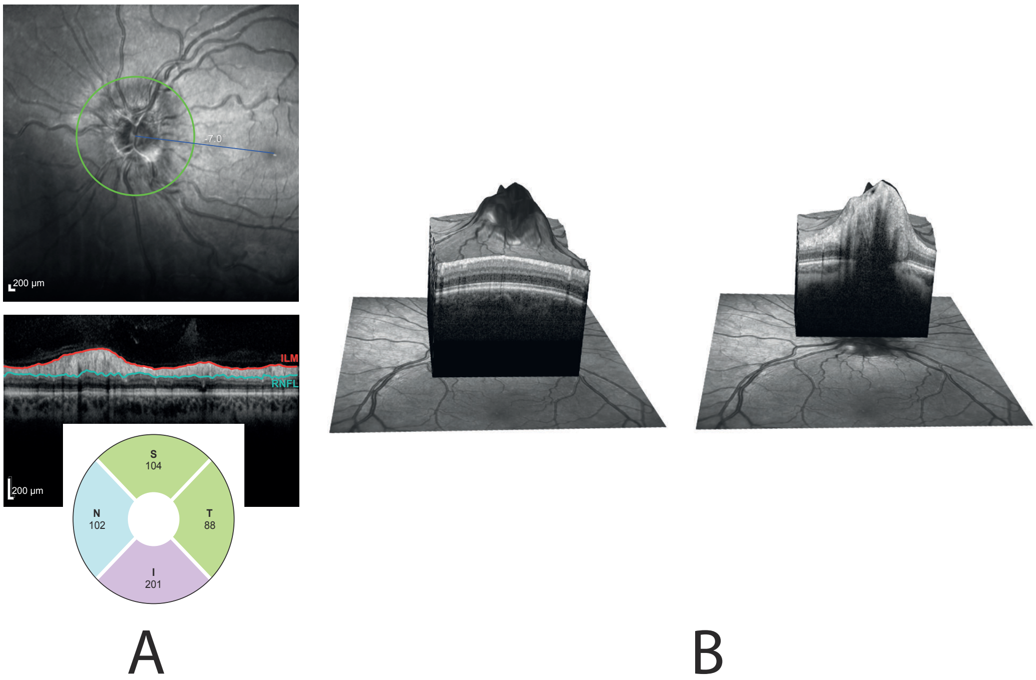

FIGURE 2.17: A. SLO images with ring scan (green circle), and the B-scan of the acquired ring, and peripapillary RNFL thickness values in different sectors. S - superior, N - nasal, I - inferior, T - temporal. A, B, C - SLO images with ring scan (green circle), and the B-scan of the acquired ring, RNFL thickness is measured between ILM (red line) and RNFL(blue line). Peripapillary RNFL thickness values in different sectors. Black numbers display the sectoral mean thickness measurements of the subject; Sectors are classified in comparison to the reference group. Green: thickness values within the fifth and 95th percentile range. Blue: last fifth percentile range. Violet: more than the last percentile. B. 3D SDOCT ONH volume scan showing the extreme elevation due the swelling.

2.5 Data and optical coherence tomography device used in our research

All data, patients and HC, was obtained at the NeuroCure Clinical Research Center at the Charité- Universitätsmedizin Berlin.

All images in our research were acquired with Spectralis OCT from Heidelberg Engineering (Spectralis software version used 5.3.3.0, Eye Explorer software 1.6.4.0), an SDOCT system. The Spectralis system is 100 times faster than TDOCT and acquires 40,000 A-scans per second. It has integrated into its system cSLO fundus imaging, which not only offers the possibility of a new perspective of the retina, but also enables accurate and repeatable alignment of OCT for repeated measurements of the same subject. High speed image acquisition is combined with custom TruTrack^{TM} technology to actively track the eye during imaging. This technology minimizes motion artifact and enables noise reduction.

Chapter 3

Retinal blood vessel segmentation

In this chapter two algorithms are presented: a semi-automated tool for the detection of the inner and the outer boundary of retinal blood vessel at 15 positions for each blood vessel in the close vicinity of the ONH, and three fully automated approaches to detect the whole retinal vasculature. Until recently, the study of retinal vessel diameters for clinical purposes has remained largely a research tool because it is laborious, although improvements in the computerized analysis have the potential to change this [Zheng et al., 2009]. The semi-automated algorithm described here was developed to offer a practical alternative to manual measurements for a wide range of studies in neurological disorders using cSLO images, while offering important benefits in terms of robustness and repeatability. The fully automated algorithm presenting three approaches for the detection of the entire vasculature in cSLO images centered on the ONH arised from a technical need of extracting possible landmarks for further registration purposes, as blood vessels and blood vessel crossings, can provide unique features for follow-up registrations of the ONH.

3.1 Previous approaches in retinal blood vessel segmentation

Many studies on 2D segmentation of retinal blood vessels from a variety of medical images have been performed [Nayan and Deshpande, 2015]. Vessel segmentation algorithms are critical components of circulatory blood vessel analysis systems [Abràmoff et al., 2010]. Most of the techniques presented in this section were developed to quantify retinal vascular disorders studied in ophthalmology and use fundus photographs. These disorders include hypertensive retinopathy (high blood pressure causing narrowing of blood vessel), retinal vein occlusion (causing narrowing or obstruction), diabetic retinopathy (causing damage that in most cases leads to blindness). Manual segmentation of retinal blood vessels is a time consuming and tiresome task which also requires skill and training, consequently the need for automatic tools [Nayan and Deshpande, 2015].

Vessel network in Fundus photography

Typical edge detection techniques, such as Sobel operator, Canny border detector, and Prewitt operator are not appropriate for vessel detection [Nayan and Deshpande, 2015]. In fundus photographs more than one processing algorithm is needed to acquire acceptable results, and before segmenting the image it is convenient to do preprocessing tasks. One common preprocessing task is to obtain the grayscale image from the green channel [Nayan and Deshpande, 2015]. Generally, blood vessels are darker than the background, although there are areas where the vascular network is not visible because its level is similar to the background. Several studies showed that the green channel saves the best pixel information. Contrast enhancement is also one of the most common preprocessing tasks, performed in both healthy and pathological retinal images [Nayan and Deshpande, 2015].

Existing vessel segmentation techniques on the conventional fundus photographs can be divided into several major categories: matched filter based, thresholding based, region growing based, model based, tracking based, multi-scale based, and classification based methods.

The matched filter (MF) method consists in convolving the image with a directional filter designed according to the vessel profile. The kernel is created to model a feature in the image at some unknown orientation and position. The MF response indicates the presence of the feature. The following properties are utilized in order to design the matched filter kernel: the diameter of the vessels decreases as they move radially outward from the optic disk; the cross-sectional pixel intensity profile of these line segments approximates a Gaussian curve; vessels usually have a limited curvature and may be approximated by piece-wise linear segments. [Chaudhuri et al., 1989] proposed a method based on a 2D Gaussian filter. [Gang et al., 2002] designed different filter parameters to increase the MF based on a second-order Gaussian filter. The MF can be used as the first step for other segmentation methods. The filter response enhances the vessel pattern features, thus improving the performance of thresholding or tracking processes. [Hoover et al., 2000] introduced a piece-wise thresholding probe algorithm on the MF response image to improve the accuracy of the segmentation. [Zhang et al., 2015] proposed a novel extension of the MF approach namely the MF-FDOG to detect retinal blood vessels. The MF-FDOG is composed of the first-order derivative of Gaussian (FDOG). The vessels are detected by thresholding the retinal image's response to the MF and the threshold is adjusted by the image's response to the FDOG. Compared with the MF, the MF-FDOG can better distinguish the true vessel structures from non-vessel structures such as blobs and lesions. The MF provides high quality results, but the main disadvantage of these methods is their requirement for vessel profiles computation to compare large regions for each pixel in the image, resulting in long computational time. Also MF alone cannot handle vessel segmentation in pathological retinal images, therefore it is often employed in combination with other image processing techniques.

[Soares et al., 2006] applied complex Morlet filters for feature extraction and supervised classification for the detection of blood vessels in retinal fundus images. In this method the magnitude outputs at several scales obtained from 2D complex Morlet filters were assigned to each pixel as a feature vector. Then a Bayesian classifier was applied for classification of the results into vessel or no vessel pixels.

The performance of algorithms based on supervised classification is better in general than the unsupervised ones. However, these methods do not work very well on images with nonuniform illumination as they produce false detection. They also fail in some images on the border of the optic disc, or that present hemorrhages and other types of pathologies [Nayan and Deshpande, 2015].

Vessel tracking algorithms are more robust in those situations [Quek and Kirbas, 2001]. They try to find a vessel-like structure in the already segmented region and track the given vessels. These algorithms can recognize vessel endings much easier, but they may have difficulties at bifurcations and vessel crossings, where the local structures do not look like usual vessels anymore.

As already mentioned, a main characteristic of the retinal blood vessels is that their width decreases as it travels radially outward from the optic disk and such a change in vessel caliber is a gradual one. Therefore methods employing a scale-space representation for vascular extraction have been extensively used in order to separate out information related to the blood vessel having varying width at different scales. [Dizdaro et al., 2012] proposed a *vesselness* measure that extracts tubular structures based on the basis of the eigenvalue analysis of the Hessian. In their approach the principal directions in which the local second order structure of the image can be decomposed, are computed. The direction of the smallest curvature along the vessel is further employed for the final segmentation.

Hessian-based filters, however, can not distinguish step edges from vessels effectively. MF provide a better result in these cases. To solve the problem of false detection of edges, [Sofka and Stewart, 2006] proposed an algorithm using the edge information at the boundary of vessels. A vessel should have two edges, one on each side of it. This property can be used to effectively distinguish between vessels and edges in the image. The proposed enhancement filter combines the advantages of Hessian based filters, MF, and edge information.

[Martínez-Pérez et al., 1999] presented a method based on the scale-space analysis of the first and second derivative of the intensity image which gives information about its topology and overcomes the problem of variations in contrast inherent to retinal images. The local maximum over scales of the magnitude of the gradient and the maximum principal curvature are used as features for a region growing procedure. The growth is constrained to regions of low gradient magnitude and then the borders between regions will be defined by growing vessel and background classes without gradient restriction.

One of the disadvantages of multi-scale methods is the computational requirement. To overcome this problem [Budai et al., 2013] presented an algorithm based on the vessel enhancement method published by [Frangi et al., 1998] in combination with a multiresolution framework to decrease the computational needs and to increase the sensitivity by using a hysteresis thresholding. The evaluation on the public databases DRIVE [DRIVE] and STARE [STARE] showed that the proposed algorithm increased in both sensitivity and accuracy compared to Frangi's method while reducing the computational complexity.

Blood vessel network in cSLO

Color images provide much more information, which is not available in cSLO images. The algorithms in previous studies did not work satisfactorily on cSLO image due to the low global/local contrast, non-uniform illumination and noise. Segmentation based on the cSLO images is focused on detecting only the main vasculature and branching points for the registration purposes and motion artifacts correction that occur during eye movement. The method proposed in [Ricco et al., 2009] is a simplified implementation of the technique based on MF, which uses hysteresis thresholding to find ridges in the divergence of the image gradient.

The only work that approached the segmentation directly from the cSLO images is by [Xu et al., 2008]. Their approach is a hybrid algorithm using MF, mathematical morphology, contrast enhancement and thresholding probe for segmentation. The results of this method were not compared to a ground truth data set, but rather presented in an experimental set-up, by focusing on the potential this method has in providing a vessel map for registration purposes.

Unfortunately there is no ground truth data for cSLO images, as most of the algorithms are based on fundus photographs for which there are two main public available databases (DRIVE [DRIVE] and STARE [STARE]).

Contributions

In our semi-automated tool, in order to account for the strong central reflex seen in cSLO images, especially in large vessels, we developed a new filter response, based on MF, one of the most commonly used methods in vessel segmentation in fundus photographs [Chaudhuri et al., 1989, Gang et al., 2002, Hoover et al., 2000, Zhang et al., 2015]. This new approach is based on a double Gaussian directional filter and it is able to model the vessel profile containing the central reflex in different orientations, providing a better feature response compared to the previous filters for fundus photographs.

We also tested our algorithm in a clinical study, to test the hypothesis of CCSVI in MS, details of the results are presented in Subsection 3.2.3, and were presented at the ECTRIMS conference in 2013 [Kadas et al., 2012b].

In the second, fully-automated approach, we first extended the work of [Weickert, 1999] on coherence diffusion enhancement to adapt the diffusion tensor introduced in Section 2.1.3 to the local structure of the image. By deriving a *vesselness* map containing the enhanced blood vessels based on the eigenvalues of the structure tensor we compute the percentage of the vessels in the image and therefore the texture characteristics of the image. In a similar manner we use a different map, the coherence response, to establish a threshold for isotropic structures. Based on the enhanced vessel image we propose three methods to extract the entire vasculature. All three approaches extend known approaches by addressing different challenges or known problems as follows:

- Approach 1. extends the work proposed by [Soares et al., 2006] in using a 2D Morlet wavelet filtering by making use of the principal curvature of the Hessian tensor in cases of large vessels with a strong central reflex

- Approach 2. proposes a method to account for the weak response of the well-known Frangi's *vesselness* filter in cases of vessel crossing by incorporating information of vessel directionality from the eigenvectors of the Hessian tensor
- Approach 3. extends the OOF response, on the vessel boundaries, using a combination of the eigenvalues and eigenvectors of the Hessian tensor of the OOF, in order to detect not only the vessel centerline but also its boundary.

3.2 Semi-automated tool for detection of blood vessel inner and outer diameter in cSLO images

The vessel diameter detection algorithm presented in this subsection was developed to detect the retinal blood vessel inner and outer diameter in cSLO images, centered at the ONH which accompany the peripapillary ring SDOCT scan, see Subsection 2.4.1, and have an image size of 1536×1536 pixels with a resolution of 6 μm/pixel. The steps of the algorithm are provided in Figure 3.1.

The cSLO image, unlike the standard retinal photographs (5 MPixel (2592×1944)), has a lower resolution with non-uniform illumination, low global/local contrast and high background noise, which makes vessel segmentation on cSLO images a challenge. Blood vessels usually appear darker relative to the background in cSLO images due to lower reflectance compared to the retinal surface. They have small curvatures that may be approximated by piece-wise linear segments, a characteristic that was integrated into our method. Another important aspect of the vasculature in cSLO images is the strong light reflex along vessels centerline, see Figure 3.2A, compared to fundus photographs see Figure 3.2B. The presence of the central reflex makes algorithms developed for fundus photographs, presented in Section 3.1, unsuitable.

The algorithm creates three concentrical circles centered on the ONH of diameter 3.2 mm, 3.4 mm and 3.8 mm. The circle of 3,4 mm represents the ring scan of the OCT device, at which position the RNFL thickness is measured, a well established parameter in order to detect nerve fiber degeneration, see Subsection 2.4.1. The center of the ONH is already provided by the

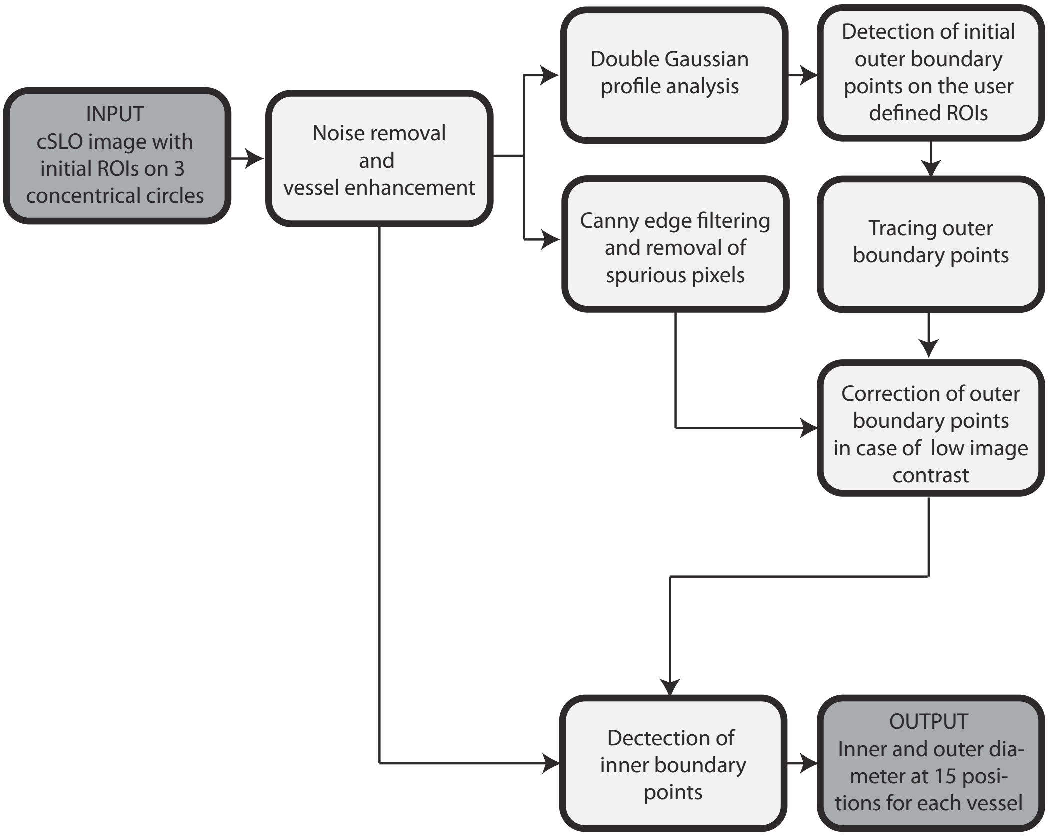

FIGURE 3.1: Illustration of the semi-automated blood vessel inner and outer diameter algorithm's steps.

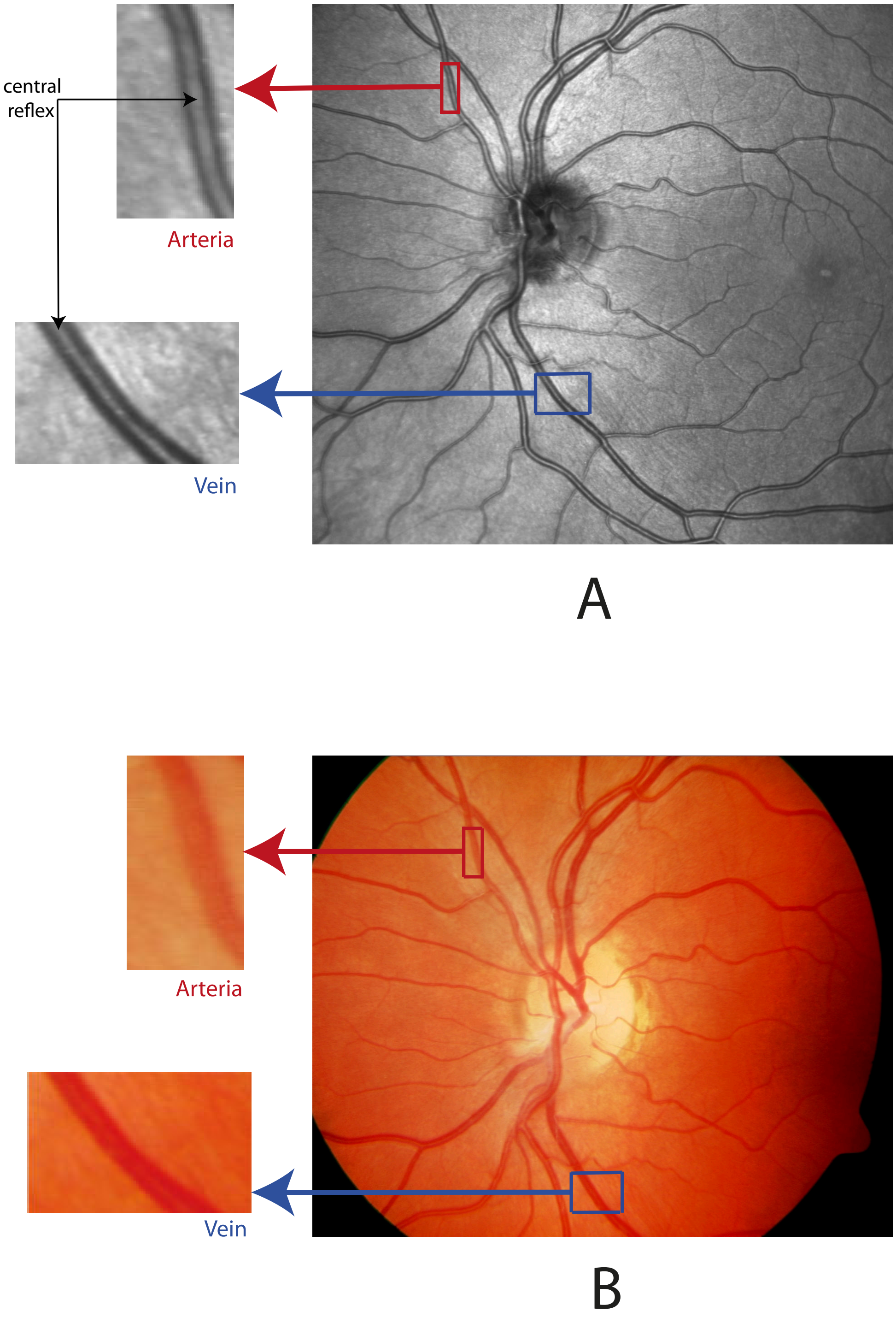

FIGURE 3.2: A. cSLO image showing a part of a vein and a part of an arteria with central reflex B. Fundus photograph of the same subject image showing the same part of a vein and a part of an arteria as in A. Note the lack of the central reflex.

center of the circle with 3.4 mm from the OCT device. The user labels the vessels intersecting the circle in arteries (a), veins (v) and unknown (u) see Figure 3.3 according to the following criteria [Motte et al., 2014]:

- arteries close to the ONH are brighter than veins
- arteries are usually thinner than their neighboring veins
- arteries and veins alternate near the optic disc
- arteries never cross arteries and veins never cross veins
- arteries take a straighter course than veins
- vessels coming from a branching of another already classified vessel is labeled from the parent vessel
- vessels that do not meet the criteria from above are labeled with unknown

The user then marks a region of interest (ROI) line using the ImageJ ROI Manager, perpendicular on the labeled vessel's profile, at the position of the intersection with the three circles, see Figure 3.3.

Noise removal and vessel enhancement

Due to the low contrast in the cSLO image, blood vessels are difficult to detect by only a single global threshold. To overcome the low contrast without introducing artifacts from non-uniform illumination specific to cSLO images, a contrast enhancement process is applied only in a 10 $mm \times 10$ mm square centered on the ONH. Contrast limited adaptive histogram equalization (CLAHE) [Zuiderveld, 1994] is used for contrast enhancement by limiting the maximum slope in the transformation function. It targets small regions in the image, called tiles, rather than the entire image. Each tile's contrast is enhanced. The size of a tile is set to 25 pixels, in order to limit noise amplification that might be present in the image, especially in areas with pixels that have similar intensity, like the non-vessel area, and to ensure that the tile size is larger than the diameter of a vessel itself. The parameter of the maximum slope is set to 2.5 to enhance the contrast between vessel wall compared to the background. The result of applying CLAHE on the original vessel Figure 3.4A is shown in Figure 3.4B.

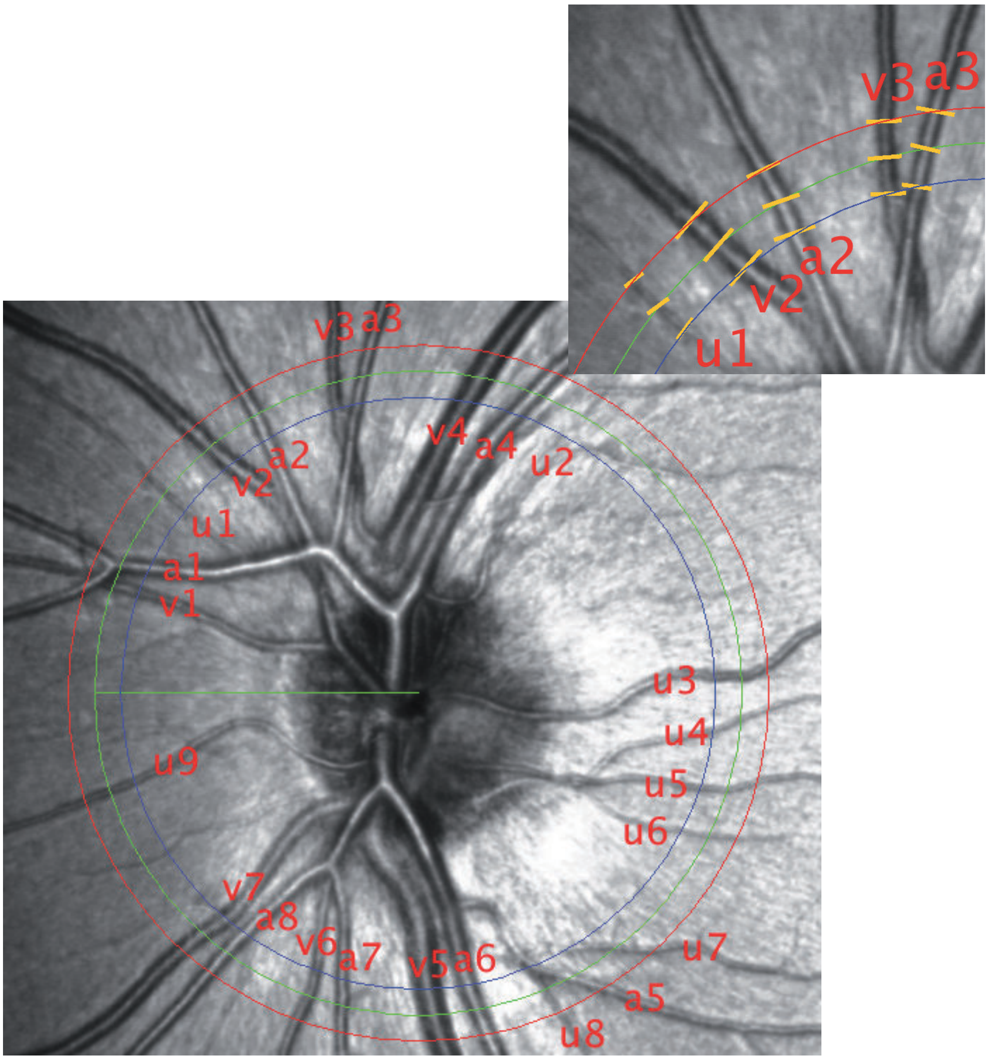

FIGURE 3.3: The region of the cSLO image that will be used for the computations performed by the vessel diameter detection algorithm with the 3 concentrical circles centered on the ONH and the labeled vessels by the user with a zoomed in region of the user defined initial ROIs at each labeled vessel.

To reduce the speckle noise present especially in the non-vessel areas, which considerably affects the accuracy of the vessel wall detection, we applied a well established technique, anisotropic diffusion [Perona and Malik, 1990], to constrain the diffusion process to contiguous homogeneous regions, but not cross region boundaries. The number of iterations was set to 15, and the threshold height to 0.5 based on the histogram in a small window of 20×20 pixels around the selected vessel ROI, which showed that vessel walls usually have an intensity that is half of the background intensity. The result of applying this filter is shown in Figure 3.4C.

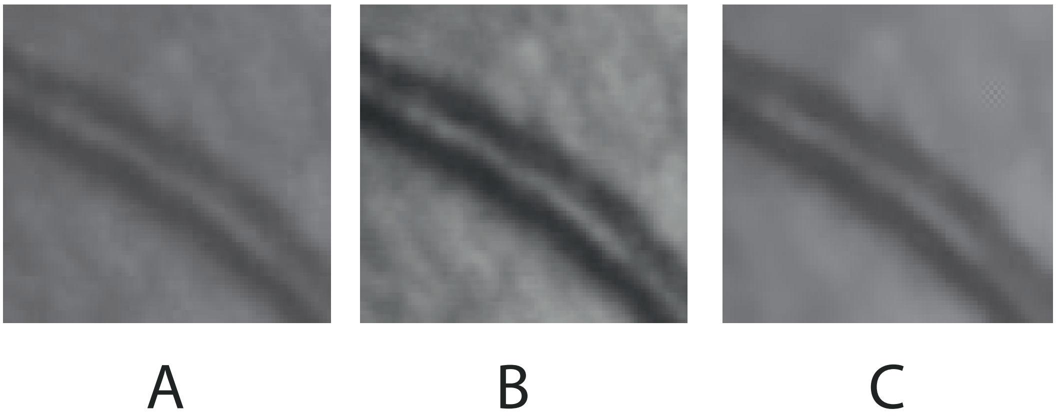

FIGURE 3.4: A. Part of a vessel with a slight curvature. B. The response of applying contrast limited adaptive histogram equalization. C The response of the anisotropic diffusion.

3.2.1 Double-Gaussian profile analysis

To account for the central reflex present in cSLO images, see Figure 3.5A, for an example of an artery and Figure 3.5B for an example of a vein, we created a double-Gaussian (DG) model. This model is used to imitate the vessels central light reflex that extends the Gaussian shaped MF used in fundus photographs, see Figure 3.6A. Gaussian shaped matched filter and its extension has been used for vessel detection before in fundus images [Chaudhuri et al., 1989]. The profile of the filter which is designed to match that of a blood vessel is defined as

$$f(x, y) = h_1 \frac{1}{\sqrt{2\pi}\sigma_1} \exp\left(\frac{-(x\cos\theta + y\sin\theta)^2}{2\sigma_1}\right), \tag{3.1}$$

for $|x| \leqslant (t \cdot \sigma_1), y \leqslant \frac{L}{2}$, where, σ represents the scale of the filter; L is the length of the neighborhood along the y-axis; h_1 is a constant representing the height of the Gaussian curve, θ is the rotation angle of the filter kernel and t is a constant and is usually set to 3 because more

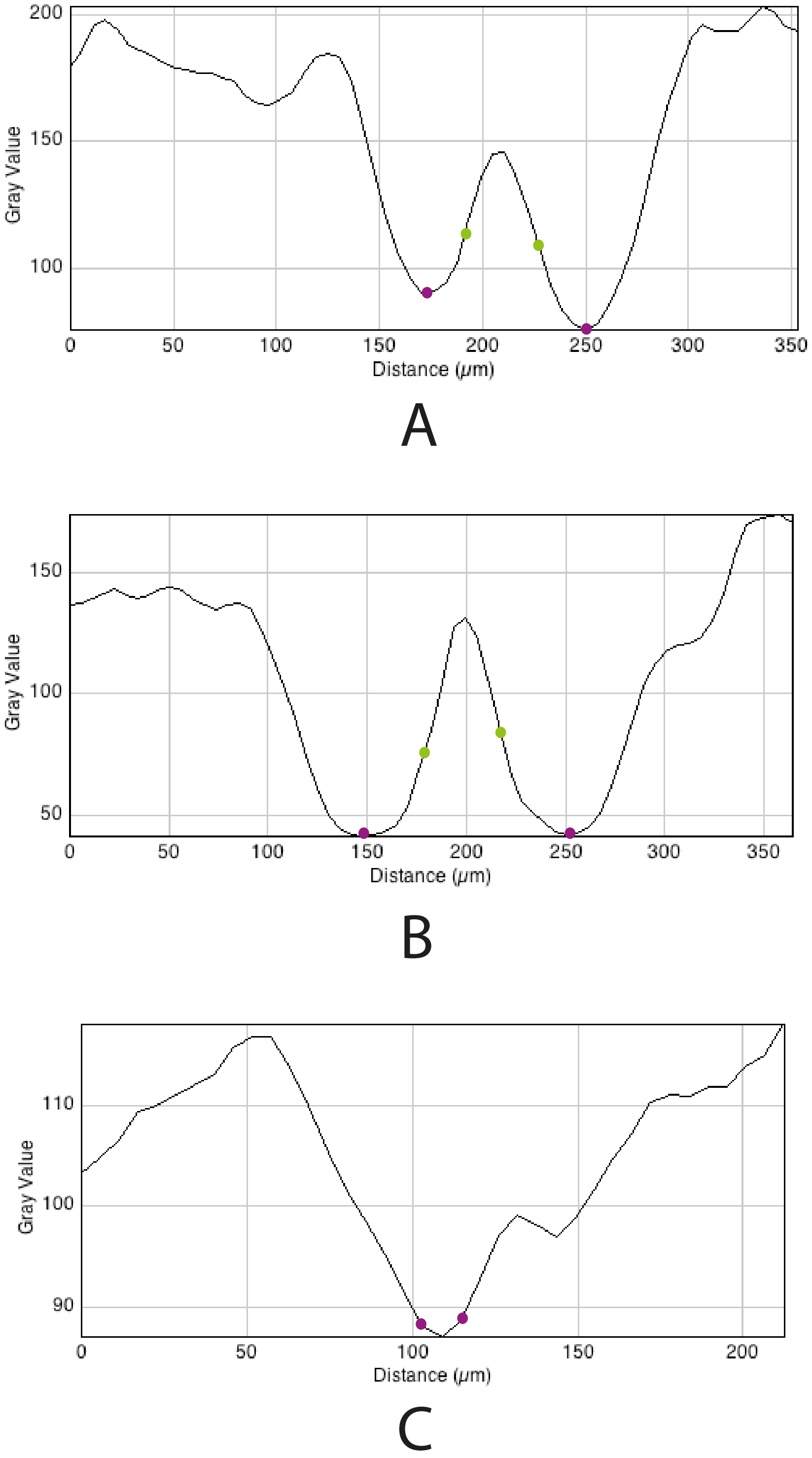

FIGURE 3.5: A. Cross section of an artery. B. Cross section of a vein. C. Cross section of a vessel classified as unknown. Magenta points represent the outer boundary points; green points represent the inner boundary points. These points are an example of manually defined outer/inner diameter by the user and represent the positions that our algorithm should detect as outer/inner boundary points.

than 99% of the area under the Gaussian curve lies within the range $[-3\sigma, 3\sigma]$. Figure 3.6B shows the cross section model profile for a vessel without a central reflex. This model for the vessel profile is however unsuited for the central reflex seen in vessels in cSLO images. For this purpose, in our DG filter a second small Gaussian curve is subtracted from the main Gaussian curve. The second Gaussian is oriented at the same angle and controlled by same parameters as the first one see Figure 3.6A . The parameters of the second Gaussian control the height and width of central light reflex and the matched filter kernel is expressed as:

$$f(x,y) = h_1 \frac{1}{\sqrt{2\pi\sigma_1}} \exp\left(\frac{-(x\cos\theta + y\sin\theta)^2}{2\sigma_1}\right) - h_2 \frac{1}{\sqrt{2\pi\sigma_2}} \exp\left(\frac{-(x\cos\theta + y\sin\theta)^2}{2\sigma_2}\right) \tag{3.2}$$

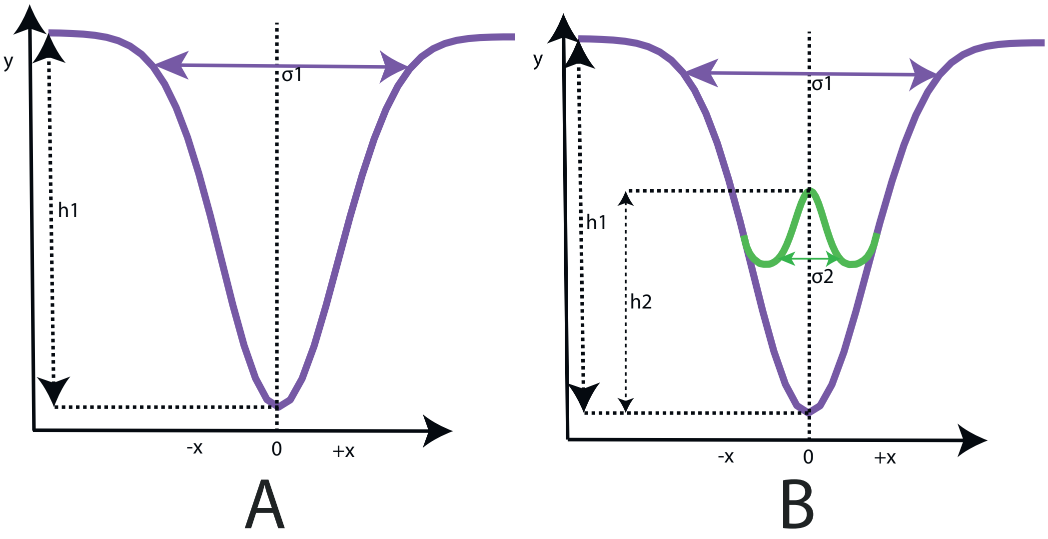

FIGURE 3.6: A. Cross section of vessel model profile without central reflex, σ_1 represents the scale, h_1 the height of the Gaussian curve used to model the profile. B. Cross section of vessel model profile with central reflex, σ_1 represents the scale, h_1 the height of the Gaussian curve used to model the profile, σ_2 represents the scale, h_2 the height of the second Gaussian curve substracted from the first one, in order to create the double-Gaussian profile that fits the vessel model.

The angle θ is computed from the orientation of the ROI provided by the user. The length parameter is set to 14 pixels in order to enhance the vessel in a small window centered at the initial ROI, which is large enough for the detection of the four new ROIs, parallel to the initial one, by the algorithm. The resulting vessel response is computed by applying the DG in this window, and extracting the maximum response of the filter for $\sigma_1 \in \{2, 2.5, 3, 3.5, 4, 4.5, 5\}$ pixels. We set $\sigma_2 = 0.3 \cdot \sigma_1$ and $h_1 > h_2$, as the central reflex curve peak is lower than the background peak, see Figure 3.5A and B. The response for a vessel with a slight curvature can be seen in Figure 3.7A. The advantage of applying this filter, which accounts for the central reflex, consists of its property to emphasize both vessel wall and lumen. The filter response is further used to guide the detection of four ROIs parallel to the initial one (two below and two above).

Detection of initial outer boundary points

Note that there is no single 'correct' vessel edge definition, and one is primarily interested in changes in diameter determined using the same method. This is true also for vessel edge definition in fundus photographs, as noted in [Bankhead et al., 2012]. Thus in our setting we define the points corresponding to the maximum response for the initial ROI set by the user on the vessel response image obtained after applying DG to represent the vessel outer boundary. This definition matches the one manually set by the user, see magenta points in Figure 3.5A, Figure 3.5B and Figure 3.5C.

Canny edge detection and removal of spurious pixels

To create a feature map of the vessels we first use a Canny edge detection filter on the smoothed image, which uses a hysteresis thresholding. After scaling the image gray values to lie between 0 and 1, we use upper and lower thresholds of 0.2 and 0.75, respectively, and discard regions containing fewer than five pixels above the upper threshold. Figure 3.7B shows an example of the Canny filter response.

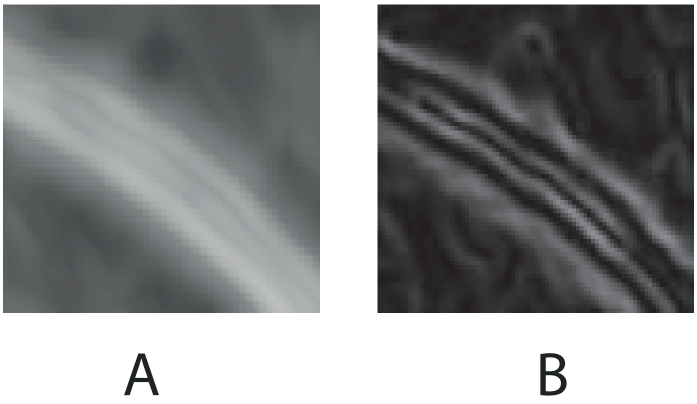

FIGURE 3.7: Part of a vessel with a slight curvature. A The dual-Gaussian response. B. The Canny edge response

Tracing outer boundary points

In the next step the outer boundary points are detected using a tracing approach, that combines information from the Canny edge response image and the DG response image. Denote by $\boldsymbol{p_i}(\boldsymbol{q_i})$ the point detected at a previous step to correspond to the outer boundary of the vessel on the left(right) side in the initial ROI, and by $\boldsymbol{\nabla p_i}(\boldsymbol{\nabla q_i})$ the direction of its corresponding gradient vector. The location of the next boundary point, $\boldsymbol{p_{i+1}}$, is estimated using the following extrapolation update equation

$$\boldsymbol{p_{i+1}} = \boldsymbol{p_i} + a \cdot \boldsymbol{\nabla p_i} \perp, \tag{3.3}$$

where $a = 2$ pixels is the step size and $\boldsymbol{\nabla p_i} \perp$ is a direction vector perpendicular to $\boldsymbol{\nabla p_i}$. This direction is along the vessel. The same equation is applied for the detection of the point $\boldsymbol{q_{i+1}}$. The final position for the points $\boldsymbol{p_{i+1}}$ and $\boldsymbol{q_{i+1}}$ is set by computing the maximum points on the line connecting $\boldsymbol{p_{i+1}}$ and $\boldsymbol{q_{i+1}}$ in the DG image. We have observed that in the case of low contrast between vessel boundary and lumen the DG response is too small causing $\left|x_{p_{i+1}} - x_{p_i}\right| < 5$ pixels. In this case the minimum point on the line connecting $mid_{p_{i+1},q_{i+1}}$ and x_{p_i} in the Canny response image is taken as the final position for $\boldsymbol{p_{i+1}}$. $mid_{p_{i+1},q_{i+1}}$ is the mid point of the line connecting the points $\boldsymbol{p_{i+1}}$ and $\boldsymbol{q_{i+1}}$. In a similar way the point $\boldsymbol{q_{i+1}}$ is updated if $\left|x_{q_{i+1}} - x_{q_i}\right| < 5$ pixels. This is especially the case when dealing with vessels classified as unknown.

Detection of inner boundary points

In order to detect the vessel inner diameter, a well established method is used on the smoothed image: Half-Height Full-Width - the standard half-height method, which uses thresholds set half-way between the maximum and minimum intensities to either side of an estimated center point, on the denoised original profile of the ROIs, see Figure 3.8. In the case of vessels where the inner diameter is not visible, see an example in Figure 3.5C, there is no maximum peak detected, and therefore, the method delivers only one value between the two outer boundary points. Thus the inner boundary is set to have 0 length.

The output of the algorithm is 15 measurements, illustrated in Figure 3.9A, containing the

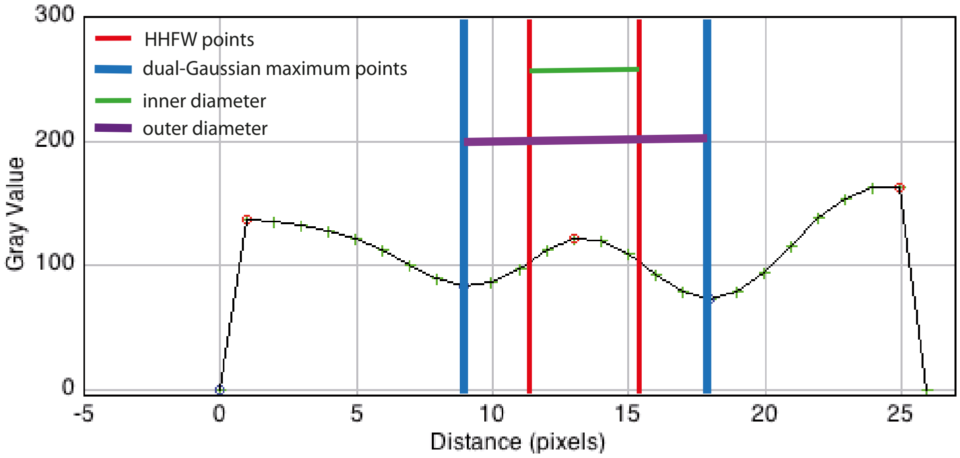

FIGURE 3.8: Vessel profile of one ROI detected by the algorithm with inner and outer boundary points, HHFW = Half-Height Full-Width. The gray values in the graph belong to the values from the smoothed image (the original image after applying the anisotropic diffusion filter).

inner and outer diameter for a blood vessel from 15 ROIs. The final measurement for a single blood vessel is computed as the average value of those 15 results.

3.2.2 Validation

There is no gold-standard data base of segmented vessels for cSLO images, as in the case of fundus photographs. Therefore the results provided by the algorithm were visually corrected by the user and wrongly detected boundaries were discarded from the final result (from 218.517 measurements, 6.492 were discarded; this corresponds to an error rate of 3%). Figure 3.9B illustrates an example of a vessel with a falsely detected inner boundary (at the 3rd. ROI from the left) and low contrast between the boundary and the background. In order to test the reliability of the method, 58 eyes with 735 vessels of HC were examined using the algorithm by two independent users. The ICC was 0.995 for the outer diameter, and 0.970 for the inner diameter differing slightly between the vessel types (arteries, veins or unknown), see Table 3.1.

The distribution of the measured vessels according to diameter size and type is illustrated in Figure 3.10. It can be observed that especially in case of small vessels the classification into artery or vein was nearly impossible, and thus these measurements were disregarded in the clinical study described in Subsection 3.2.3. Our algorithm was able to accurately detect only 66% of the inner diameter of the 218.517 marked vessels. Therefore the outer diameter was

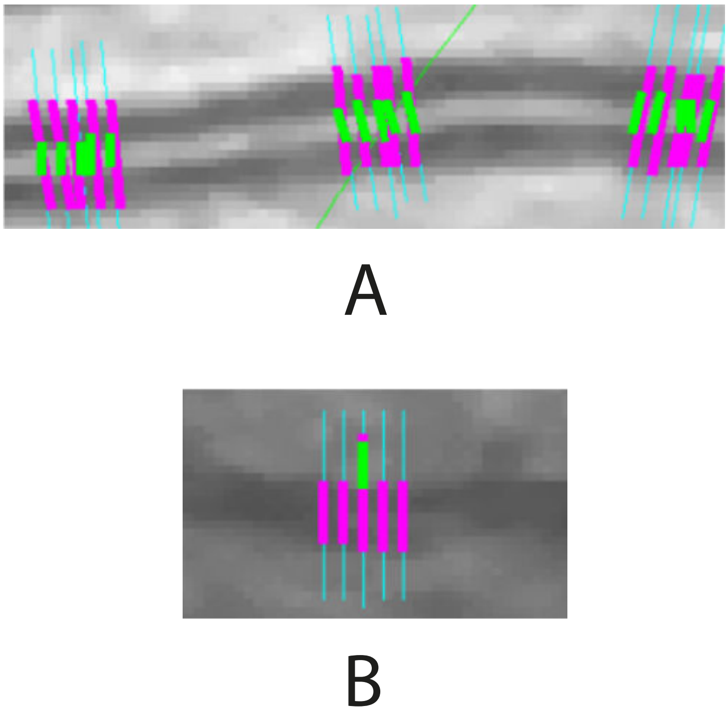

FIGURE 3.9: A. A close up with correctly (by our definition and a visual inspection from the user) delimited inner and outer diameter of a vessel. B. A close up of a small vessel with low contrast and a wrongly delimited inner boundary with its profile.

TABLE 3.1: Intraclass correlation coefficient of the vessel inner and outer diameter measurements between the two graders.

	Inner diameter		Outer diameter	
Vessel type	No.	ICC	No.	ICC
All	735	0.995	511	0.970
Arteria	303	0.935	274	0.946
Vein	205	0.996	188	0.980
Unknown	227	0.980	49	0.825

TABLE 3.2: Demographic overview of MS patients and HC. SD = standard deviation.

			Patients	HC
Subjects	No.		108	96
Eyes	No.		216	192
Gender	No.	male	35	29
		female	73	67
Age	Mean (±SD)		42 (±12)	39 (±12)
Disease type	No.	CIS	27	
		RRMS	64	
		SPMS	17	
ON	No. of eyes		74	
Disease duration (months)	Mean (±SD)	CIS	8 (±9)	
		MS	116 (±83)	
RNFL thickness (μm)	Mean (±SD)		87.7 (±14.5)	98.6 (±9.6)
TMV (mm^3)	Mean (±SD)		8.41 (±0.4)	8.63 (±0.34)

chosen as parameter for the statistical analysis as there is a strong correlation between inner and outer diameter [Bilger, 2014].

3.2.3 Results in a clinical study

Our algorithm was applied in a clinical study to investigate the differences in retinal blood vessels in patients with MS or CIS. 108 patients and 96 age- and sex-matched HC were included in the study, see Table 3.2. The age difference between HC and patients was not significant (T-test: $p = 0.19$). Between HC and MS patients there was no significant difference both in average arterial diameter (GEE: $p = 0.332$) and average venous diameter (GEE: $p = 0.908$) [Bilger, 2014]. Patients with a high disease duration and/or ON had a slightly reduced vessel diameter, especially in the average venous diameter, compared to the group of matched HC, although this difference was not significant [Bilger, 2014]. However, there was a significant correlation between the standard OCT parameters (RNFL thickness an TMV) and the blood vessel outer diameter both for arteries and for veins [Bilger, 2014].

Statistical analyses were performed with SPSS 19 (IBM SPSS Statistics Version 19, Release 19.0.0.1, IBM, Armonk, NY, USA).

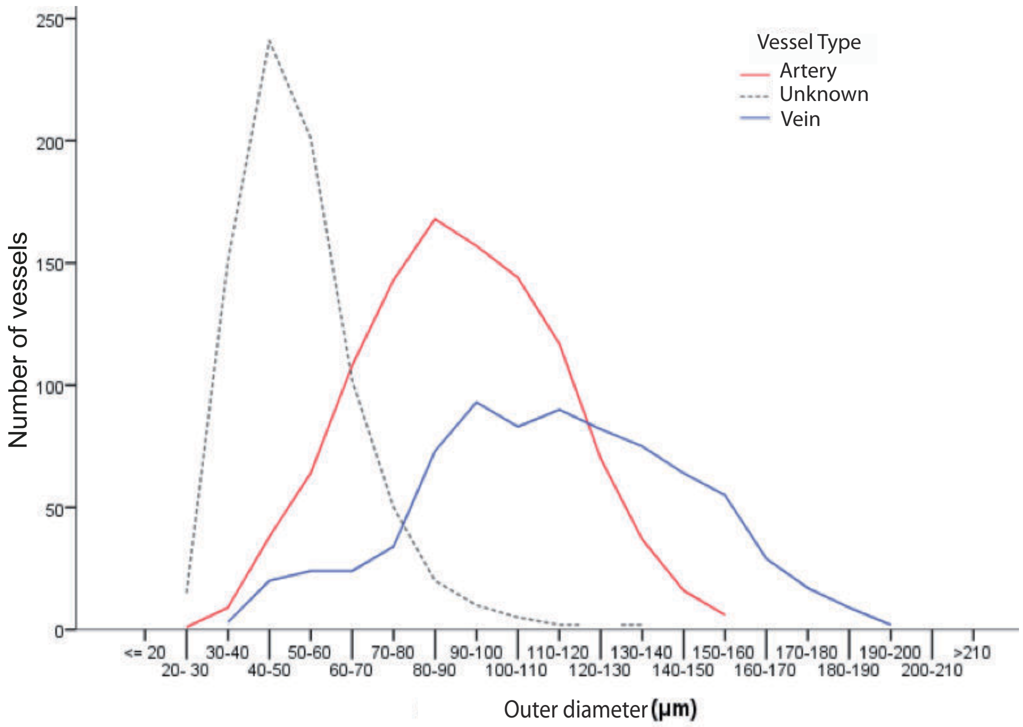

FIGURE 3.10: Distribution of the blood vessels (2654 vessels with: No. of arteries = 1078, No. of veins = 777 and No. of unknown = 799) corresponding to HC according to diameter size and blood vessel type.

Development environment

Algorithm development was done as an ImageJ plugin using Java SDK 1.6 (Oracle, Redwood Shores, CA, USA) and ImageJ version 1.46e (W. Rasband, http://imagej.nih.gov/ij) (Schneider, Rasband, and Eliceiri 2012) on Mac OS X (Apple, Cupertino, CA, USA, Intel Core i5, 4GB memory). Our approach requires 15 seconds for the automated part of the computation (after the user labeled the vessels).

3.3 Automated detection of the entire retinal vasculature in cSLO images

We developed an automated vessel detection tool for the segmentation of the entire retinal vasculature in ONH centered cSLO images. These images are acquired together with the 3D SDOCT ONH scan and have an image size of 768×768 pixels with a resolution of $11.4878\ \mu m/$ pixel. Our main motivation focuses on a technical aspect, as retinal blood vessels could be further used as landmarks for the registration of different ONH scans. An important characteristic of the

ONH region is that, unlike the brain cortical surface, the ONH surface presents no known folds or visible landmarks. Considering our special interest in characterizing even subtle changes in the ONH structure, that we hypothesize to be present especially in the acute ON phase (see Section 2.4), the identification of specific topographic features and local shape structures such as blood vessels is a key prerequisite to obtain anatomically meaningful registrations for further analysis in this direction. As described in Section 3.1, the cSLO image is typically a grey scale image with non-uniform illumination, low global/local contrast and high background noise [Xu et al., 2008]. Therefore we first address the issues mentioned, to prepare the images for further analysis as follows.

Nonuniform illumination correction

To correct variable non-uniform illumination, especially the vignetting observed in cSLO images illustrated in Figure 3.11A, we applied a computationally efficient approach presented in [Zheng et al., 2009]. The method uses the sparseness property of the gradient probability distribution to estimate the intensity nonuniformity in medical images. It is a fast and accurate method tailored specifically for the illumination artifacts seen in medical imaging like magnetic resonance imaging, computer tomography, X-ray, ultrasound. For our images we have chosen the non-parametric approach, with the bias field represented parametrically with the bipolynomial presented in [Zheng et al., 2009]. The parametric one produces larger errors when the nonuniformity is severer [Zheng et al., 2009], a drawback observed also in our experiments in images like the second and third image in Figure 3.11A.

Anisotropic coherence diffusion for enhancement of flow like structures

To adapt the diffusion tensor D introduced in Section 2.1.3 to the local structure of the image we derived methods to compute the main variables ρ from Equation 2.22 and C from Equation 2.27 as follows.

The eigenvalues of the tensor integrate the variation of the gray values within a neighbourhood of size $O(\rho)$. They describe the average contrast in the eigendirections. In order to get the integration scale ρ to reflect the characteristic size of the texture of the image, we introduce a

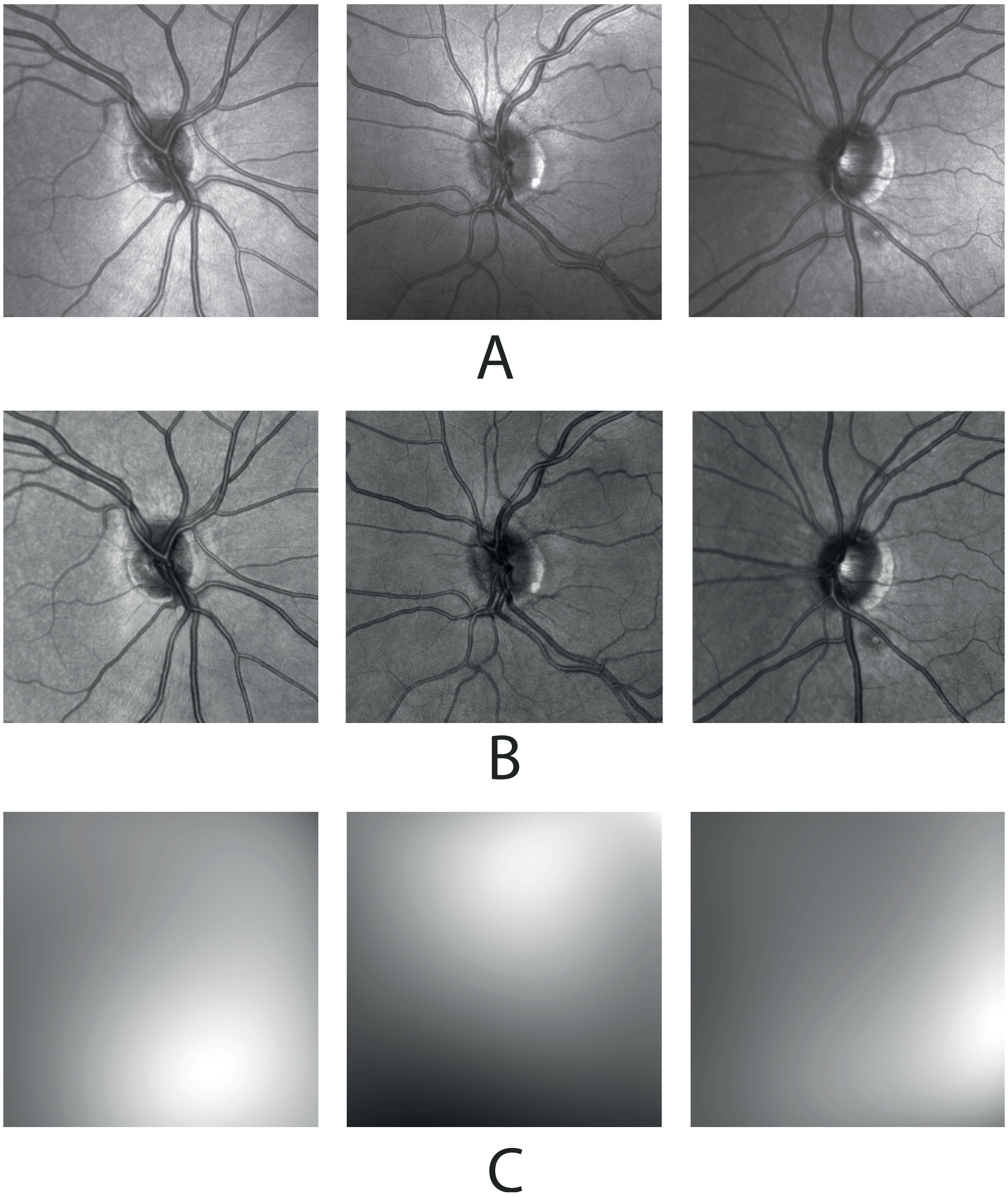

FIGURE 3.11: A. Original cSLO images with different degrees of non-uniform illumination. B. Non-uniform illumination corrected cSLO images. C. Bias field approximation of the non-uniform illumination.

simple *vesselness* property based on the eigenvalues of the structure tensor S_ρ

$$vesselnessMap(x) = \begin{cases} 0, \text{ if } \lambda_1 > 0 \\ \\ |\lambda_1| - |\lambda_2|, \text{ otherwise} \end{cases} . \tag{3.4}$$

The *vesselness* map containing the enhanced blood vessels is shown in Figure 3.12A. To detect the percentage of vessel structures from the image, we apply the thresholding method proposed by [Otsu, 1979]. The area containing the vessels in the binary image obtained is computed as a percentage of the whole image area. This is the value we set for ρ.

C is another important variable in the computation of the diffusion. It acts as a threshold parameter. Structures with coherence measures $(\lambda_1 - \lambda_2)^2 \ll C$ are regarded as almost isotropic, and the diffusion along the coherence direction (the smallest eigenvector) tends to α. For $(\lambda_1 - \lambda_2)^2 \gg C$, the diffusion along the coherence direction tends to its maximal value, which is limited by 1. To set this parameter we apply a similar approach as for ρ, but on the coherence $(\lambda_1 - \lambda_2)^2$ result image map. The coherence result is depicted in Figure 3.12B. Figure 3.12C illustrates the structure tensor S_ρ smallest eigenvector orientation in degrees of the original image. It depicts the coherence orientation. The eigenvalue corresponding to this direction of the diffusion tensor D of the original image is illustrated in Figure 3.12D. The result of the original image seen in Figure 3.13A is shown in Figure 3.13B. It can be observed that it shows less smoothing across the vessel boundaries compared to the well-known anisotropic diffusion by [Perona and Malik, 1990], see Figure3.13C.

We implemented three approaches in order to test their ability to detect the retinal vessel map. Our main goal was to detect a connected vessel network with clear defined crossings in order to further use these crossing as possible landmarks for registration purposes.

3.3.1 Approach 1. Extended 2D Morlet filtering with principal curvature enhancement

The steps of the proposed method can be seen in Figure 3.14

In order to detect oriented features (segments, edges) in an image like the blood vessels in our case, we applied a wavelet which is sensitive to directions. An example of such a wavelet is

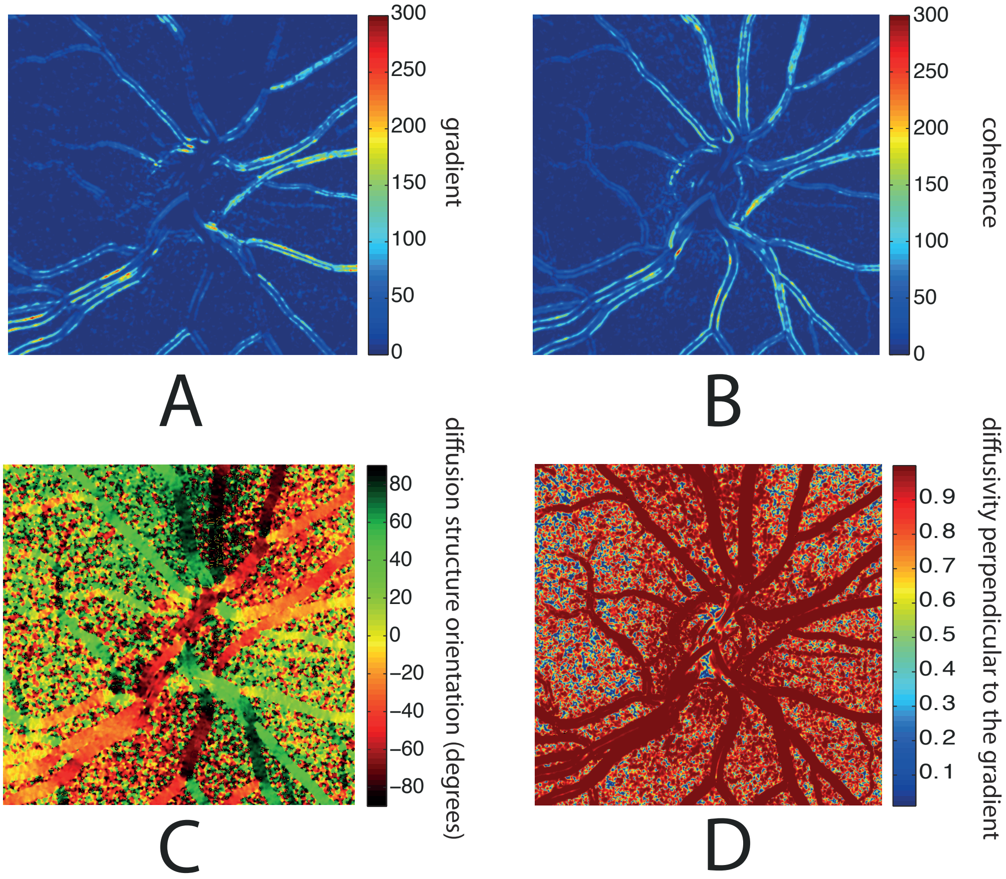

FIGURE 3.12: A. The gradient orientation map of the original image. B. The coherence $(\lambda_1 - \lambda_2)^2$ of the original image. C. Diffusion structure orientation in degrees. D. The diffusivity perpendicular to the gradient. E.

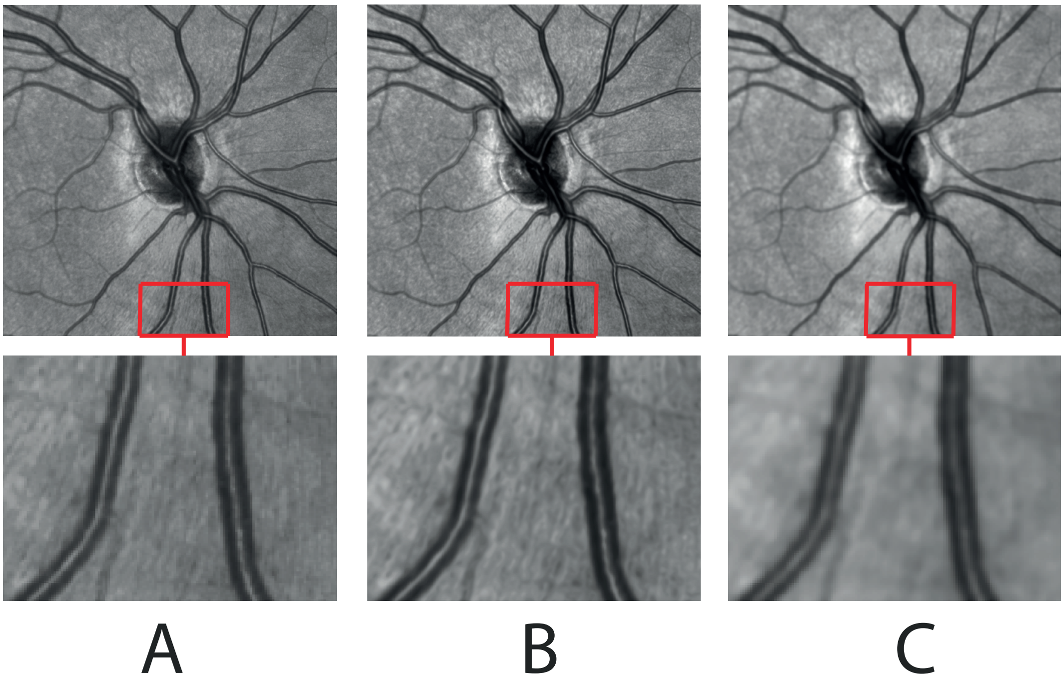

FIGURE 3.13: A. The original image, with a zoomed in area corresponding to the red rectangle. B. The result after applying the coherence diffusion enhancement with the parameters : $\rho = 0.5$, $C = 0.7$, step size = 0.25 after 20 iteration steps, with a zoomed in area corresponding to the red rectangle. C. The result after applying the anisotropic diffusion defined by [Perona and Malik, 1990] with parameters $k = 30$, step size = 1/7, after 20 iterations, with a zoomed in area corresponding to the red rectangle.

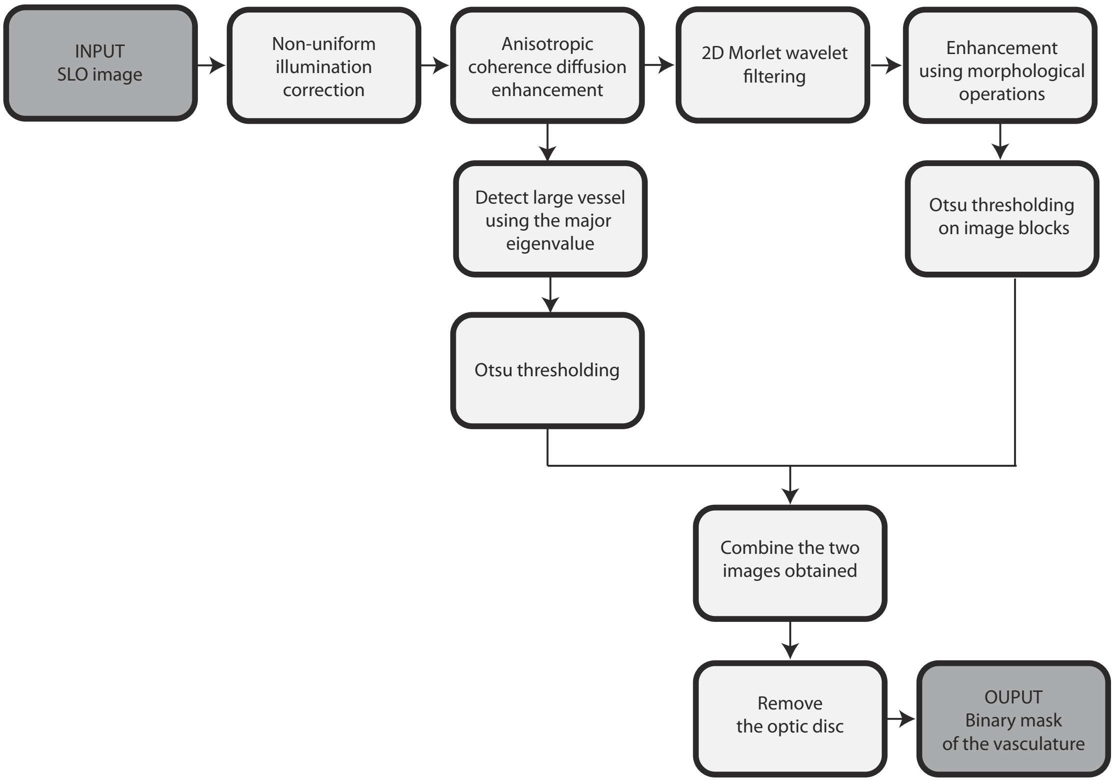

FIGURE 3.14: The steps of the algorithm in Approach 1.

the 2D Morlet wavelet (MW) as proposed by [Antoine et al., 1993] is defined as

$$\psi_M(\boldsymbol{x}) = e^{i\boldsymbol{k_0}\cdot\boldsymbol{x}} e^{-\frac{1}{2}|A\boldsymbol{x}|^2}, \tag{3.5}$$

where $\boldsymbol{k_0}$ is the wave vector defining the frequency of the complex exponential, $A = diag\left[\epsilon^{-\frac{1}{2}}, 1\right]$, $\epsilon \geq 1$, is a 2×2 diagonal matrix that defines the anisotropy of the filter (its elongation in any desired direction). Examples for the real part of the 2D MW from Equation 3.5 for different settings of the variables ϵ, $\boldsymbol{k_0}$, with a different scale (dilation) parameter at different orientation can be seen in Figure 3.15. As described in [Soares et al., 2006], 2D MW has the capability of directional selectiveness and detection of oriented features. It provides a decomposition of an image into details having different resolutions and orientations.

The MW is a complex exponential modulated Gaussian. We use the notation employed by [Soares et al., 2006], where the $f \in L^2$ is an image represented as a square integrable function

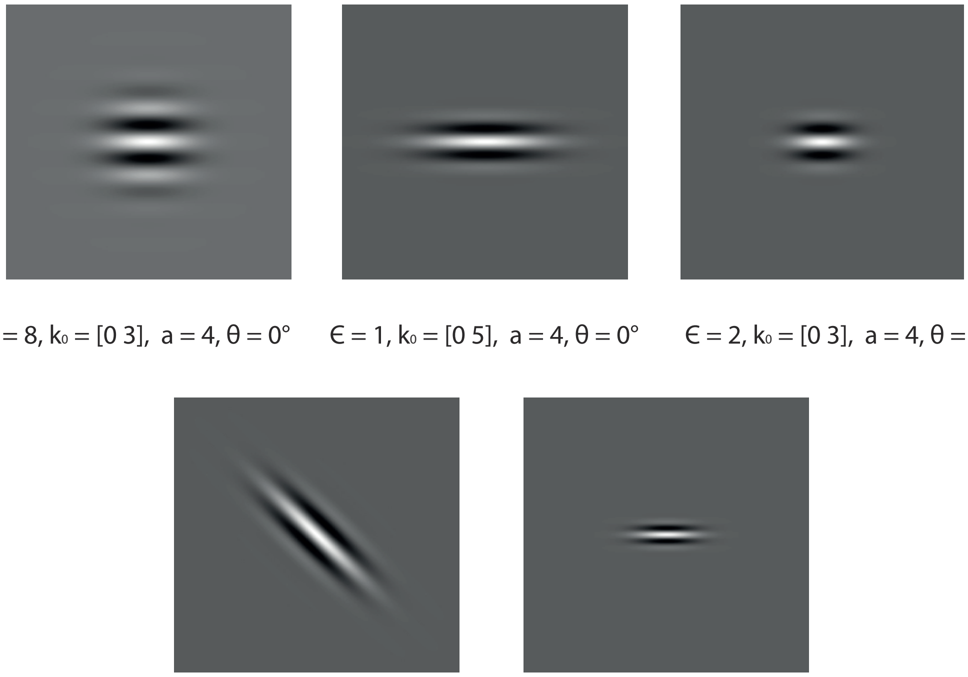

$\epsilon = 8$, $k_0 = [0\ 3]$, $a = 4$, $\theta = 0°$ $\epsilon = 1$, $k_0 = [0\ 5]$, $a = 4$, $\theta = 0°$ $\epsilon = 2$, $k_0 = [0\ 3]$, $a = 4$, $\theta = 0°$

$\epsilon = 8$, $k_0 = [0\ 3]$, $a = 4$, $\theta = 45°$ $\epsilon = 8$, $k_0 = [0\ 3]$, $a = 2$, $\theta = 0°$

FIGURE 3.15: Real part of the MW, with varying parameters. ϵ parameter of the diagonal matrix A that defines the anisotropy of the filter, k_0 vector that defines the frequency of the complex exponential, a scale (dilation), θ is the rotation angle, see Equation 3.5 and Equation 3.6.

defined over $\mathbb{R}^2$. Then the continuous wavelet transform is defined as:

$$T_{\psi}(\boldsymbol{b},\theta,a)(\boldsymbol{x}) = \frac{1}{a}\int \psi^{*}[a^{-1}r_{-\theta}(\boldsymbol{x}-\boldsymbol{b})]f(\boldsymbol{x})d^{2}\boldsymbol{x}, \tag{3.6}$$

where ψ, ψ^*, $\boldsymbol{b}$, θ and a denote the analyzing wavelet, its complex conjugate, the displacement vector, the rotation angle and the dilation parameter. In our approach, in Equation 3.5, we have set the parameter ϵ to 4, making the filter elongated and $\boldsymbol{k_0} = [0, 3]$, i.e., a low-frequency complex exponential with few significant oscillations perpendicular to the large axis of the wavelet, and a to 2. This characteristic is especially suited for the detection of directional features and has been chosen in order to enable the MW transform to present stronger responses for pixels associated with the blood vessels. The choice of the parameters is similar to [Leandro et al., 2001]. In their work [Leandro et al., 2001] performed extensive experiments with the MW for different sets of parameters, where they have shown that many sets of parameters lead to similar (good) results, suggesting that this is not so critical. For each pixel position and considered scale value, we are interested in the response with maximum modulus over all possible orientations. Thus, the MW transform is computed for θ spanning from 0° up to 180° at steps of 10°. The algorithm used in our approach is presented Algorithm 1.

```
Data: I
Result: $T_{max}(\boldsymbol{b},\theta,a)(\boldsymbol{x})$
Initialization: $T_{max}(\boldsymbol{b},\theta,a)(\boldsymbol{x}) = 0$, $a = 2$, $\boldsymbol{k} = [0,3]$, $\epsilon = 4$ ;
for each $\theta \in \{0°, 10°, ..., 180°\}$ do
    compute $I_F = FT(I)$ ;
    compute $\psi^*_M$;
    compute $\psi^*_{MF} = FT(\psi^*_M)$;
    compute $I_W = I_F \cdot \psi^*_{MF}$;
    compute $T(\boldsymbol{b},\theta,a)(\boldsymbol{x}) = IFT(I_W)$;
    $T_{max}(\boldsymbol{b},\theta,a)(\boldsymbol{x}) = max(T_{max}(\boldsymbol{b},\theta,a)(\boldsymbol{x}), |T(\boldsymbol{b},\theta,a)(\boldsymbol{x})|)$;
end
```

Algorithm 1: Algorithm for 2D MW transformation of the image I; FT represents the Fourier transform, IFT represents the inverse Fourier transform

Figure 3.16A shows a section of a cSLO enhanced by the coherence diffusion filter. The result of applying the 2D MW transformation to this section is shown in Figure 3.16B.

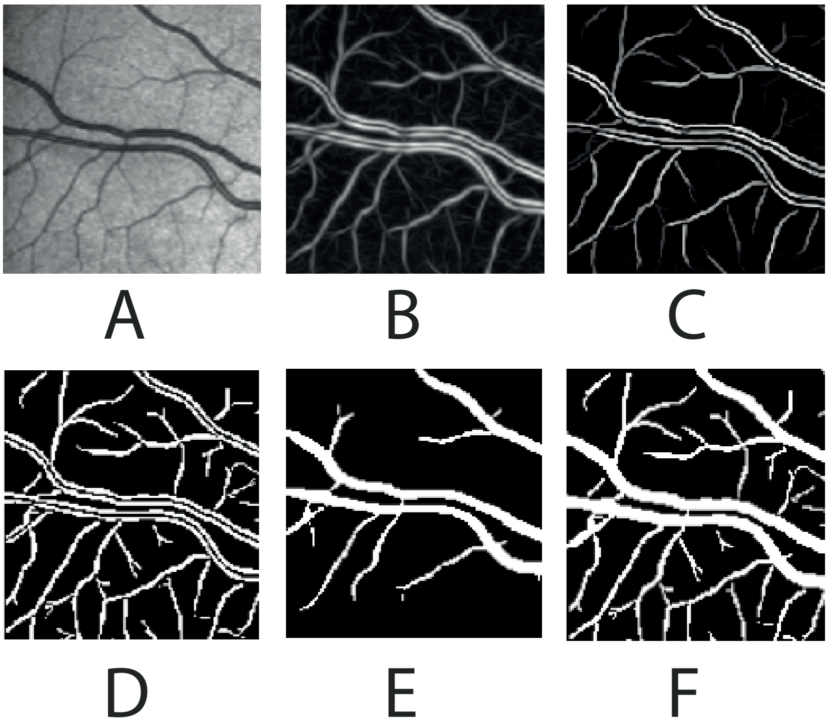

FIGURE 3.16: A. Part of an original cSLO image. B. The resulting image after applying the 2D MW. C. The resulting image after performing morphological opening and morphological reconstruction using the opening as a mask. D. The resulting image after applying Ostu's threshold method. E. The resulting image after enhancing the large vessels and Otsu's threshold. F. The final resulting image.

In order to further enhance the vessels from the background we make use of morphological operations. First we perform a morphological opening with a line structuring element of length $L = 17$ pixels rotated over 12 angles from $0°$ up to $180°$. By taking the maximum response of the openings performed and reconstructing the image using the opening as a mask, we enhance the vessels. To suppress the background we take the minimum response of the openings performed and reconstruct the image using the same opening as a mask, see Figure 3.16C.

We first split the image into 9 blocks in order to treat separately regions close to the ONH with large vessels that give a strong response after the MW filtering step, and regions at the periphery of the ONH, which contain rather small vessel with lower contrast to the background, and apply the Otsu's threshold method [Otsu, 1979] on each of these blocks, see Figure 3.16D.

To detect large vessels (large in this sense means the vessel with a diameter larger than 14 pixels) and their inner and outer boundary we compute the major eigenvalue, λ_2, corresponding to the maximum principal curvature of the Hessian matrix see Section 2.1.4 over 5 scales from 3 to 7 pixels on the coherence diffusion enhanced image. Since our best approximation of vessel radius at this stage of the algorithm is the scale factor, we used this in the computation of λ_2. Thus, vessels with diameter $d \approx 2\sigma$ are most strongly detected when the scale factor is σ. We normalize each feature along scales by d and then keep the local maximum over scales. We employ again Otsu's threshold method to detect the final response, see Figure 3.16E. Thus the final vessel map is comprised by the MW response and the maximum principal curvature response, see Figure 3.16F.

3.3.2 Approach 2. Improved *vesselness* response at vessel crossings

In this subsection we present another approach to segment the entire vasculature of the cSLO image, by deriving a new *vesselness* response filter. Figure 3.17 shows the main steps of this approach. Unfortunately, the Hessian-based *vesselness* [Frangi et al., 1998] and second order informations derived from the Hessian are only applicable to a limited extent as the measures are erroneous especially around bifurcations and crossing vessels. These errors arise due to the fact that the assumptions for the detection of the tubular structure, see Subsection 2.1.4, no longer hold. For an example see Figure 3.18A, which illustrates a part of a cSLO image with vessel crossings and Figure 3.18C showing the response of applying the *vesselness* method as proposed by [Frangi et al., 1998]. At the bifurcation of a small vessel from a large one the intensity

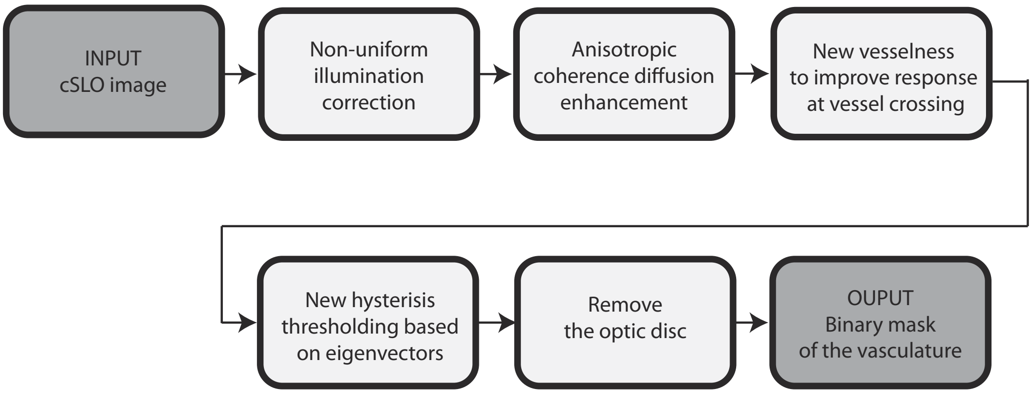

FIGURE 3.17: The steps of the algorithm of Approach 2.

profile along the small vessel direction is no longer homogeneous but drops significantly at the boundary of the larger vessel. In terms of second order structure, the intensity profile along the small vessel direction results in a significant negative second order derivative, i.e., $\lambda_1 \ll 0$ see Figure 3.19A. On the other hand, the estimated curvature perpendicular to the small vessel is influenced by the surrounding main vessel, which affects the magnitude of $\lambda_2 > 0$ see Figure 3.20A. Both effects mislead the *vesselness* filter in the immediate vicinity of the large branch, which results in a trench along the main branch see Figure 3.18C.

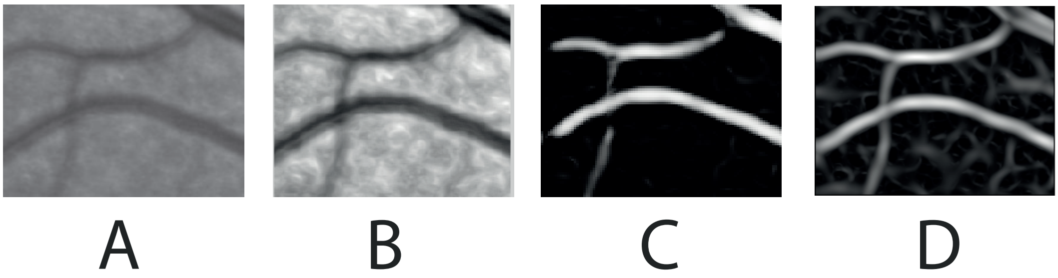

FIGURE 3.18: A. Part of an original cSLO image with vessel crossings. B. The response of the coherence diffusion. C. The response of Frangi's *vesselness*, see how vessels are disconnected at crossings. D. The proposed *vesselness* response showing better results at vessel crossings.

To overcome this problem we propose a different approach based on the fact that the eigenvector $\boldsymbol{v_1}$ corresponding to the smallest eigenvalue λ_1 is aligned to the vessel direction inside a vessel. Thus $|\lambda_2 \langle \boldsymbol{v}, \boldsymbol{v_1} \rangle|$, will be maximized at a vessel point x, when $\boldsymbol{v_1}$ is aligned to the vessel direction $\boldsymbol{v}$. We choose, $\boldsymbol{v} = [cos\theta, sin\theta]$, θ spanning from 0° up to 180° at steps of 10°.

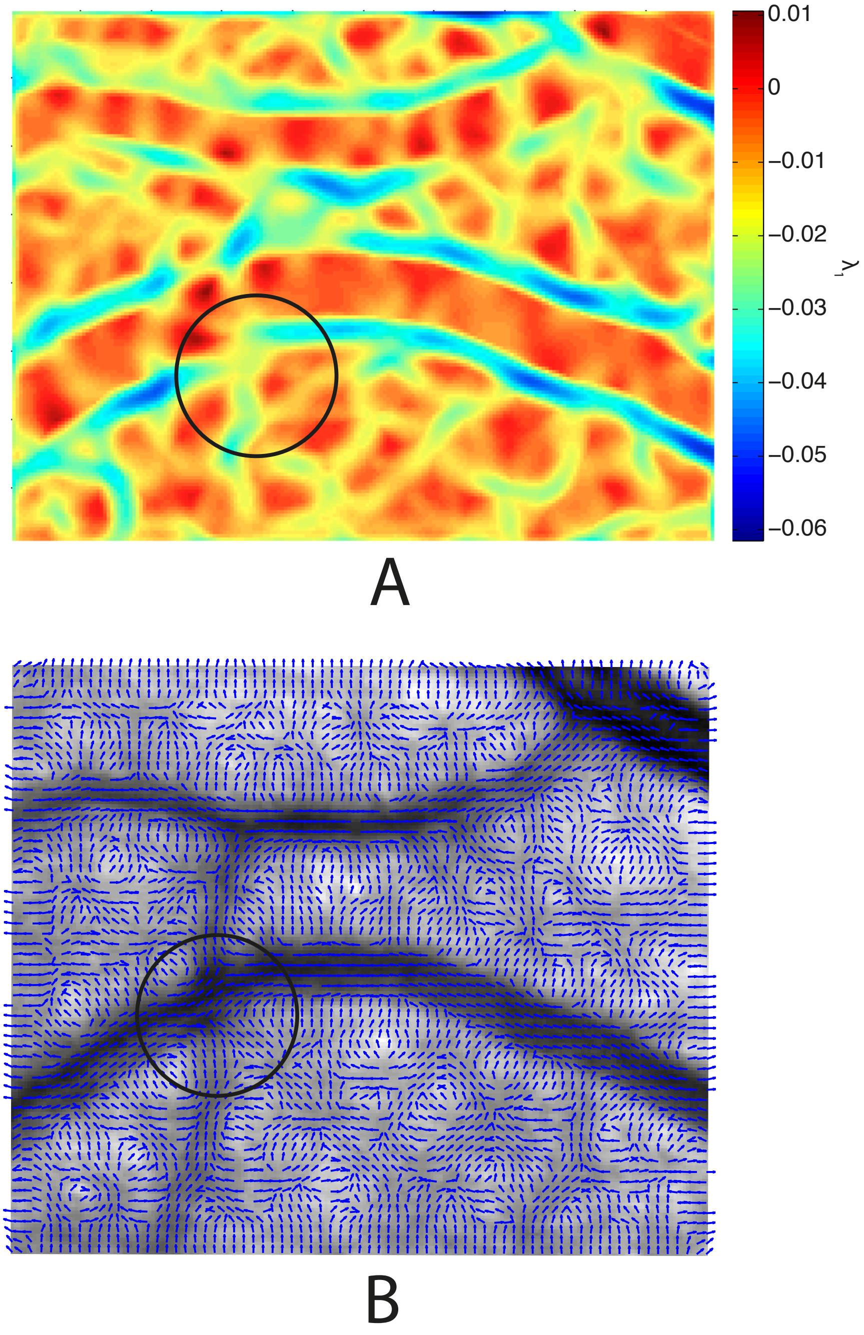

FIGURE 3.19: A. λ_1. B Its corresponding eigenvectors. Both eigenvalues and eigenvectors are shown for the scale $\sigma = 3$. Black circles indicate a position of vessels crossing.

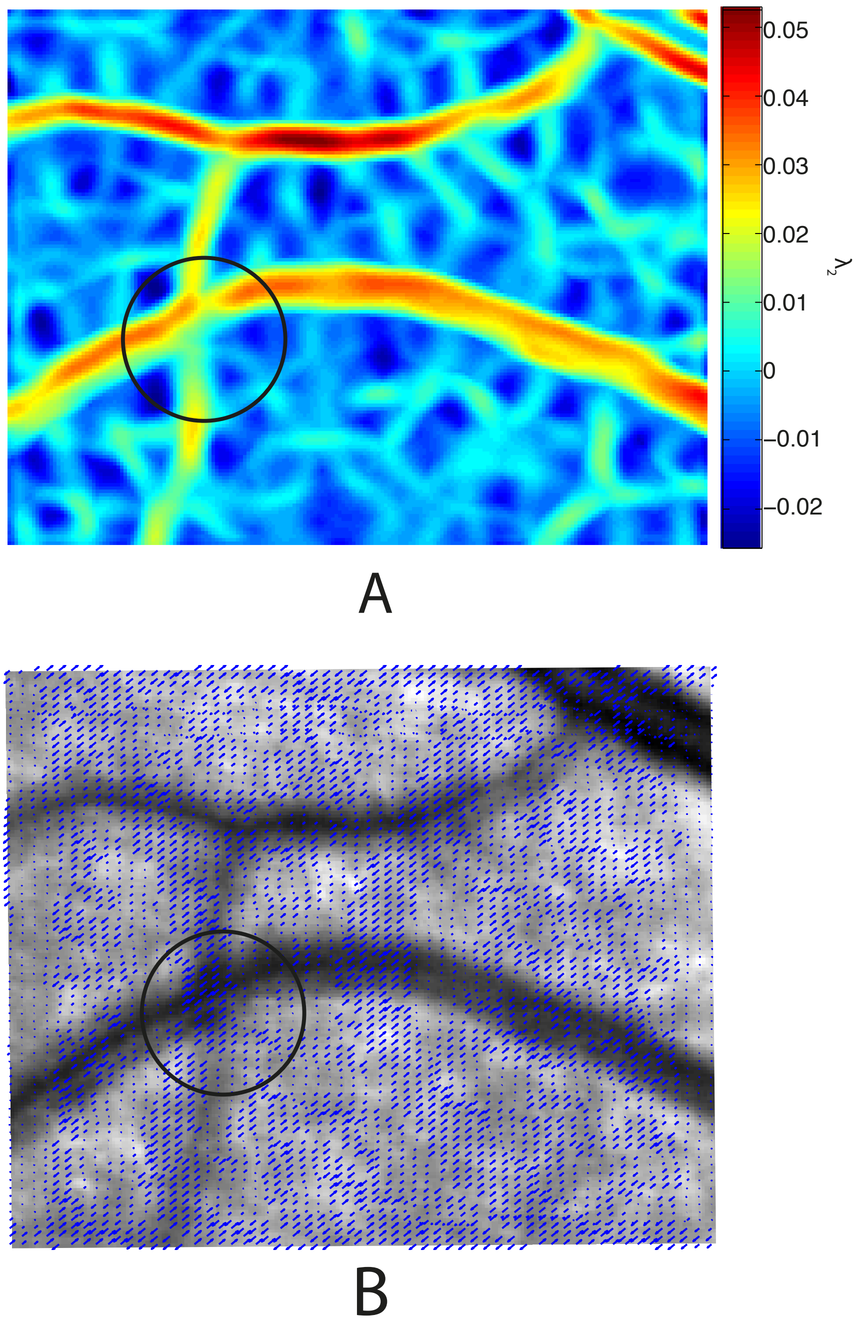

FIGURE 3.20: A. λ_2. B. Its corresponding eigenvectors. Both eigenvalue and eigenvector are shown for the scale $\sigma = 3$. Black circles indicate a position of vessels crossing.

As in [Frangi et al., 1998] our *vesselness* is obtained by computing this introduced measure as a maximum response over a range of 12 scales, varying from 1.5 to 7 with a step size of 0.5.

New hysteresis thresholding

The final response is computed using a new derived hysteresis thresholding. The high threshold (set at 0.05) indicates a strong principal curvature response. Pixels with a strong response act as seeds that expand to include connected pixels that are above the low threshold. Unlike the hysteresis threshold method [Yu et al., 2014], in our approach, the lower threshold is a function depending on each pixel's eigenvector and the surrounding ones. Each pixel's low threshold is set by comparing the direction of the major (or minor) eigenvector to the direction of the 8 adjacent pixel's major (or minor) eigenvectors. This can be done by taking the absolute value of the inner product of a pixel's normalized eigenvector with that of each neighbor. If the average dot product over all neighbors is high enough then we set the low threshold to be 1/5 of the high threshold, 1/2 otherwise. The final result can be seen in Figure 3.18D.

3.3.3 Approach 3. New *vesselness* response based on OOF

In this approach we make use of the eigenvalues and eigenvectors of the OOF filter. The main steps of the proposed method can be seen in Figure 3.21. λ_1 and λ_2 are the eigenvalues of the OOF see Figure 3.22B and Figure 3.22C. $\lambda_1 \leq \lambda_2$ and two corresponding eigenvectors are denoted by $\boldsymbol{v_1}$ and $\boldsymbol{v_2}$. $\boldsymbol{v_1}$ is perpendicular to the vessel direction and $\boldsymbol{v_2}$ is parallel to it at a position on the vessel's centerline and the scale r is equal to the vessel's radius.

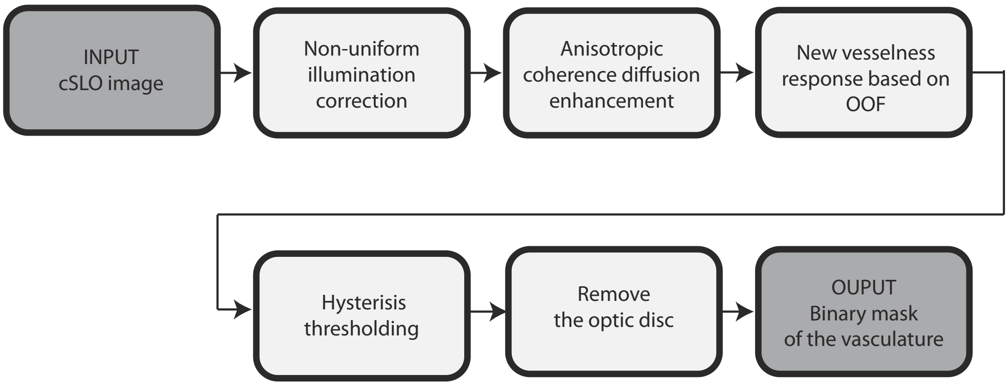

FIGURE 3.21: The steps of the algorithm of Approach 3.

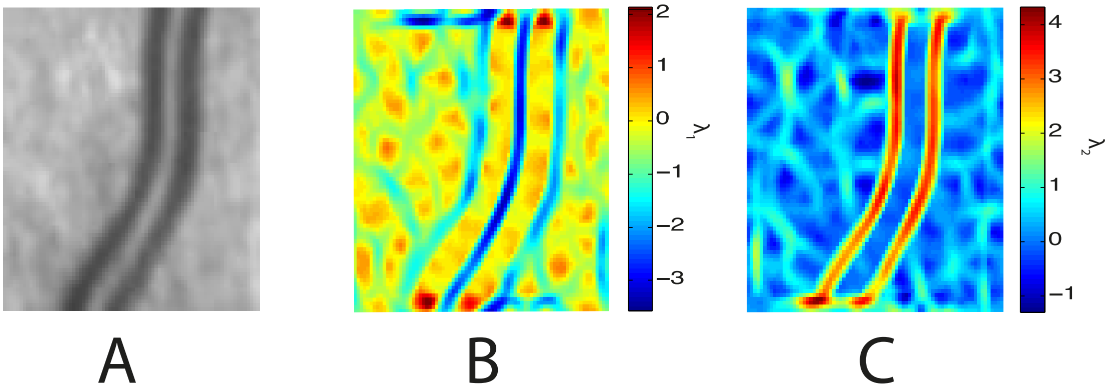

FIGURE 3.22: A. Part of a vessel from the original cSLO image. B. λ_1 of the OOF. C. λ_2 of the OOF. Both eigenvalues are shown for the scale $\sigma = 4$

The image gradient $\boldsymbol{\nabla I}$ at the object boundary of a strong intensity curvilinear structure points to the centerline of the structure. Inside the structure, when the local circular region boundary ∂D_r, see Equation 2.36, touches the object boundary, at the contacting position of these two boundaries, the image gradient is aligned in the opposite direction of the outward normal. Along the vessel direction, $\boldsymbol{v_2}$, the magnitude of the eigenvalue λ_2 is small inside the vessel as image gradient magnitudes are minor along the vessel direction. Along the first eigenvector $\boldsymbol{v_1}$, the magnitudes of λ_1 varies according to the radius of the local disc and also the positions where OOF is evaluated. Thus to obtain a high response inside the vessel but also on the boundary we define a new OOF *vesselness* measure as

$$\text{vess} = \left| \arg\min_r (\lambda_1(\boldsymbol{x}, r) \langle \boldsymbol{\nabla I}, \boldsymbol{v_1} \rangle) \right| + \arg\max_r (\lambda_2(\boldsymbol{x}, r) \langle \boldsymbol{\nabla I}, \boldsymbol{v_2} \rangle). \tag{3.7}$$

The final response is taken by hysteresis threshold with lower threshold 0.25 and upper 0.6 on the *vesselness* response. This was found to provide satisfactory results, and removing spurious response at non-vessel regions.

Remove the optic disc

We apply this step to all our approaches to remove the region on the ONH. At this low intensity region, all vessels gather, strongly influencing the detection of single vessels. We emphasize that our main goal is to create a vessel map for registration purposes, therefore we just roughly estimate and remove the ONH region from our final resulting images. This is performed using some simple operations: first a strong Gaussian smoothing is applied with $\sigma = 7$ in the original image, the intensity is normalized to lie between $[0, 1]$, and a simple binary threshold 0.3, found in our experiments to provide a satisfactory result in segmenting the ONH region, is applied. The binary mask is then dilated using morphological operation, with a disc element of 10 pixels and an ellipse is fitted to the obtained mask.

3.3.4 Experimental results

In the absence of a ground truth database we are not able to directly compare the three approaches. Therefore we show two particular examples, with a "normal" vessel network from a HC and one with strong curvature from a patient with IIH, to provide a better insight in the performance of the detection of the vessels (inner and outer boundary) see Figure 3.23. A detailed comparison between the results is presented in Section 6.2. From the computational time point of view, the OOF *vesselness* was the fastest with 2.1 to 3 seconds, followed by the modified Frangi *vesselness* measure, 4.3 to 5.8 seconds, and the MW enhancement technique 5.6 to 6.9 seconds.

Development environment

Algorithm development was done using Matlab R2011A with Spline library (Mathworks, Germany) on Mac OS X (Apple, Cupertino, CA, USA, Intel Core i5, 4GB memory).

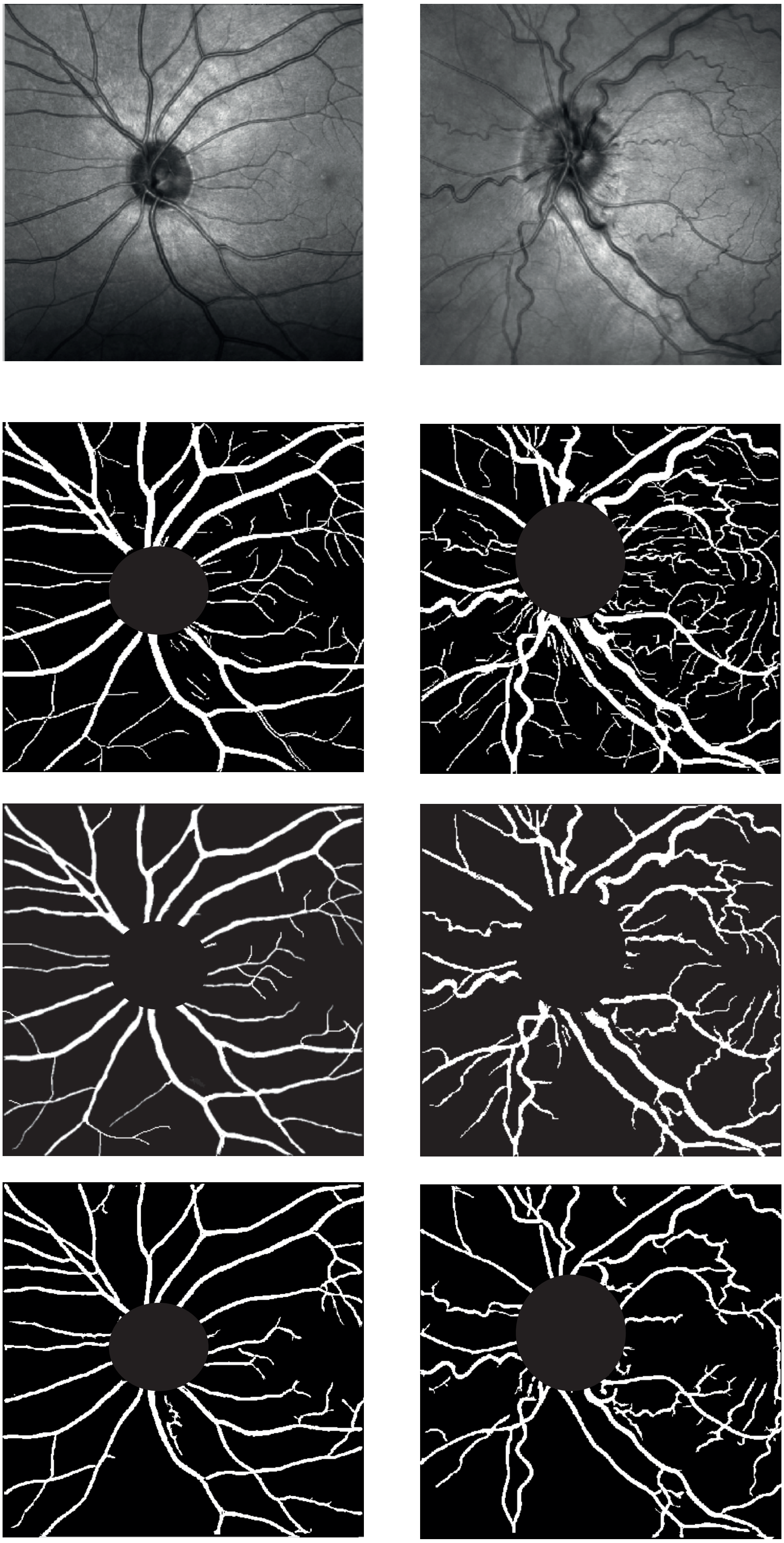

FIGURE 3.23: From top to bottom: first row original images, second row the result with Morlet filtering, third row the result with the modified Frangi's method, last row the result from the modified OOF.

Chapter 4

RPE lower boundary segmentation for ONH volume computation

This chapter presents a reliable approach for the detection of the RPE boundary from 3D SDOCT ONH scan. The RPE lower boundary is used as a reference surface for the computation of the ONH volume. The presented method is able to extract the RPE from data of HC as well as from data with swelled ONH. As described in Section 2.4 there are several cases like ON, or IIH which causes a swelling of the ONH. In order to quantify the edema, the computation of its volume is needed. However, current algorithms presented in Subsection 4.1 fail to satisfactorily segment the ONH in cases of swelling, as segmentation is especially challenging in diseases that show profound ONH alterations.

In cases of extreme swelling like in IIH, OCT scans tend to have regions of strong varying intensity values caused by the edema. Additionally, scans are characterized by an increased intrinsic speckle noise making a reliable differentiation of intraretinal layers challenging to impossible. To exemplify cases of severe swelling we illustrate two ONH scans from IIH patients. These can appear as a "hill", see Figure 4.1A, or as a "volcano", see Figure 4.1B, with varying sizes. In this region the retinal layers or other structures, like the BMO, are hardly recognizable.

4.1 Previous approaches in RPE lower boundary segmentation

There has been an extensive work in developing robust algorithms for intraretinal layers segmentation in SDOCT images, from early approaches [Ishikawa et al., 2005, Rossant et al., 2009b],

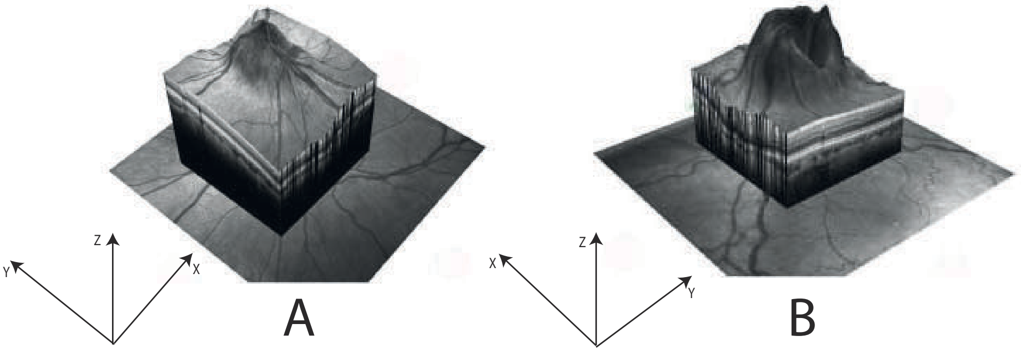

FIGURE 4.1: 3D SDOCT volume of two different swelled regions. One A. that has a hill form, and B. with a "volcano" shape, [Kadas et al., 2012a].

relying mainly on 2D information heavily based on edge profiles and largely validated on normative datasets rather than on data of patients, to 3D based approaches like graph-cuts that incorporate 3D contextual information [Bhavna et al., 2014, Garvin et al., 2008, Lee et al., 2010]. While [Garvin et al., 2008, Lee et al., 2012] proposed 3D graph-cuts in volumes centered at the macula from HC, [Bhavna et al., 2014] further developed this technique by incorporating textural information, for macula and ONH centered volume scans, from HC and from patients with glaucoma. There are several aspects regarding these approaches when considering the segmentation of the RPE. First the common denominator of all of these methods is that these rely on the observation that the RPE is one of the most hyper-reflective layer among all intraretinal layers, thus providing a good contrast for segmentation. Also in the macula scans this layer is not interrupted as in the ONH centered ones, making the segmentation less prone to errors. The method proposed by [Bhavna et al., 2014] adapted the graph-cuts technique also on ONH centered scans, but this method was tailored for HC and glaucoma volume data sets. Although in the case of glaucoma the ONH undergoes a degeneration process, the RPE presents negligible changes [Strouthidis et al., 2009b].

In contrast, in the swelled ONH region, the retinal layers or other structures, like the BMO, are hardly recognizable. Also, the assumption of hyper-reflectivity of the RPE no longer holds. Another approach [Hu et al., 2010b] that assessed the detection of the ONH structural change in 3D OCT scans, use the BMO as a basis for a longitudinally stable reference plane. In IIH patients this structure can be partly or entirely affected by the swelling, therefore hardly visible. Also as presented by [Scott et al., 2010] the commercial machines were not specifically designed for papilledema, so the commercial algorithm frequently failed with severe papilledema. Our main assumption was that the papilledema is enclosed by the inner limiting membrane (ILM) and RPE lower boundary.

Contributions

The work presented in this chapter presents several advantages over other RPE boundary segmentation techniques:

- the algorithm is able to detect RPE from 3D SDOCT images in the area of the optic disc which exhibits regions with strong intensity inhomogeneities, low or no intraretinal layer contrast, therefore contradicting the hypothesis that the RPE is one of the most hyper-reflective layers within a retinal SDOCT image
- it determines the position of the RPE also from eyes with a strong natural curvature
- it is robust against missing layer information and strong variations caused by ONH edema, by using reliable information only from a sub region of the ONH scan
- it can be further used to quantify ONH swelling (volume and maximal height) in patients with unclear symptoms, or ONH regions with unusual retinal structure and poor signal quality

The algorithm was published in [Kadas et al., 2012a].

Furthermore our algorithm was applied in two important clinical studies. In [Kaufhold et al., 2012] we were able to show that although peripapillary RNFL thickness did not show differences between HC and IIH patients, the newly developed 3D parameters: ONH volume (ONHVV) and ONH maximum height (ONHH) were able to discriminate between HC, treated and untreated patients. Both ONHV and ONHH measures were related to levels of ICP, see details in Subsection 4.4. In the second clinical study [Albrecht et al., 2015] investigated whether patients with moyamoya angiopathy without obvious retinal pathologies may have subtle subclinical retinal changes. The main finding in the investigation was a pronounced reduction of the ONHV (computed with our algorithm) in moyamoya angiopathy compared with HC, see details in subsection 4.4. The results were published in *Neurology*, one of the most important neurology journals.

4.2 Algorithm description

In the following section we present a detailed description of the proposed algorithm. Spatial ONH scans were performed using a custom protocol for high-resolution optic nerve head imaging with 145 B-scans focusing on the optic nerve head with a scanning angle of $15^\circ \times 15^\circ$ and a resolution of 384 A-scans per B-scan. While the ILM is provided by the OCT device's software, the RPE is detected with the presented algorithm. The RPE is our key ingredient. It separates the other layers from the choroid see Figure 2.15. In the presented algorithm, we detect the RPE around the ONH and extend it through the ONH as a theoretical lower bound to volume and height measurements. An overview of the algorithm is provided is Figure 4.2

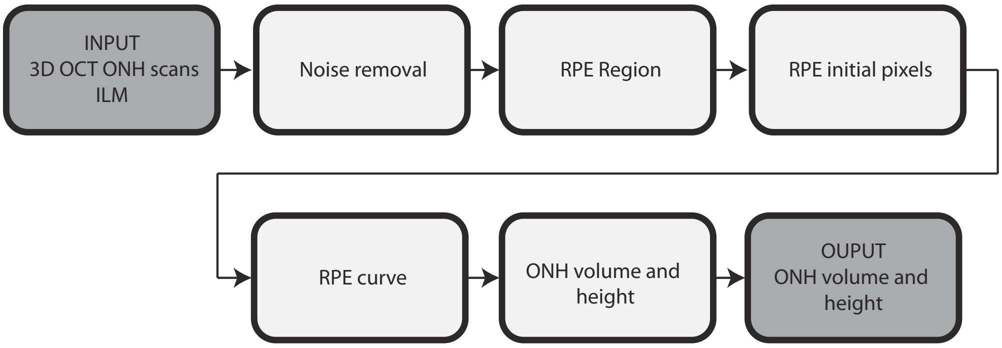

FIGURE 4.2: Steps of the RPE lower boundary detection algorithm.

Noise removal

Given a B-scan from the 3D OCT scans, the intrinsic speckle noise is reduced by denoising each B-scan using anisotropic diffusion as described in [Perona and Malik, 1990], with a number of iterations set to 10. Then a relatively homogeneous region from the corresponding ILM to the INL is created by dilating the ILM with a disc structure of radius 4 pixels. After that, each B-scan is smoothed with a large Gaussian filter, size $[7, 7]$, with $\sigma = 5$. The resulting image contains three regions in the following order from top to bottom: light gray, black and gray, see Figure 4.3A and B.

4.2.1 RPE Region

The regions we assumed to contain the RPE are the two lower ones. Two curves are detected to bound the search area for the RPE from these regions. The candidate pixels for the construction of the curves are found per column

- for the upper one from top to bottom, starting at the ILM

$$\underset{ILM(i)<j<n}{\arg\min} \; \{I(p(y_i, z_j)) < 60 \text{ for } 1 < i < m\}$$

- for the lower one from bottom to top

$$\underset{ILM(i)<j<n}{\arg\max} \; \{I(p(y_i, z_j)) > 20 \text{ for } 1 < i < m\}\,,$$

where $m \times n$ is the total number of pixels in each B-scan, and $I(p)$ the intensity value at a point p. The two intensity threshold values were found by experiments with our data set such that RPE regions with low intensity values are also taken into account. Fitting a cubic spline to the set of top and lower resulting pixels two boundary curves C_1 and C_2 shown in Figure 4.3A and Figure 4.3B, respectively.

4.2.2 RPE Initial Pixels

Having the two curves C_1 and C_2 from the previous step, RPE pixels candidates within the bounded region are now chosen. Previous reports [Chiu et al., 2010] defined RPE consisting of pixels having the highest intensity value among all other layers. In the present data this observation is not reliable due to strong artifacts from ONH swelling. To ensure a spatial choice that respects the anatomical position of this layer, we use information about pixel intensity and position in the gray value profile of each column in a B-scan. For each profile the set P of peaks is detected. From each of these sets, a point p with $d(p, C_1) > 20px$ is added to a list L which meets the condition

$$p = \arg\min_{i} \{d(p_i, C_1)\ , \forall s \in M\}$$

where $d(p_i, C_1)$ represents the distance from the candidate point p to the corresponding point of the upper bounding curve C_1, $d(p_i, s)$ represents the distance between two points, $M = \{x | I(p_{max}) - I(s) < 10\ , \forall s \in P\}$, $I(p)$ the gray value of a point in the intensity profile and p_{max} represents the maximum peak.

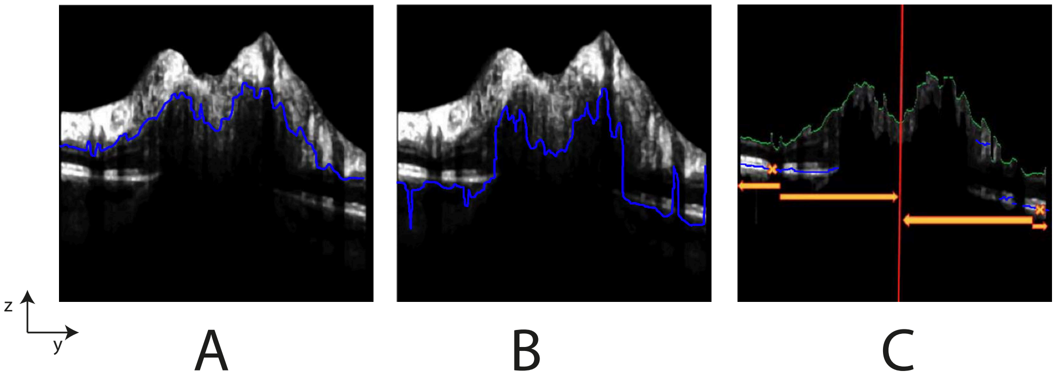

FIGURE 4.3: A.The upper border. B. Lower border. C. The processed image containing the RPE region and the two starting points mark by crosses. Green points contain the upper boundary, and blue ones the initial RPE pixels. The arrow suggests the search direction for RPE pixels included into the list before the spline fitting step, [Kadas et al., 2012a].

From the list L of each B-scan the final selection of points to create the curve describing the RPE layer is constructed. Outliers might still be present in L in B-scans that contain the region of the edema. In this region the only reliable RPE information is at the left, respectively right side of each scan. Two lists $L1$ and $L2$ are created from pixels in L. For each side a point $p(y_i, z_i)$ in the first quarter from left and right of the scan with minimal z_i coordinate is detected. These give the starting reference height for creating two lists. Starting from these seed points to the right and left, pixels are added iteratively to the corresponding list if they meet the following conditions, see Figure 4.3C

$$\begin{cases} |y_i - z_{i-1}| < 5\text{px}, & \text{for } |z_i - z_{i-1}| < 5\text{px} \\ |y_i - z_{i-1}| < 10\text{px}, & \text{for } |z_i - z_{i-1}| < 15\text{px}. \end{cases}$$

In the case of missing image information, RPE segmentation data from the previous scan is taken into account.

4.2.3 RPE Curve

Finally having the two lists, a least square spline approximation is applied to $L1 \bigcup L2$, with knots and order of the spline, quadratic or cubic, depending on the number of pixels of $L1$, respectively $L2$. The scan alignment step is performed by column shifting as described in [Rossant et al., 2009a].

ONH Volume and Height

For the volume measurement a threshold of 20 pixels was applied from the reference height computed at the right side and left side of each B-scan. The areas found on each B-scan, multiplied by the spatial spacing were summed up to obtain the final volume. The threshold of 20 pixels was found through experiments to provide a satisfying result in images from IIH patients as well from healthy controls. The height value represents the maximum height of the ONH. Figure 4.4 illustrates the capability of the algorithm to correctly detect the RPE in ONH with different degree of swelling and different image quality.

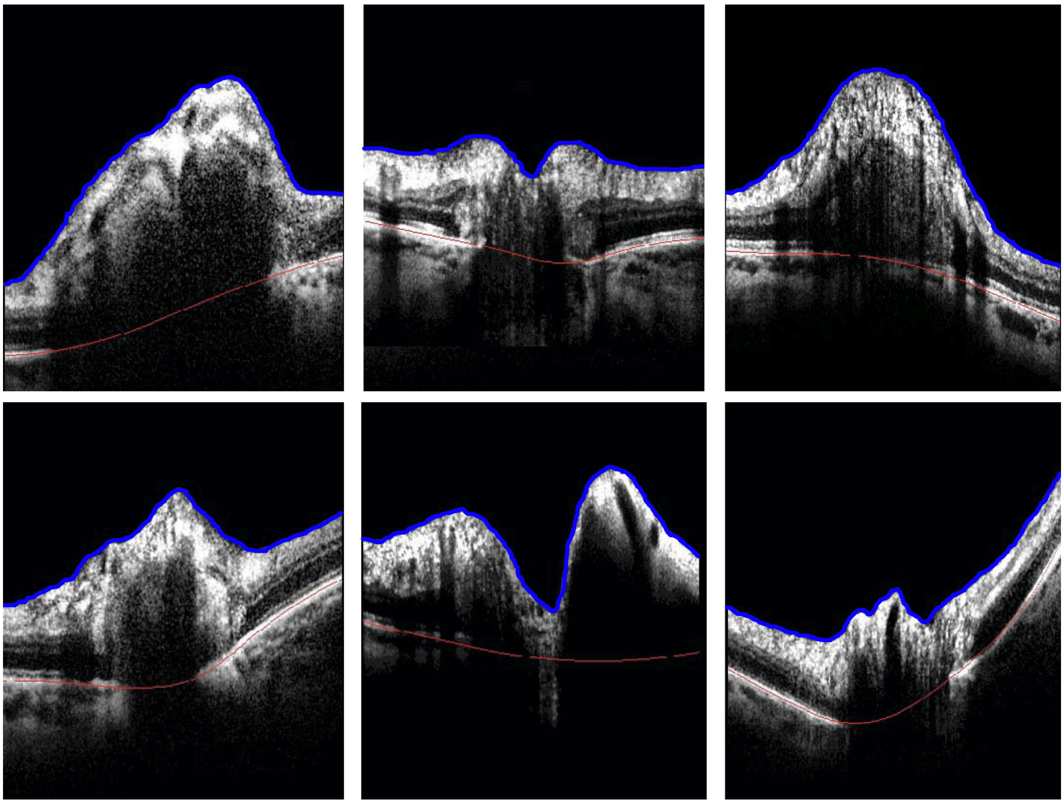

FIGURE 4.4: These images belong to different patients at different position relative to the ONH, and are representative for the different changes that occur in this region. The blue line represents the ILM, while the red one stands for RPE, [Kadas et al., 2012a].

TABLE 4.1: Differences in RPE detection for 2900 B-scans between first expert manual grader and the proposed algorithm (Column I), between the second expert manual grader and the proposed algorithm (Column II). Column III reports the differences between the two manual graders. Each pixel is 3.8717 μm. SD = Standard deviation

RPE Differences (2900 Bscans)	Manual Grader 1 vs. Algorithm	Manual Grader 2 vs. Algorithm	Manual Grader 1 vs. Manual Grader 2
Mean Difference	1.3247 μm	1.4310 μm	1.1572 μm
SD	0.3024	0.3128	0.309

4.3 Validation

To determine the accuracy of the RPE detection we conducted an automatic versus manual segmentation validation study. This study included five randomly selected HC and five IIH patients. In total, 3D scans from 20 eyes, each with 145 B-scans, were manually segmented by two expert graders and compared to the results of the automatic segmentation. The results in Table 4.1 show that the automatic algorithm accurately detected the RPE in HC scans a swell as in scans from IIH patients. The quantitative results indicate a very good agreement and high correlation between the manual graders and our set of measurements. Furthermore, the agreement was comparable to the agreement between two manual graders.

4.4 Results of two clinical studies

IIH

To evaluate 3D SDOCT volume scans as a tool for quantification of ONH volume as a potential marker for treatment effectiveness and disease progression in IIH in a clinical study, 37 eyes from 19 IIH patients and 38 eyes from 19 matched HC were enrolled, see Table 4.2. ONHV was significantly increased in IIH patients (2.3 ± 1.3 mm^3) compared to healthy controls (1.1 ± 0.5 mm^3, GEE, B = 1.2, SE = 0.3, $p < 0.001$), see Figure 4.5A. Maximal ONHH was elevated in IIH (108.0 ± 17.5 μm) compared to HC (102.5 ± 6.9 μm), however, this difference was statistically not significant (GEE p = 0.101), [Kaufhold et al., 2012]. We further divided the patient group into treated and untreated patients. Untreated patients (n = 6) showed a higher ONHV than treated (n = 13) patients (GEE, $p < 0.001$), see Figure 4.5B. Both medically treated and untreated patients had an increased ONHV compared to controls which did not hold true for ONHH, [Kaufhold et al., 2012]. Statistical analyses were performed with SPSS 19 (IBM

TABLE 4.2: Demographic overview of IIH patients and HC. SD = standard deviation.

			IIH	HC
Subjects	No.		19	19
Eyes	No.		37	38
Gender	No.	male	2	2
		female	17	17
Age	Mean (±SD)		38 (±13.8)	37.6 (±12.9)
Disease duration (months)	Mean (±SD)		40 (±37)	
RNFL thickness (μm)	Mean (±SD)		99.1 (±18.1)	99.2 (±8)
TMV (mm^3)			8.48 ±0.4)	8.67 (±0.38)
ONHV (mm^3)	Mean (±SD)		2.3 (±1.25)	1.08 (±0.49)
ONHH (mm)	Mean (±SD)		0.42 (±0.07)	0.4 (±0.03)

SPSS Statistics Version 19, Release 19.0.0.1, IBM, Armonk, NY, USA). For the evaluation of OCT parameters relationship between HC and IIH, and treated and untreated patients we performed GEE analyses with working correlation matrix structure "exchangeable" accounting for inter-eye/intra-patient dependencies.

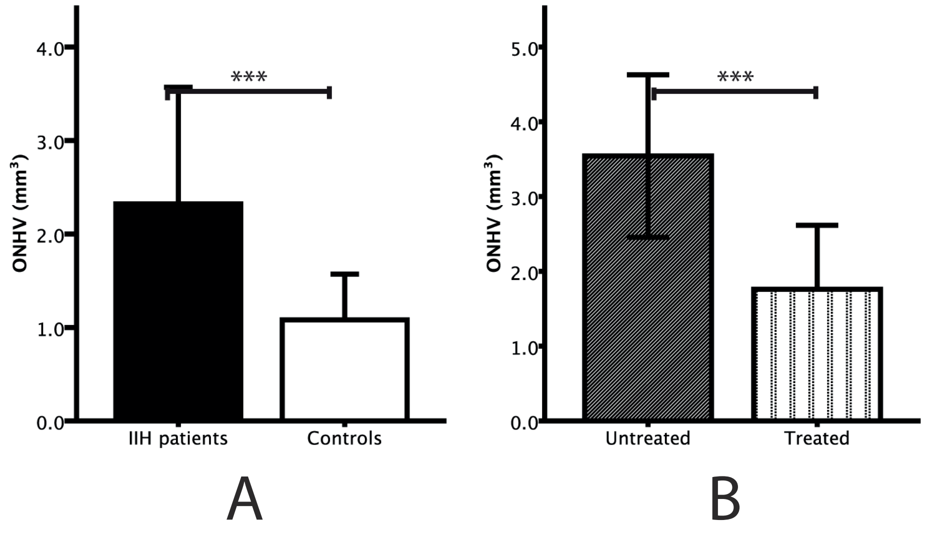

FIGURE 4.5: A. Groups differences in ONHV between IIH patients (black bar) and controls (white bar). B. Group difference in ONHV between medically untreated (gray bar) and treated (vertical lines bar) IIH patients. Error bars represent 1x standard deviation =$p < 0.001$, [Kaufhold et al., 2012].

MoyaMoya

To investigate whether patients with moyamoya angiopathy without obvious retinal pathologies such as retinal infarctions or the congenital morning glory anomaly may have subtle subclinical retinal changes, [Albrecht et al., 2015] enrolled 25 patients with idiopathic moyamoya angiopathy and 25 age and sex matched HC (mean age 40 years and 78% females in both groups). Moyamoya disease is a rare progressive cerebrovascular disorder, caused by blocked arteries at the base of the brain, the basal ganglia, [M. et al., 1998]. Patients with moyamoya angiopathy sometimes also have embolic retinal infarction, and can present morning glory anomaly, a rare congenital abnormality of the optic disc characterized by a funnel-shape excavation of the posterior fundus that incorporates the optic disc, resembling the morning glory flower [Lee and Traboulsi, 2008]. The main finding of this study was a pronounced reduction of the ONH volume in moyamoya angiopathy compared with controls (0.76±0.45 mm^3 and 1.47±0.50 mm^3, respectively; $p < 0.0001$), which was associated with a less pronounced reduction of the retinal nerve fiber layer in macular volume scans (0.97±0.11 mm^3 and 1.10±0.10 mm^3, respectively; $p < 0.001$) [Albrecht et al., 2015]. Autofluorescence and MultiColor confocal scanning laser ophthalmoscopy images revealed no pathologies except for one branch retinal artery occlusion, which was excluded from the analysis of the OCT measures, [Albrecht et al., 2015]. Statistical analyses were performed using Microsoft Excel, Prism 5.0 (GraphPad, La Jolla, CA), and SPSS Statistics 20 (IBM, Armonk, NY). GEE models accounting for within-subject inter-eye correlations using an exchangeable correlation structure correcting for age and sex were applied to test for differences in the OCT measures between patients with moyamoya angiopathy and controls.

Development environment

Algorithm development was done using Matlab R2011A with Spline library (Mathworks, Germany) on Mac OS X (Apple, Cupertino, CA, USA, Intel Core i5, 4GB memory). The algorithm requires 1.5 to 2 minutes for the whole computation.

Chapter 5

BMO points detection for ONH center and ONH volume computation

We propose an algorithm for the detection of the BMO points directly in the 3D SDOCT scans centered on the ONH. Our main goal was to provide assessments of the ONH shape for the further application in investigating neurological disorders like MS (with its sub types), NMOSD, and IIH. BMO points provide a stable reference for the computation of the ONH even in cases where the morphology of the ONH might undergo changes under the influence of a disease, a characteristic presented in detail in Section 5.1. Therefore our approach focuses on detecting these points, thereby providing the necessary information for deriving important parameters for clinical analysis. These parameters consists of measurements of different areas of the ONH and the volume region comprised in a cylinder around the ONH center point.

5.1 Previous approaches in ONH volume computation

ONH is one of the main components on the retina. Assessment of its 3D shape is often studied in eye diseases [Abràmoff et al., 2010]. Although ONH measurements are still performed extensively on 2D fundus photographs, 3D shape of the ONH can fully reveal reliable parameters [Bhavna et al., 2014]. We present the methods that had been developed and the histological motivation towards quantifying the ONH in 3D OCT data. All of the methods discussed in this section were developed to investigate ophthalmological diseases, the majority focusing on extracting features to characterize glaucoma. Glaucoma is the second most common cause of blindness, characterized by progressive damage of the optic nerve [Quigley and Broman, 2006].

ONH in fundus photography

Although various ocular imaging instruments, such as HRT and OCT, provide 3D information and clinically useful quantitative assessment of glaucoma diagnosis and management, it is still a clinical standard and routine to perform subjective optic disc assessment using disc photographs [Abràmoff et al., 2010]. The disc assessment usually consists in the manual delimitation of the optic disc and optic cup by glaucoma specialists and the computation of the ratio of the optic cup and neuroretinal rim surfaces, or cup-to-disc ratio. However, it has been shown that manual computation is time-consuming with substantial interobserver variability [Xu et al., 2006].

ONH in stereo disc photography

Stereo disc photograph has been used to document structural abnormality/changes in glaucomatous 3D reconstruction of the ONH shape [Abràmoff et al., 2010]. One of the limitations of stereo disc photography, however, is that there is no fully automated ONH quantification method available. Conventional ONH evaluation consists in manually labeling the disc and cup margins and consequently generating several disc parameters from these two structures. This procedure is time consuming and prone to high intra- and inter-observer variability [Xu et al., 2006].

[Juan et al., 2010] developed a fully automated algorithm to perform a volumetric measure of the optic disc using conventional stereoscopic ONH photographs. A hybrid approach was used, where the cup margin was located at a fixed distance from the disc margin for average size cups, and a relative distance for large and small cups. Image features, such as pixel intensity value, gradient, and contour smoothness, were extracted and used in the computation of the deformable model. The limitation of this study was the substantial failure rate of the algorithm method (23.8%). The main causes of the failures were the presence of pathologic features such as peripapillary atrophy, which reduced the visibility of the disc margin.

ONH in HRT

The HRT shows the 3D surface topography of the ONH, which allows for quantitative analysis of glaucomatous changes of the ONH. The commercial software available defines the optic cup to be $50\mu m$ below the mean surface height along a six degree annulus at the temporal inferior disc margin. Although it is a well-defined method for ONH analysis, it requires manual delimitation of the disc margin to define a reference plane that is then used to calculate the cup margin. Because accurate determination of the disc margin depends on the skill of the operator, calculation of the cup margin is also affected by it [Juan et al., 2010].

Comparison of ONH parameters in stereo disc photography, TDOCT and HRT

[Juan et al., 2010] also compared algorithm-produced parameters with manual photogrammetry, by using HRT and OCT measurements. The optic disc margin was manually delineated at the border of Elschnig's ring and the disc parameters were generated by the HRT3 software. The OCT used in the study was a TDOCT, in which the software defines the optic cup below a reference plane located 150 μm superior to the RPE/BM tips. The disc margin was automatically defined at the termination of the RPE in each of 6 radially sampled cross-sectional retinal images. The OCT software generated a disc margin by interpolating these 12 detected points. Manual correction was required if the disc margin was not correctly placed at the end of RPE. Non-constant bias was noted for most measurements between the methods indicating a difference that changes with the imaging modality employed. Therefore, measurements are not inter-changeable between modalities.

It should be noted that all the presented methods used subjective input for their ONH definition.

BMO points as a stable parameter for ONH center and ONH volume computation

The choice of BMO points for the computation the ONH center has an important anatomical motivation. Several studies conducted compared these landmarks and the optic disc in histological ONH, SDOCT and fundus photographs [Kotera et al., 2009, Reis et al., 2012, Strouthidis et al., 2009b]. These have proven that BMO points are a stable parameter even in case of changes that ONH undergoes during degeneration, as in diseases like glaucoma. We present a short summary of these findings in order to explain prior approaches that focus on detecting these points, as well as our choice in developing the BMO points detection algorithm presented in this chapter that employs these points for ONH center and volume computation.

In a series of recent publications [Strouthidis et al., 2009b] have proposed three important concepts that are necessary to understand optic disc margin anatomy within 3D histomorphometric and SDOCT reconstructions of the monkey ONH. The first concept is that of a NCO, which is the anatomic opening in BM through which retinal ganglion cell axons must pass to enter the choroidal and scleral portions of the neural canal. The second concept is that of a ‘neural canal’ which is the axonal pathway through the eye wall. The neural canal begins at the NCO, and then extends through a choroidal component, bound on either side by the border tissue. The neural canal terminates at the point at which the optic nerve leaves the globe. The third concept is that, what the clinician perceives to be the disc margin is not a single anatomic structure, but is instead variable structure with some portions being the NCO, and others the border tissue or the anterior scleral canal opening, depending upon the 3D architecture of these structures.

When examining the 3D point cloud generated from the human SDOCT ONH volume [Strouthidis et al., 2009b] have confirmed their previous histomorphometric report that the BMO and not the disc margin will become the basis for an SDOCT reference plane for the ONH. Within SDOCT volumes, the innermost termination of the presumed RPE/BM signal was delineated as the BMO. Furthermore, clinical co-localization of SDOCT detected disc margin anatomy will provide the clinician with the necessary information for the interpretation of the disc in glaucomatous ONH.

Subsequently, [Kotera et al., 2009] have compared the photographic disc margin with the SDOCT defined disc margin in glaucomatous eyes. In that study, a high concordance between the photographic disc margin and the SDOCT disc margin was found. Unlike the previous study, the observers delineated either the termination of the RPE or the termination of the “highly reflective, curved line”, which connected to the straight signal identified as the RPE. This highly reflective, curved line is the signal identified as border tissue. Additionally [Kotera et al., 2009] have shown cases where the termination of the RPE identified by SDOCT coincided with the termination of visible retinal pigment at the edge of peripapillary atrophy.

[Reis et al., 2012] emphasized the findings previously presented. They have shown that BM and its terminations are key structures of the ONH and their variations. Assessing the neuroretinal rim requires a stable and consistent anatomical landmark and an actual anatomical border and, as such, recognizing BMO may prove vital. They also showed that the clinically identified disc margin is a clinical construct that does not reference a consistent anatomical structure within or between eyes.

In all the approaches mentioned before, BMO points were manually delimited.

BMO points detection for ONH center and ONH volume computation

A first attempt to quantify the ONH from 3D OCT images is presented in the work of [Abràmoff et al., 2009]. The purpose of this preliminary study was to determine the performance of the algorithm's cup–rim segmentation from SDOCT images to planimetry by glaucoma experts in patients with glaucoma or suspicion of glaucoma. In this study automatic segmentation of 3D SDOCT scans, centered at the ONH, by a novel voxel column classification algorithm was presented. Reference standard from fundus photographs was used as truth in the training phase. However, this approach has the limitation that the algorithm essentially mimics the subjective assessment of 2D parameters by human experts. It is not based on objective anatomic landmarks within the 3D volumes, and the optic disc margin does not overlap with a single constant anatomic structure in 3D OCT.

To overcome this limitation [Hu et al., 2010a] presented an automated graph-theoretic approach to identify the BMO and cup. BMO-based metrics were compared with the reference standard for cup and disc margins from the images manually delineated by glaucoma experts. Four intraretinal surfaces, ILM, IS/OS, the inner boundary of the RPE/BM complex, and the outer boundary of the RPE/BM complex were segmented. The 3D OCT volume was flattened based on the second segmented surface, the IS/OS. A projection image from a thin layer at the RPE/BM complex was created for correspondingly comparing the NCO-based parameters with those of fundus photographs. Finally the projection image is unwrapped to polar coordinates and a signed edge-based term is used as a cost function in a directed graph to simultaneously segment the (optimal) BMO and cup boundaries. The BMO and cup boundaries were finally smoothed using a B-spline.

There are several limitations to this preliminary study. Because of the large variations in the surface of the ONH, intraretinal layer segmentation differences can occur and cause a non-optimal flattening problem (i.e., the BMO points do not lie on a plane after flattening). For the 2D measurements on the projection image, the non-optimal flattening problem was corrected by extrapolating the average radial positions outside the estimated BMO with those inside it. Although small discrepancy existed between the BMO and the clinical disc margin in some eyes, the relative stability of the BMO reference plane and the objective nature of the algorithm makes the measurements of the BMO-based 2D or 3D glaucomatous parameters in 3D OCT scans more reproducible than those of the reference standard.

[Bhavna et al., 2014] proposed a different approach to detect the BMO boundaries to overcome an important issue in the method proposed by [Hu et al., 2010a], namely the fact that the surfaces detected by [Hu et al., 2010a] do not actually exist inside of the BMO. Therefore in the graph-based segmentation step the surfaces are pulled away from the true locations near the boundary of the BM towards deeper underlying structures. The method proposed by [Bhavna et al., 2014] combines a graph-theoretic approach in the 3D SDOCT and a 2D projection image from retinal layers by considering the BMO as a “hole” embedded with multiple surrounding surfaces. An iterative approach that simultaneously segments the surfaces in the RPE-complex as well as the BMO is proposed. In particular, the general framework of their approach reflects an extension of the graph-theoretic approach by incorporating costs associated with this additional structure (the hole boundary).

The method begins with an initial segmentation of three surfaces, namely the ILM, the IS/OS line and the BM in the volumetric image. In order to find a smooth representation of a surface that cuts through the optic nerve disruption, a TPS is fit to the segmentation of the BM. A projection image was then created using this interpolated smooth surface after fitting the TPS to the IS/OS line. This projection image is then polar transformed so that the BMO boundary appears as a line in the image instead of a circle, and was segmented using a graph-theoretic approach similar to the method proposed by [Hu et al., 2010a].

Next, given this “fixed” set of hole boundary columns, the corresponding optimal set of feasible surfaces that meets at the hole boundary in the volumetric image is found in an iterative manner. The cost function for boundary also incorporated textural features learned from a training set. The biggest drawback for the iterative approach proved to be the presence of the end point of the border tissue. The machine-learning based “corner” detection was able to locate the BMO point. However the endpoints of the border tissue share “corner”-like features, and the classifier was not able to differentiate between them, leading to the preferential detection of the border tissue.

Contribution

The method presented in this chapter extends the RPE detection of our previous approach [Kadas et al., 2012a], and improves several aspects of previous ONH volume detection algorithms as follows:

- it detects the BMO points directly in the 3D SDOCT scans, without making use of any projection images as in the approaches proposed by [Bhavna et al., 2014, Hu et al., 2010a]
- it is able to detect BMO points in swelled, normal and atrophic ONH, and does not rely on features specific to glaucoma (atrophic ONH) unlike all approaches presented in the previous section
- it reduces the search of the RPE region from the previous algorithm [Kadas et al., 2012a], by first approximating the ONL
- to account for motion artifacts and sudden jumps in consecutive scans, but also for the natural curvature of the retina, we propose an efficient two-stage TPS, that improves the approach proposed by [Garvin et al., 2008] without making use of the orthogonal scans presented in the work of [Bhavna et al., 2014]
- we significantly reduce the computational time by extracting a sub-volume from the initial 3D SDOCT scans that approximates the BMO region
- we present a modified grow-cut algorithm that requires no user interaction, where we redefine the strength function by incorporating information from the sub-volume with suppressed vessels and enhanced RPE using textural filters; also we address the slow convergence of the algorithm by reducing the number of unknown labeled voxels in the initialization stage.

We tested our algorithm in a clinical study in order to investigate how well ONHV correlates to OCT standard measurements in HC, MS, NMOSD and IIH. A detailed description of the study is presented in Section 5.4. Our results were also presented at the NANOS conference in February 2015 [Kadas et al., 2015].

5.2 Algorithm description

In the following section we present a detailed description of the proposed BMO detection algorithm. Spatial ONH scans were performed using a custom protocol for high-resolution ONH imaging with 145 B-scans focusing on the optic nerve head with a scanning angle of $15^\circ \times 15^\circ$ and a resolution of 384 A-scans per B-scan. The main steps of the algorithm are illustrated in

Figure 5.1.

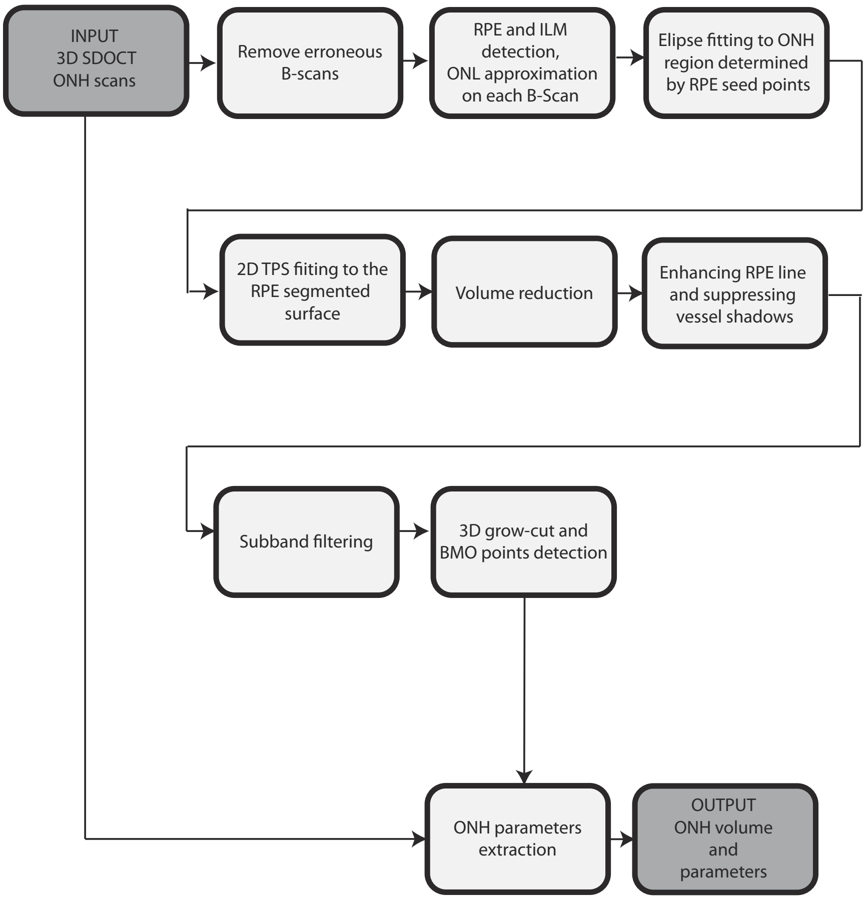

FIGURE 5.1: The main steps of the BMO detection algorithm.

Removing scans containing erroneous data

Although the OCT device used for the data acquisition is equipped with a tracking system to reduce motion artifacts, the scans used in our research, however, are prone to some artifacts, which are thought to be caused by a number of factors such as motion of the eye, positioning of the camera, or defocus. These artifacts not only make it difficult to visualize the data, but they also affect the further processing of the images. Therefore our first step consists in preparing the data for computation, by removing erroneous data. There are three types of artifacts commonly seen in our OCT ONH scans:

- missing information, i.e. the B-scan wasn't acquired entirely and the information is missing on the y axis, or on the z axis, see Figure 5.2A.
- bad illumination and noise present in different regions of the B-scan make the detection of the retinal layers inapplicable, see Figure 5.2B.
- the entire B-scan contains only noise and random data, see Figure 5.2C.

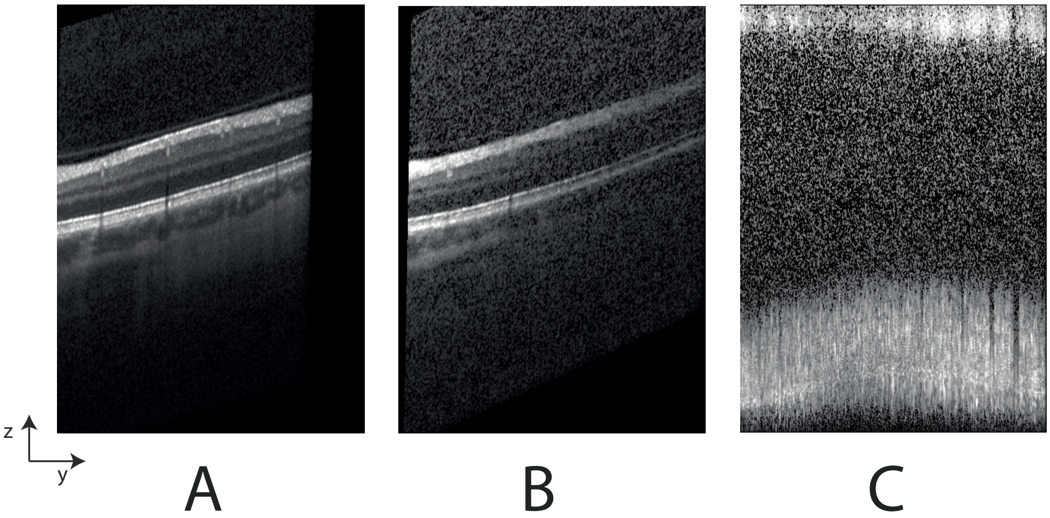

FIGURE 5.2: A. B-scan with missing information on the right side. B. B-scans with noise and bad illumination C. B-scan with erroneous data

In order to remove these B-scans we make use of the ILM boundary information provided by the OCT device, as follows. If the ILM pixel position information is missing more then 50 pixels to left, to the right, or is at the upper border (pixels with position 1 on the z axis), or on the lower border (pixels at maximal position on the z axis) of the B-scan, the B-scan is regarded as having missing information. These criteria are fulfilled also by B-scan containing an erroneous part (bad illumination, or extreme noisy information). In the case of complete erroneous data, the ILM position information is either partly or entirely missing. The ONH scan protocol consists of 145 scans, comprising an area of major interest in the study of the ONH feature analysis. In order to maintain consistency among our data for further comparison, we need the entire scan information. Consequently we discard 3D scan that contains erroneous data in more then 5 B-scan, if these are among the first 10, or the last 10 B-scans (in the x axis direction), or in more then 3 B-scans if these are between scan number 10 and 135 (as the region between these scans contains the valuable information - BMO region). The removed B-scans, if these fit the aforementioned criteria, are replaced by interpolated neighboring B-scans.

5.2.1 Detection of ILM, ONL and RPE lower boundary

In the second step of our method the goal is to detect the ILM and the RPE lower boundary, and to approximate the ONL. We need the ILM and RPE lower boundary for the volume and for the parameters computation, described later in Subsection 5.2.5. Our approach does not make use of other retinal layer segmentation. We only approximate the ONL region for reducing the computational load in a further step, when we define the partial 3D volume used for the BMO points computation. It is well known that retinal layers in OCT scan are identified by two retinal surfaces separated by dark-to-bright or bright-to-dark transition of voxel intensities from top to bottom in OCT scan [Garvin et al., 2008]. The RNFL and RPE are distinctively bright, while the IPL and OPL are of medium intensity and the INL and ONL have low intensity, see Figure 2.15.

ILM is a hyper-reflective membrane delimiting the retina from the vitreous. Therefore the only difficulty in applying a direct detection using the gradient magnitude, to detect the transition from dark-to-bright, occurs when the vitreous contains different regions with high reflectivity or there is a second membrane detached from the ILM that causes the gradient to present a high magnitude before the ILM. To account for this problem our method starts by creating three multi-scale OCT volumes subsampled by a factor of 2 in the z axis. Level 1 represents full resolution, and level 3 is the lowest resolution. This subsampling process has the effect of reducing speckle noise in OCT volumes of low resolutions so that ILM and ONL have clear borders in the low resolution. At each level we apply a 2D Gaussian smoothing ($\sigma = 3$ pixels isotropic) on each B-scan. The ILM and ONL borders are detected in an iterative manner as follows.

The maximum gradient magnitudes of the dark-to-bright transition from top to bottom are detected, at level 3, representing the initial ILM and ONL borders. The positions are smoothed by applying a 5 pixels moving average filter on each B-scan separately. This averaging step acts to smooth out smaller outlying boundary points, often caused by variations in the pixels intensity. These positions provide the approximate z-positions of ILM and ONL in level 2 by multiplying the z-positions of borders in level 3 by 2. The process of detecting the maximum gradient is repeated at level 2 and at level 1, with the difference that abrupt jumps in the positions of the ILM or ONL boundary points are replaced with positions detected prior at level 3, level

2, respectively. These abrupt jumps are defined by pixel positions that are more then 5 pixels higher/lower then the neighboring pixel positions on the z axis.

The reason for not applying a 3D smoothing filter at this stage is the presence of another motion artifact, we address in the next subsection. This artifact, illustrated in Figure 5.3, has the drawback of leading to altered image information propagated through the entire volume when 3D contextual information is used at this stage.

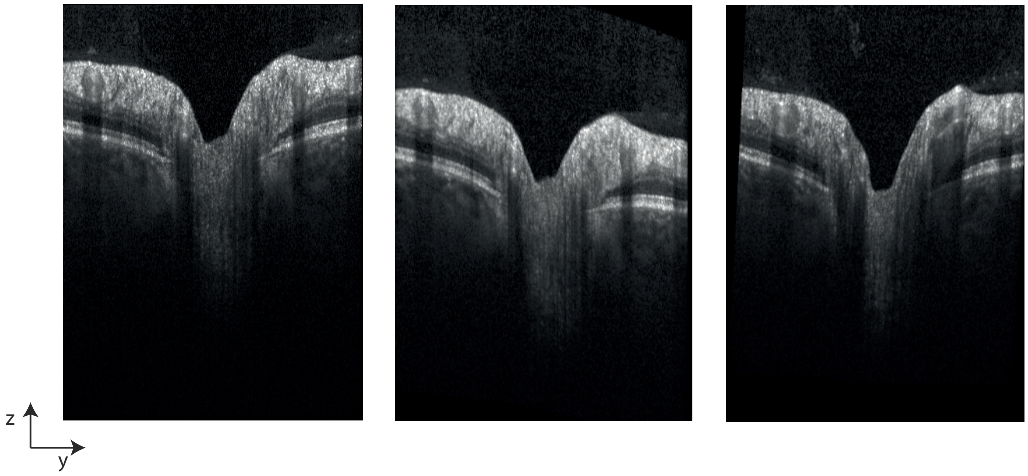

FIGURE 5.3: Three consecutive B-scan showing strong displacement on the z axis.

The RPE lower boundary detection is based on our previous method described in Section 4, with the main difference in the Step 2 of the algorithm. In our current approach we reduce the computation load of the cubic polynomial fitting for the two regions by using the ONL approximated positions, to delimit the search area for the RPE lower boundary pixel candidates.

5.2.2 Modified TPS fitting

The method described in this step addresses the presence of motion artifacts using a modified TPS fitting. Moreover, this approach helps to constrain the search area for the final segmentation, by reducing the algorithm sensitivity to the retinal curvature. The main motivation in using TPS as a smoothing preprocessing step is its capability not only to remove motion artifacts but also to reconstruct the “true” shape of the retina, namely an ellipsoidal shape dependent of the curvature of the eye ball [Bhavna et al., 2014]. Furthermore compared to 1D (A-scan correction) and 2D (B-scan correction) approaches it incorporates 3D contextual information, therefore reducing the artifacts that might arise in previous methods by interpolation only of

1D, 2D information [Garvin et al., 2008]. The artifact correction process needs a stable surface to which a TPS can be fit. Therefore, the RPE lower boundary is used, as it can be reliably detected in OCT volumes, as we have seen in our previous RPE lower boundary detection algorithm in Section 4. At this stage, the method considers evenly distributed grid points on the surface defined by the RPE lower boundary curves. The number of grid points is set to 10 in the x direction and 20 in the y direction, with the regularization parameter $\lambda = 0.7$. One important difference at this step compared to other works using TPS [Garvin et al., 2008], [Bhavna et al., 2014] consists of the definition of the grid points over the entire RPE surface, without discarding points in the ONH region. The reasoning behind this choice is that the RPE curves detected in our previous algorithm (Section 4) already created a hypothetical extension of this anatomical structure through the ONH. This choice of grid points has proven to provide a smooth surface that reduces the artifacts in the yz plane.

While demonstrating robustness against any small local errors in the initial segmentation result of the RPE lower boundary and reducing the motion artifacts, TPS is still sensitive to sudden height changes in the original scan, see Figure 5.3. To account for this effect we modified the method by introducing an additional correction step that removes the extreme points in a first TPS least-square approximation stage then performs the actual TPS fitting described above. The outline of the algorithm is presented in Algorithm 2

```
Data: RPE surface $S$ coordinates
Result: TPS coordinates $S_1$
Initialization: resample grid points on $S$ ;
compute surface $S_0$ = TPS with $\lambda = 0$ (least-squares approximation);
compute $mean_i$ and $SD_i$ (standard deviation) for each list $l_i$ of coordinates in $S_0$;
compute reference $mean_R$ = mean with $SD_R$ = min$(SD_i)$;
compute list of extreme points $L_0$ of the surface $S_0$;
while $L_0 \neq 0$ do
    if $(x_i, y_i) \in L_0, S_0(x_i, y_i) > mean_R + SD_R$ or
    $(x_i, y_i) \in L_0, S_0(x_i, y_i) < mean_R + SD_R$ then
        remove $(x_i, y_i)$ from $L_0$;
        replace $S_0(x_i, y_i)$ with $(S_0(x_{i+1}, y_i) + S_0(x_{i-1}, y_i))/2$;
    end
end
compute surface $S_1$ = TPS with $\lambda = 0.7$;
```

Algorithm 2: Modified TPS

Figure 5.4A shows the initial TPS fit from a data with strong motion artifacts (B-scans of this data can be seen in Figure 5.3). The corresponding zero level sets of the derivatives (green contour - derivative in the y direction, red contour - derivative in the x direction) and gradient vectors (in blue) are illustrated in Figure 5.4B. Red and green lines crossings represent a point where the derivatives are both zero and hence it is either a local extremum or a saddle point. Notice how the two stage TPS, see Figure 5.5, was able to remove the points that caused strong oscillations in the initial TPS.

Alignment

The retina in OCT scans is curved due to the natural scleral curvature and while this is not an artifact, removing temporarily this curvature is advantageous in our further analysis, as we want to bring our data into a consistent format. Alignment or flattening is a common preprocessing step performed by many retinal segmentation algorithms [Abràmoff et al., 2009, Bhavna et al., 2014, Garvin et al., 2008] and refers to translating all of the A-scans in each B-scan such that a chosen boundary in the image is flat. We choose to align the retina to the smoothed RPE lower boundary obtained after the TPS fitting. A result of the ILM surface before the alignment to the smooth RPE surface and after is shown in Figure 5.6A, Figure 5.6B, respectively.

5.2.3 Volume reduction

Our data set is a volume of $384 \times 496 \times 145$ voxels. At this stage of our approach we have all the prerequisites to reduce the volume to a smaller one containing our 3D region of the BMO. For this step we make use of the RPE pixel candidates from our RPE lower boundary detection algorithm, see Section 4. A 2D binary image is created containing the projected RPE pixel coordinates onto the xy plane. The pixels are coded with 0 in the binary image. Note RPE pixel candidates are not present at the ONH, as this information is missing due to the anatomy of the ONH. Also some regions in each B-scan are missing RPE pixels because of the presence of blood vessels. Thus the 2D projected image contains some spurious regions. To remove them we make use of several morphological operations. First we detect the largest connected component (corresponding to the ONH region), remove all the other components, and dilate it with a disk element of 4 pixels. The result is a smooth enlarged ONH region. By fitting an ellipse to this region, we define our area for the volume reduction, in the y direction $2\times$ the minor axis, in the x direction $2\times$ the major axis of the ellipse. The volume is also reduced in the z direction, by considering only voxels between the ONL approximation boundary, and 50 pixels bellow the RPE coordinates smoothed by the TPS fitting. Thus depending on the ONH region fitted by the ellipse and the position of RPE and ONL, we reduce for example our volume from $384 \times 496 \times 145$ voxels to $210 \times 90 \times 52$ voxels. Figure 5.8A illustrates a C-mode image of a ONH volume scan with the ONH region delimited by the red rectangle. This region was used in this example for the volume reduction process.

C-mode images are 2D projections in the xy plane, obtained by taking, for example see Figure 5.8C, the maximum grey values from the RPE boundary 50 pixels in the z direction on each B-scan. This projection image provides a view of the vessel map (shadows, or dark intensity regions in the RPE layer) and the BMO region. This type of C-mode image was used in other approaches [Abràmoff et al., 2009, Bhavna et al., 2014, Hu et al., 2010a] to segment the ONH. These methods rely strongly on the existence of the optic disc and optic cup, especially in eyes with glaucoma, which is not always the case in our data. Figure 5.7 illustrates two different ONH types. One with a strong excavation in Figure 5.7A.1. and one with no cup in Figure

5.7B.1. Both images represent B-scans at the same position in the two 3D volumes at the ONH. Red arrows represent the BMO points. The C-mode images at different z position in the 3D volume seen in Figure 5.7A.2-4 present similar characteristics seen in the approaches mention above. Figure 5.7A.4. is the C-mode image projected from a thin layer at the RPE, and it is used to detect the BMO (this is represented by the black area). Notice that these images, in the case of an ONH with no cup, Figure 5.7B.2-4, present different features.

In our approach we use the C-mode image only for visualization purposes.

5.2.4 Vessel suppression

We have demonstrated in Section 3.3 the capability of the 2D Morlet wavelet in detecting linear structures. Vessels appear in the RPE layer as dark intensity regions, or shadows (see Figure 5.8B.1 and C.1). These affect the detection of the BMO, especially because vessels gather at the ONH region to leave the optic nerve, or enter through the optic nerve, creating large shadows. Our approach focuses on emphasizing the RPE layer and on suppressing these shadow artifacts. To this end we apply a 2D Morlet wavelet filter for each B-scan of the reduced volume to enhance the RPE line. Using the Morlet transform, see Equation 3.5, the scale parameter a is held constant and the orientation varies $\theta = \{170°, 175°, 180°, 185°\}$, in order to enhance almost horizontal lines and suppress the vertical ones representing blood vessels. The results can be seen in Figure 5.8B.2, and C.2.

5.2.5 BMO points detection using textural information in a grow-cut setting

The retinal layers can be interpreted from a texture analysis point of view, in order to combine them in similar regions, or to extract relevant features for further classification in an intraretinal layer segmentation process. An intensive work in this direction has been proposed by [Bhavna et al., 2013], where different classical texture analysis methods were tested for their ability to improve segmentation in a 3D graph-cut setting. Among these methods are intensity-based features (mean intensity, variance, entropy, kurtosis and skewness), co-occurrence matrix features (energy, entropy, contrast, correlation and inverse difference moment), run-length features (short run, long run, gray level non-uniformity, run length non-uniformity and run percentage). In addition, features generated using a variety of filter banks such as Haar, Gabor, and steerable-Gaussians were applied.

At this stage of our algorithm, we are interested in enhancing the RPE line by removing certain periodicities that appear in the resulting B-scans after vessel suppression. To this end we adapt a different method as the ones mentioned above, the sub-band multiresolution filtering (SMF) process using an orientation pyramid (OP) tessellation of the image space. [Reyes-Aldasoro and Bhalerao, 2006] introduced this method in the setting of medical image textural analysis, emphasizing its capability of detecting relevant features that are not emphasized by methods developed for natural images as the ones proposed by [Bhavna et al., 2013]. To subdivide the frequency domain of an image into smaller regions [Reyes-Aldasoro and Bhalerao, 2006] use two operators, quadrant and center surround see Figure 5.9A. By combining these operators, it is possible to construct different tessellations of the space, one of which is the OP, see Figure 5.9B. A band-limited filter based on truncated Gaussians is used. The filters are real functions which cover the Fourier half-plane. Since the Fourier transform of a real signal is symmetric, it is only necessary to use a half-plane to measure sub-band energies.

The quadrant and center-surround operator in the frequency domain of each B-scan of the volume after vessel suppression is divided into smaller region by use of 7 filters, one for the low pass and six for the high pass. Region 1 according to the notation seen in Figure 5.9B is chosen as the space containing the relevant RPE feature enhanced in each volume. Results of applying SMF to the B-scan in Figure 5.8B.2 can be seen in Figure 5.9C. We have discarded regions 2, 3, 6 and 7 as they are dominated by noise-like pattern and region 4 and 5 because they emphasize also the transition between RPE and choroid, and ONL and upper retinal layers.

We create 4 feature volumes as follows. For each of our 3D reduced volumes, for the original one and for the one after applying vessel suppression, we create another volume by re-ordering the voxels in the xz direction. Denote the 4 volumes created by:

- O The original volume
- O_r The original volume in the xz direction
- V The volume with suppressed vessel after SMF
- V_r The volume in the xz direction with suppressed vessel after SMF

A voxel p belonging to RPE would have, according to this notation, high intensity in O and O_r, and low intensity in V and V_r. A voxel q belonging to the ONH region would have complementary intensity values. Thus each voxel p_i has a list of intensity values contained in a feature vector $V_{p_i} = (a_{iO(p_i)}, a_{iO_r(p_i)}, a_{iV(p_i)}, a_{iV_r(p_i)})$.

A modified 3D region grow based on the *cellular automata* algorithm, also known as *grow-cut* in image processing [Vezhnevets and Konouchine, 2005], that uses the feature vectors created is applied to classify the voxels in RPE and background. This algorithm is presented as an alternative to graph-cuts. The operation is very simple, and can be interpreted as a biological metaphor: each image pixel is a "cell" of a certain type. These cells can be foreground, background or undefined. As the algorithm proceeds, these cells compete to dominate the image domain. The ability of the cells to spread is related to the image pixel intensity. A *cellular automata* is a triplet $CA = (S, N, \delta)$, where S is a non-empty state set, N is the neighborhood connectivity type, and δ is the transition function. This function defines the rule of calculating the cell's state at $t + 1$ time step, given the states of the neighborhood cells at previous time step t and it depends on the similarity function between two cells and the strength of the current cell, both defined later in this subsection. The cell's state S_p is actually a triplet (l_p, Ψ_p, V_p), where $l_p \in \{0, 1, -1\}$ is the label of the current cell (foreground $= 1$, background $= 0$ or unknown $= -1$), $\Psi_p \in [0, 1]$ represents the *strength* of the current cell, V_p is the feature vector created at a previous step. We modified this method to classify voxels as belonging to RPE or to the ONH region as described in Algorithm 3.

```
Data: List of voxels with initial state (RPE, ONH region or unknown) and the strength
      function for every voxel
Result: List of voxels with final state (RPE or ONH region and background)
for each voxel p with unknown state do
    if p is weak, i.e. $\sum_{q \in N(p)} \underset{l_p^t \neq l_q^t}{l} \geq 4$ then
        $S_p^{t+1} = 0$
    end
    else
        copy previous state: $S_p^{t+1} = S_p^t$, $\Psi_p^{t+1} = \Psi_p^t$ ;
        for each voxel $q \in N(p)$ do
            if $g \cdot \Psi_q^t > \Psi_p^t$ then
                $S_p^{t+1} = S_q^t$;
                $\Psi_p^{t+1} = g(p) \cdot \Psi_q^t$
            end
        end
    end
end
```

Algorithm 3: Grow-cut algorithm for classifying voxels belonging to either RPE or ONH region

Ψ_p^t denote the strength of a voxel p at time t, S_p^t denotes the voxel's state at time t, $N(p)$ denotes neighboring voxels of p (in our implementation we used 6-connectivity), g is a similarity function. A novelty of our method consists in redefining the decreasing function g, such that this incorporates the information from the feature vector V_p as follows. We defined g as

$$g(p) = e^{-\|V_p - V_q\|}\ , q \in N(p). \tag{5.1}$$

Additionally, compared to the approach presented in [Vezhnevets and Konouchine, 2005] our method requires no user interaction as the labeling in the initialization stage of the algorithm is performed automatically. This also reduces the computational complexity. We label the input data in voxels belonging to RPE, ONH region or unknown in the V volume based on the assumption that two thirds of the smoothed RPE lower boundary position (from left, and right) are correctly identified as belonging to the RPE and voxels with intensity higher then the mean intensity of the RPE lower boundary surface belong to either ONH region or other retinal structures. Therefore the remaining voxels are labeled as background. Thus a considerably amount of voxels is already categorized before the *grow-cut* algorithm begins. Also we define the strength function Ψ to incorporate information about the labels in the initialization stage as follows: $\Psi_p = 0$ if $l_p = 0$, $\Psi_p = 1$ if $l_p = 1$, if we have a voxel labeled as unknown, $l_p = -1$, that is close to a foreground voxel, i.e. $min(\|p - q\|) \leq 15$, $q \in N_{foreground}(p)$, where $N_{foreground}(p)$ contains only the voxels q labeled as foreground, then $\Psi_p = 0.8$. For all the other unknown labeled voxels $\Psi_p = 0.4$.

Another important aspect that reduces the computational time is achieved by defining *weak* voxels, that will not be considered for further processing. These are represented by voxels surrounded by 4 or more already labeled foreground voxels. The *grow-cut* algorithm, summarized in AlgorithmCAAlg, terminates after a fixed number of iterations K or when no pixels change state. Convergence is guaranteed when K is sufficiently large because the updating process is monotonic and bounded [Vezhnevets and Konouchine, 2005]. Figure 5.10 shows three B-scans at the ONH with the classified RPE voxels depicted in white. The red arrows show the end points of the RPE surface detected, and represent the BMO points. Figure 5.11 shows several B-scans with correctly identified BMO points. In Figure 5.12 some examples of B-scans are shown where the shadows on the RPE layer created by the presence of the blood vessels in the upper layers made the algorithm misclassify the BMO points.

Parameters extraction

A smoothing technique using a mean filter is applied to the BMO points to remove any outliers that might have been wrongly detected. The centroid of all BMO points is computed as the ONH center. Several ONH parameters can be derived from the ONH center and BMO points.

- the ONH volume is defined inside a cylinder with a radius of 1.7 mm centered at the ONH, see Figure 5.13C
- the BMO area is defined as the area inside the BMO points, for one B-scan it is represented by the line consisting of green part and magenta part in Figure 5.13A

- the cup area defined between the BMO points intersecting with the ILM (if there is a cup), for one B-scan it is represented by the magenta line in Figure 5.13A
- the rim area is defined as the BMO area - cup area, for one B-scan it is represented by the green line parts in Figure 5.13A
- the BMO distance area is defined by the distance between the BMO points, the entire green line in Figure 5.13A
- BMO-ILM intersection area is defined by the points of perpendicular lines from the BMO intersecting the ILM (blue lines in Figure 5.13A), for one B-scan it is represented by the yellow line in Figure 5.13A
- the total excavation volume defined as the sum of the excavation volume and the cup volume, for one B-scan see Figure 5.13D
- the cup volume is defined as the region of the cup, for one B-scan see Figure 5.13E
- the excavation volume is defined by the volume outside the ILM and having as upper bound the BMO-ILM intersecting area, for one B-scan see Figure 5.13F
- the ILM volume defined as the volume between ILM and the perpendicular lines from BMO intersecting the ILM (blue lines in Figure 5.13A), for one B-scan see Figure 5.13G

5.3 Validation

We also tested how reliable the ONH volume detection performs. Intra-session reliability was determined in ten eyes of HC in three repeated measurements. ICC was 0.964 (95% CI: = $[0.903, 0.990]$). Inter-session reliability was determined by longitudinal analysis of 30 eyes of HC in three measurements including baseline, one-year and two-year follow-up examinations. ICC was 0.976 (95% CI: = $[0.956, 0.987]$). Detailed results are presented in [Kadas et al., 2015].

5.4 Results in a clinical study

In order to analyze the algorithm capability in correctly detecting the BMO points and ONH center in different ONH conditions, we have included 36 HC and 213 patients with neurological

TABLE 5.1: Demographic overview of patients and HC. SD = standard deviation.

			Patients	HC
Subjects	No.		213	36
Eyes	No.		426	72
Gender	No.	male	63	14
		female	150	22
Age	Mean (±SD)		41 (±11)	39 (±11)
Disease type	No.	CIS	23	
		RRMS	92	
		SPMS	14	
		NMOSD	33	
		IIH	15	
ON	No. of eyes	CIS	22	
		RRMS	73	
		SPMS	18	
		NMOSD	0	
		IIH	0	

disorders (MS (with subtypes), NMOSD and IIH). An overview of the included cohort is illustrated in Table 5.1. Our method was able to reliably determine BMO points and ONH centroid and ONHV estimations were robust in both atrophic and swollen ONH condition. Figures 5.14, 5.15, 5.16 and 5.17 illustrate the ILM surface of different examples of ONH, with the BMO points and the ONH center as seen in our data.

The algorithm failed in 6% of all 426 eyes due to poor signal to noise ratio or due to unpropitious position of blood vessels near the ONH region. We also investigated how well ONHV correlates to OCT standard measurements, i.e. RNFL thickness and GCIPL thickness, using the GEE analysis. We have found that ONHV correlates with RNFL thickness and GCIPL thickness in MS, NMOSD but not in HC see Table 5.2, [Kadas et al., 2015]. In differentiation between ON and non ON eyes, ONHV performed similarly to RNFL thickness and GCIPL thickness, [Kadas et al., 2015]. RNFL thickness was measured using a 3.4 mm circular scan around the ONH with the device's standard protocol and segmentation algorithm with activated eye tracker and the maximum number of averaging frames was tried to be achieved. GCIPL was derived by semi-automated segmentation from macula centered scan comprising 61 slices (B-scans) focusing the fovea centralis with a scanning angle of 30° × 25° and a resolution of 768 A-scans per B-scan were acquired. The statistical analysis was performed with R version 3.1.2. Statistical

TABLE 5.2: Correlations between ONHV and OCT standard measurements in patients and in HC

	ONHV			
	HC		Patients	
	B	p	B	p
RNFL thickness	0.00524	0.112	0.012506	p<0.001
GCIPL thickness	0.00942	0.073	0.02280	p<0.001

significance was established at $p < 0.05$ in all analyses. For all group comparison and correlation of OCT parameters we performed GEE analyses with working correlation matrix structure “exchangeable” accounting for inter-eye/intra-patient dependencies.

Development environment Algorithm development was done using Matlab R2011A with Spline library (Mathworks, Germany) on Mac OS X (Apple, Cupertino, CA, USA, Intel Core i5, 4GB memory). The algorithm requires 2.5 to 3 minutes for the whole computation, depending on the sub-volume size.

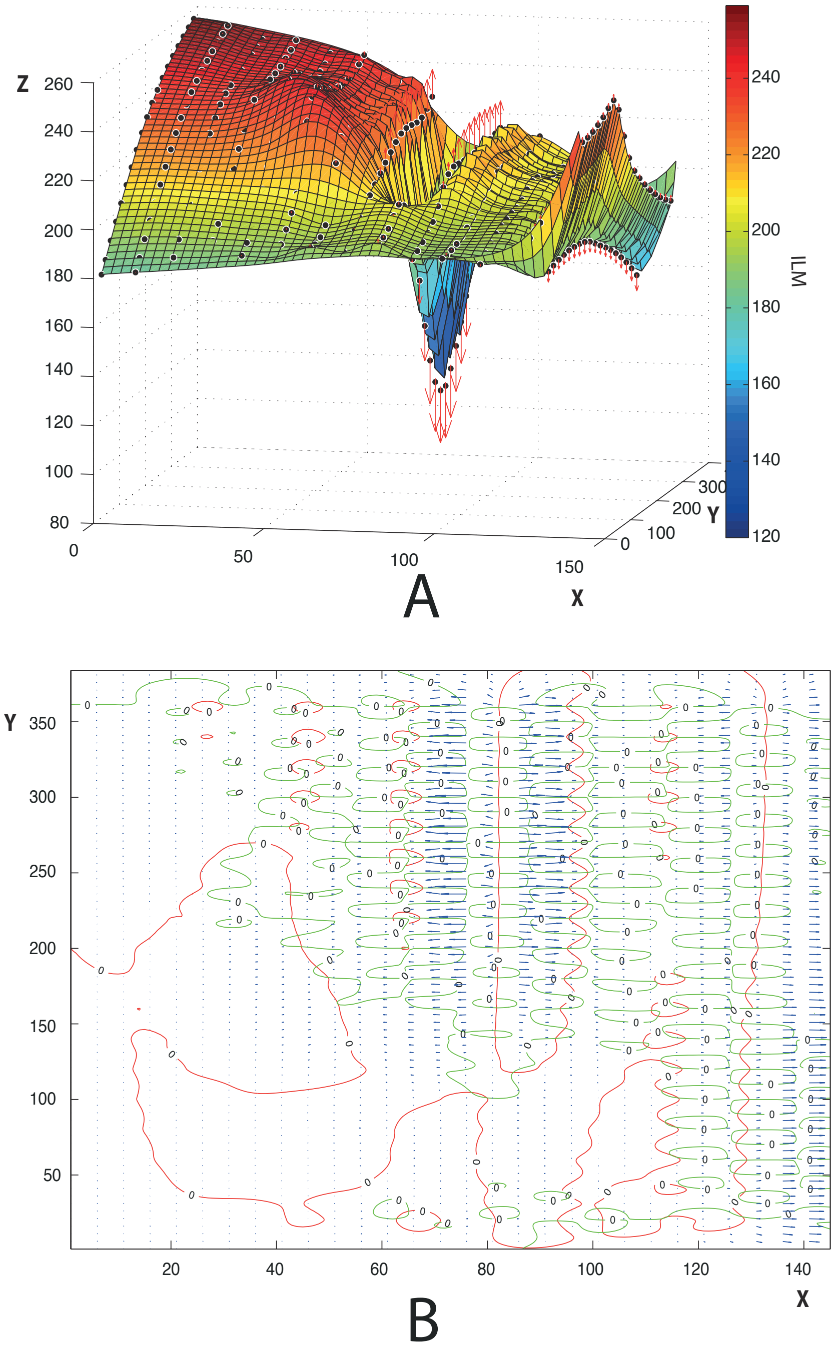

FIGURE 5.4: A. Initial TPS fitted to the data with motion artifacts seen in Figure 5.3. B. Contours at 0 level of the derivatives of the initial TPS with the gradient vectors. To illustrate how well TPS performs, the exact values (as black balls) as well as each arrow leading from a smoothed value to the corresponding noisy value are depicted in A.

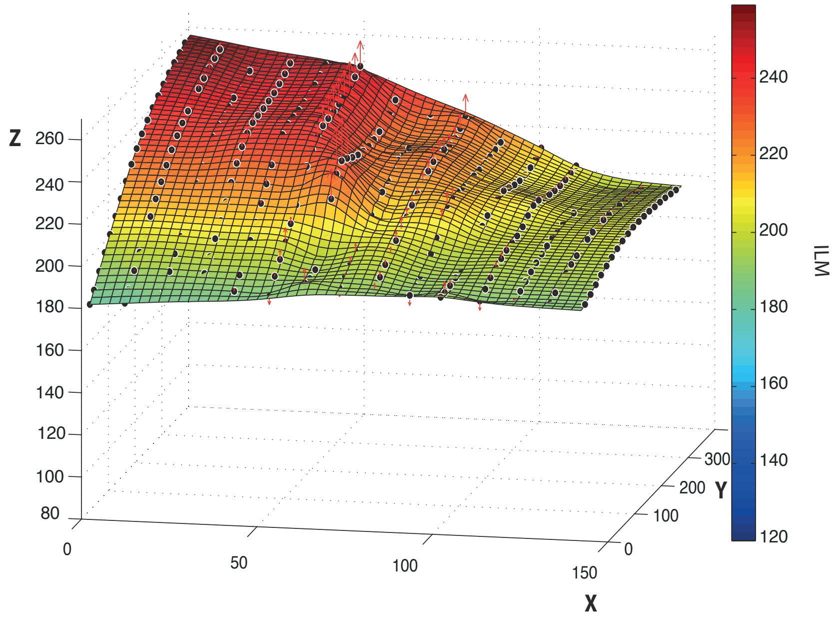

FIGURE 5.5: Second stage TPS result. To illustrate how well TPS performs, the exact values (as black balls) as well as each arrow leading from a smoothed value to the corresponding noisy value are depicted.

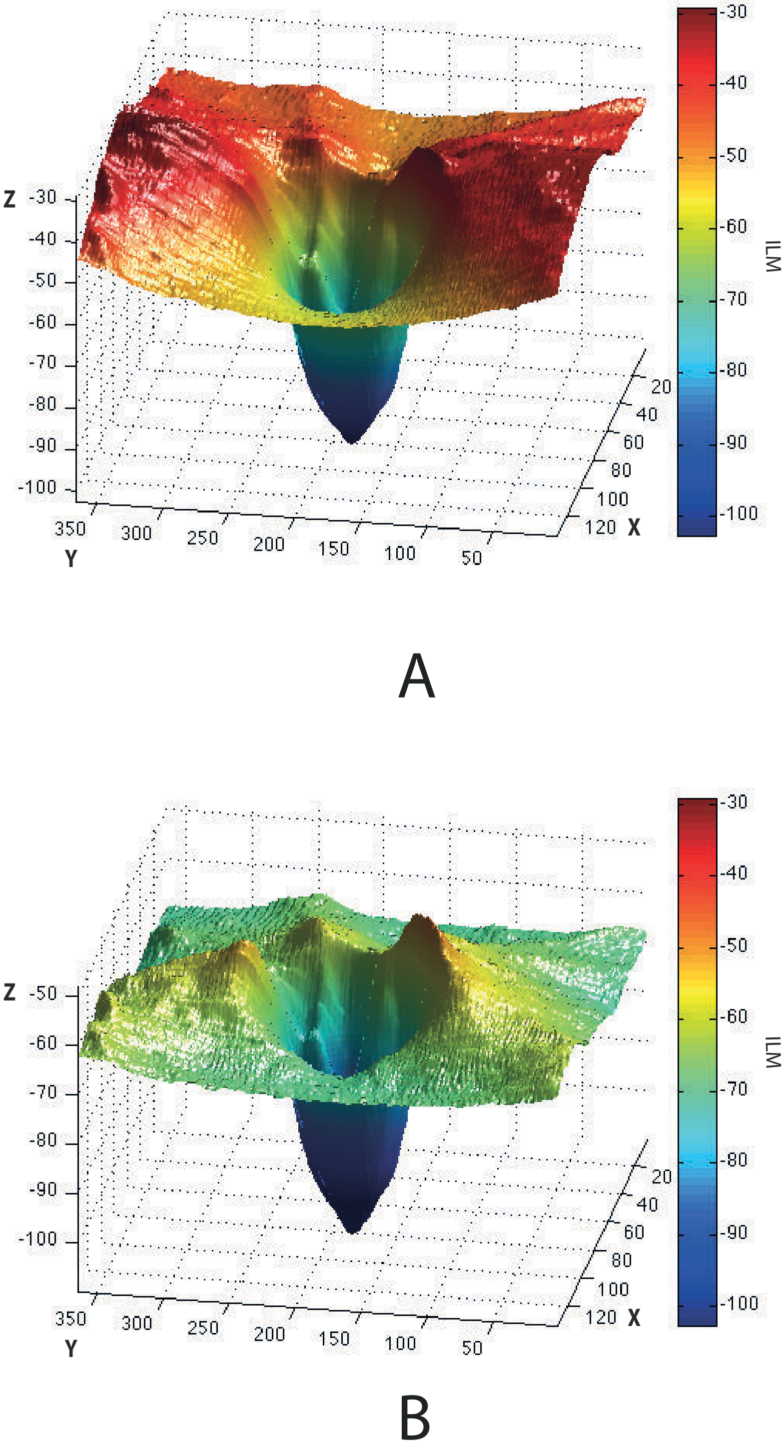

FIGURE 5.6: A. ILM surface before alignment. B. ILM surface after alignment.

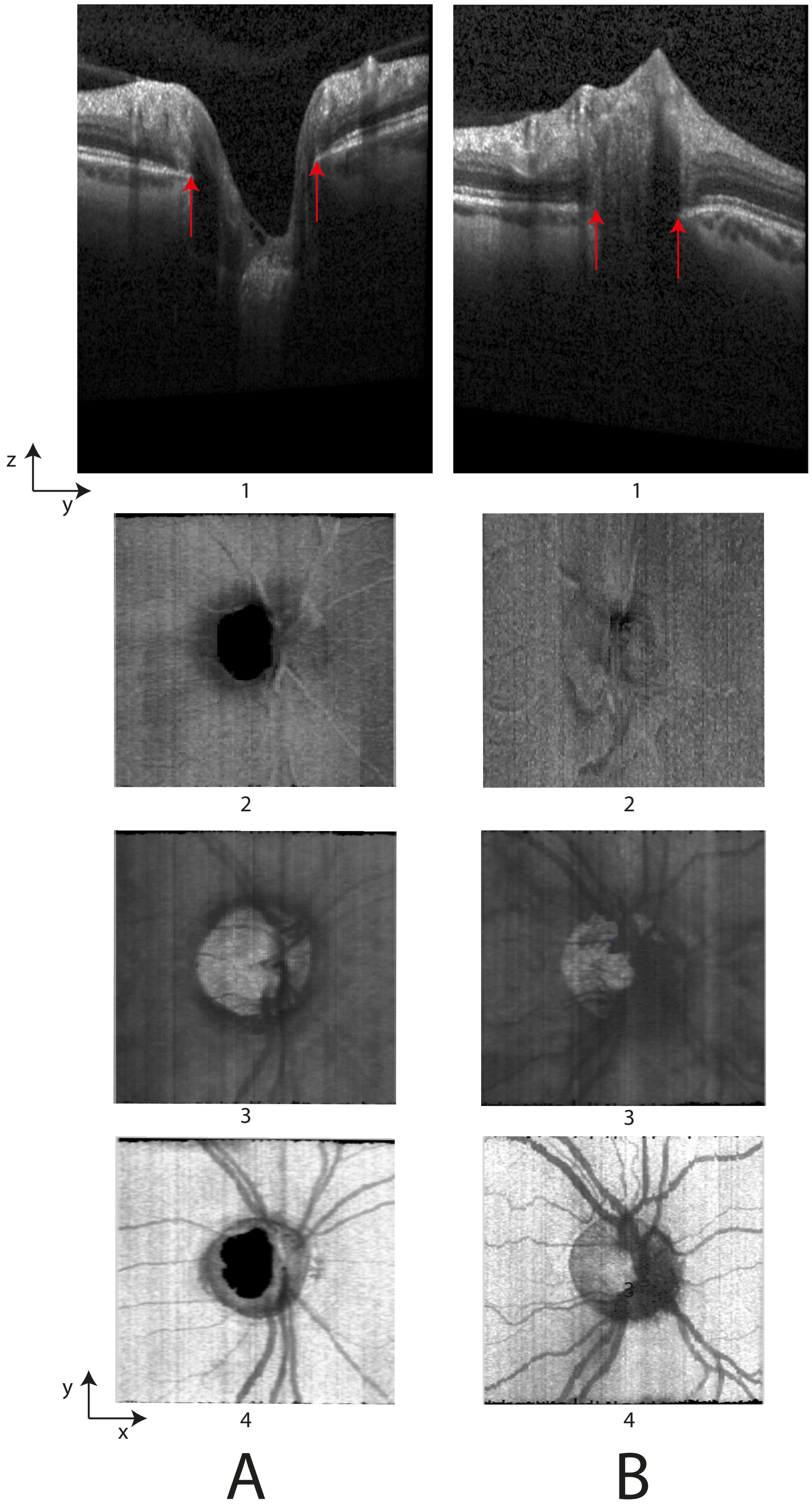

FIGURE 5.7: Examples of different ONHs with their C-mode images. A.1. and B.1. B-scans from 3D volumes, red arrows represent the BMO points. A.2-4. B.2-4 C-mode images from different y positions in the volume, from left to right projections from a thin layer: 2. at the ILM, 3. bellow the RPE, 4. at the RPE.

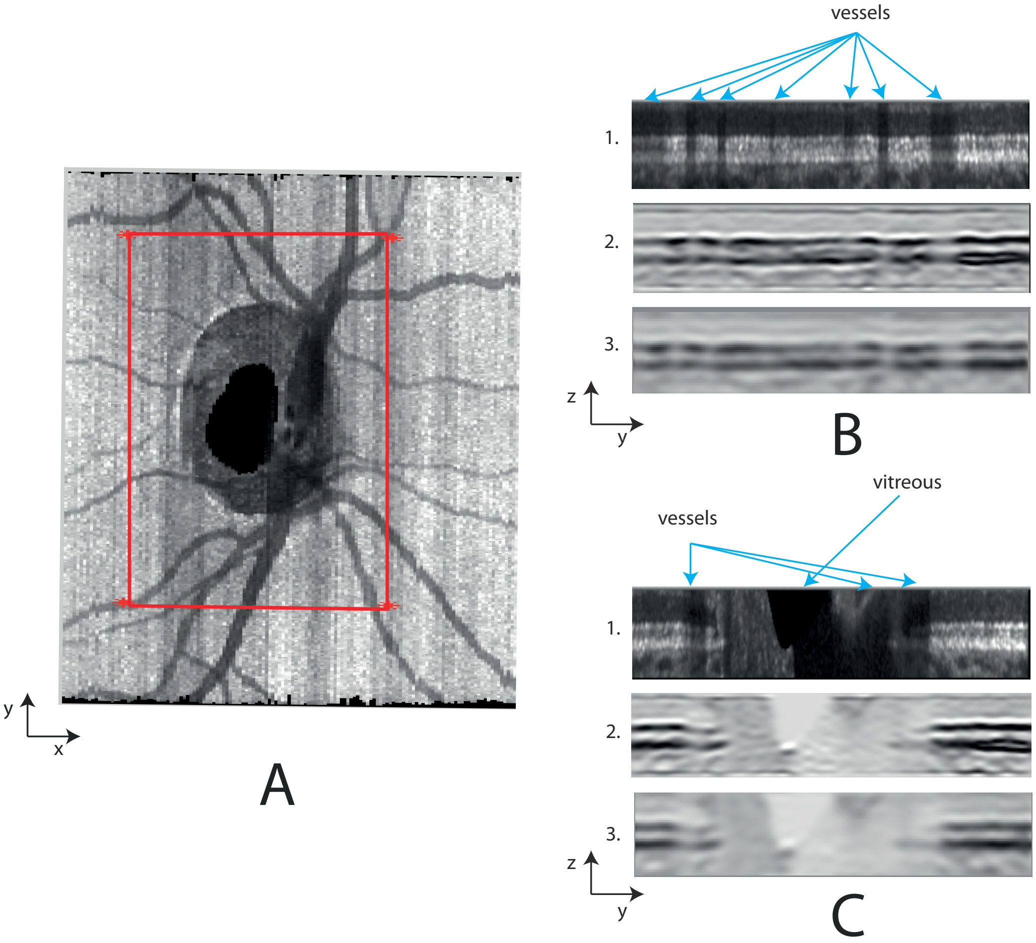

FIGURE 5.8: A. C-mode image with the region used for applying the volume reduction inside the red rectangle. B. and C. Two B-scans from the reduced volume, B. outside the ONH region, C through the ONH. B.1., C.1. represent the original gray values, B.2., C.2. represent the values obtained after applying a wavelet filter, B.3., C.3. represent the values after RPE enhancement.

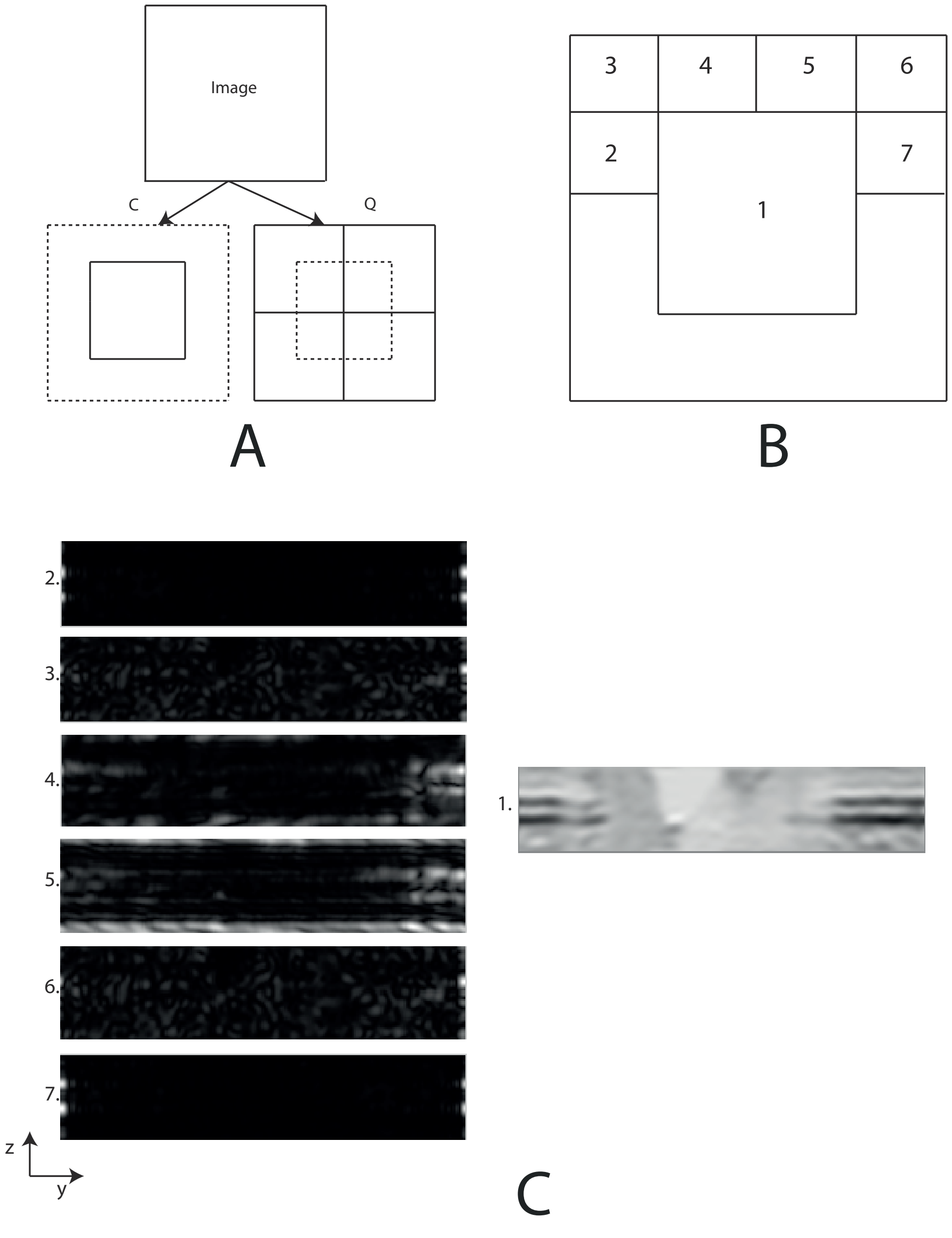

FIGURE 5.9: A. Primitive tessellation operators, center and quadrant. B. OP of level 1. C. 1-7 example of B-scan after applying SMF. Each number corresponds to the OP numbers in B.

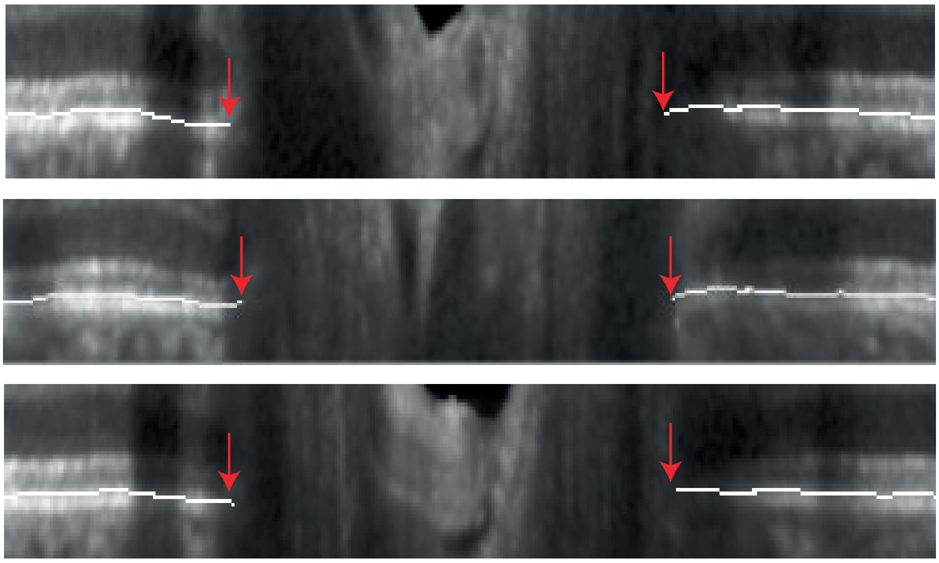

FIGURE 5.10: B-scan from original sub-volume with BMO points (red arrows), and final RPE detected surface.

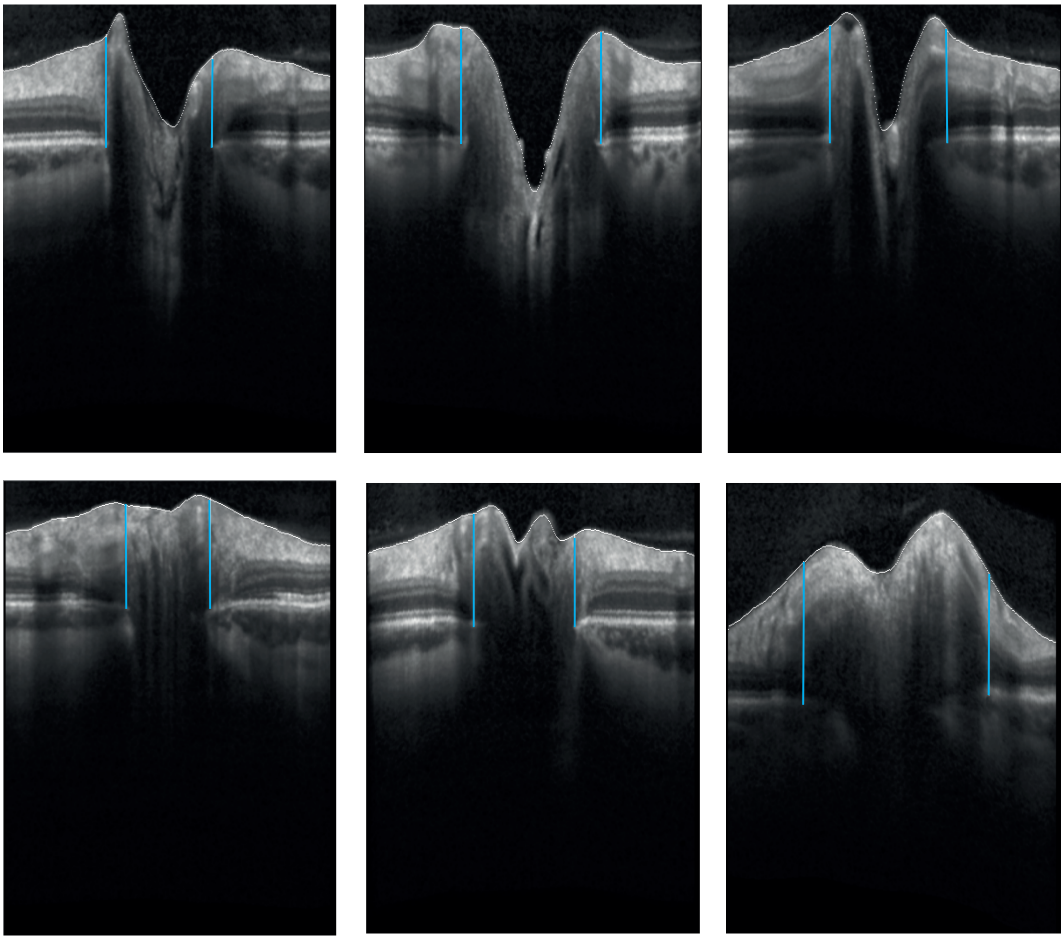

FIGURE 5.11: B-scans with ILM (white line), and two perpendicular lines from the detected BMO points to the ILM (blue lines).

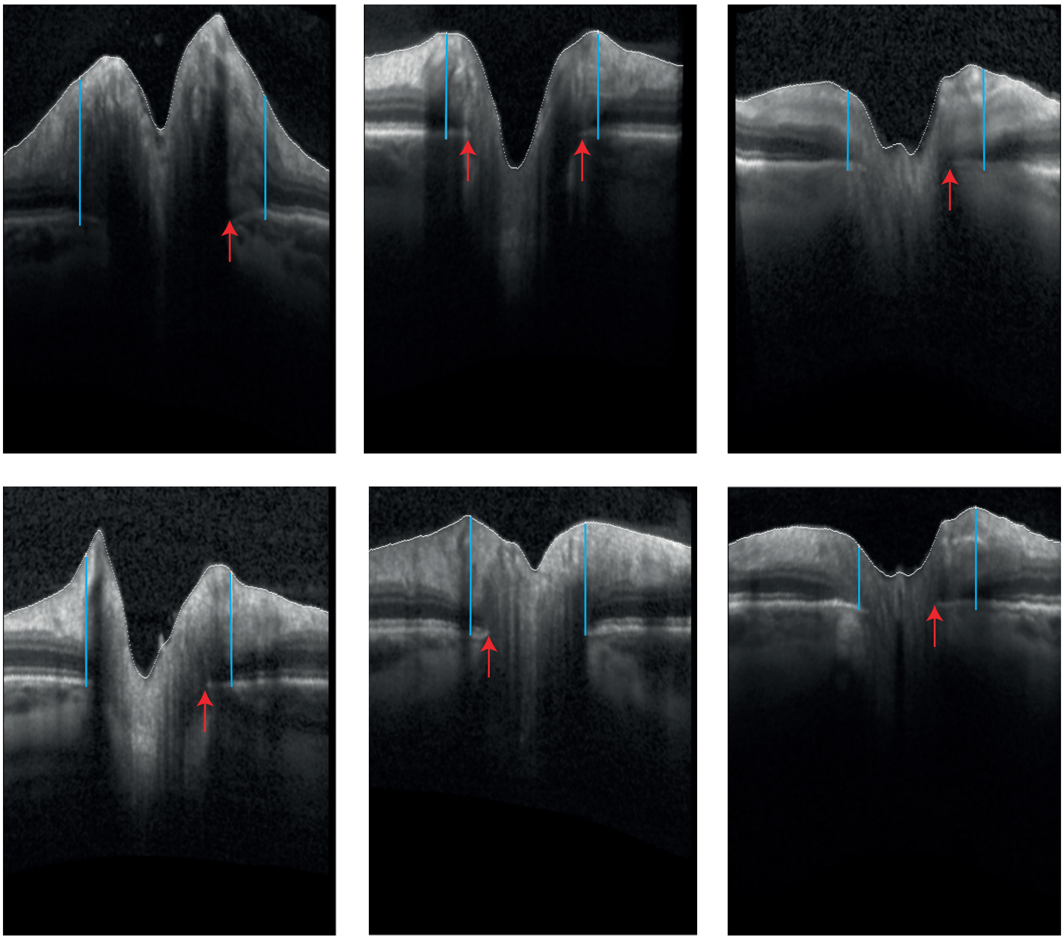

FIGURE 5.12: B-scans with ILM (white line), and two perpendicular lines from the detected BMO points to the ILM (blue lines). Red arrows show the correct position of the BMO points, that were misclassified by the algorithm.

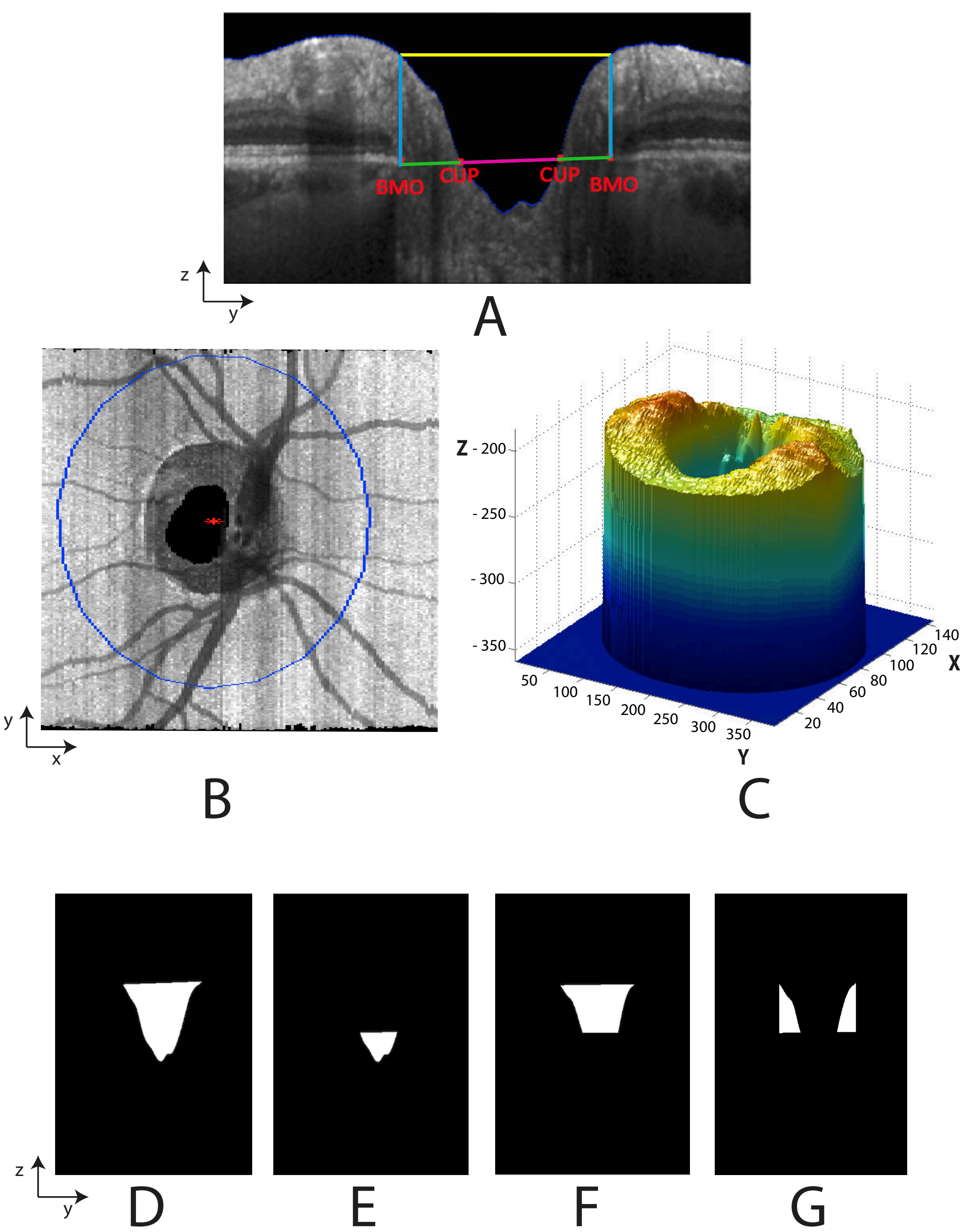

FIGURE 5.13: A. B-scan with BMO points and cup points, red crosses; the lines define regions that will be used in computing D-G. B. C-mode image with ONH center, red cross, blue circle represents the area of the cylinder. C. The ONH volume between ILM and RPE lower boundary inside a cylinder with a radius of 1.7 mm centered on the ONH. D. B-scan with the region used for the computation of the total excavation volume defined as the sum of the excavation volume and the cup volume. E. B-scan with the region used for the computation of the cup volume. F. B-scan with the region used for the computation of the excavation volume.

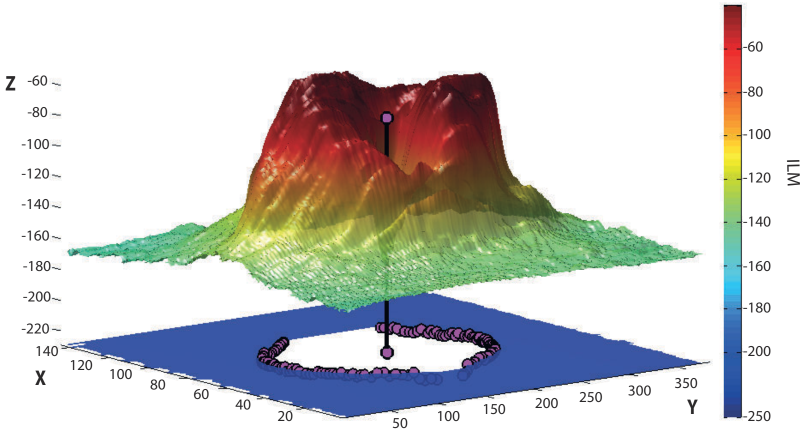

FIGURE 5.14: The surface of the ILM is shown in case of a swollen ONH with BMO points and ONH center detected by the BMO points detection algorithm in magenta.

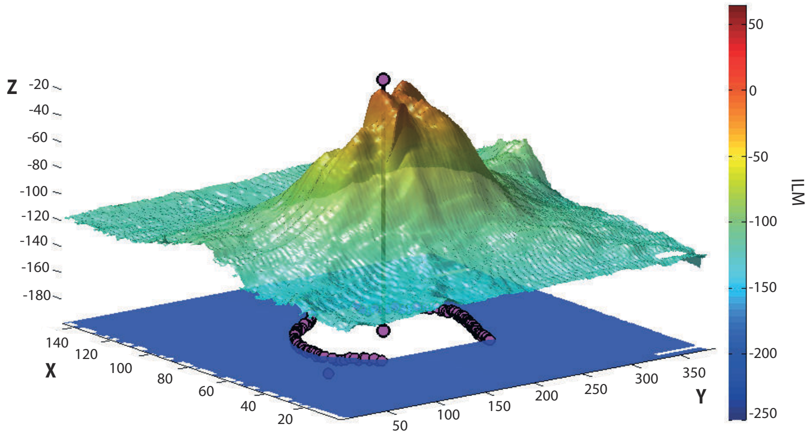

FIGURE 5.15: The surface of the ILM is shown in case of an ONH with no cup with BMO points and ONH center detected by the BMO points detection algorithm in magenta.

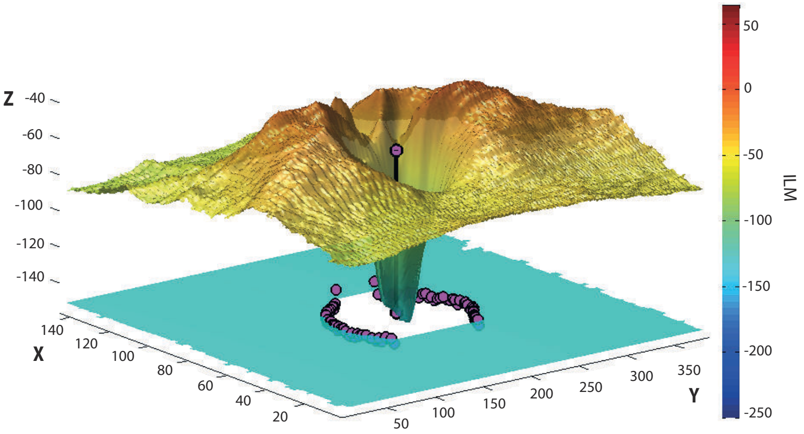

FIGURE 5.16: The surface of the ILM is shown in case of an ONH with small cup with BMO points and ONH center detected by the BMO points detection algorithm in magenta.

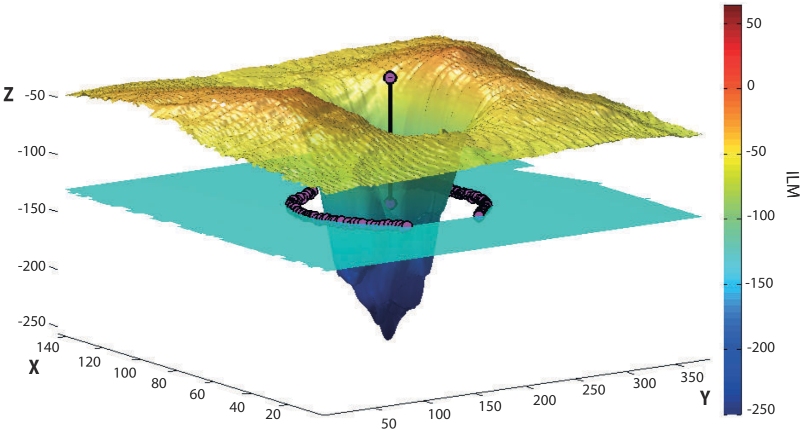

FIGURE 5.17: The surface of the ILM is shown in case of an ONH with large cup with BMO points and ONH center detected by the BMO points detection algorithm in magenta.

Chapter 6

Discussion

6.1 Semi-automated tool for detection of blood vessel inner and outer diameter in cSLO images

We have presented a semi-automated method to segment the inner and outer diameter of retinal blood vessels in cSLO images. The main contribution of this algorithm consists in the integration of the central reflex light in a DG model. Compared to the MF response based methods developed for the fundus photographs that use a steerable Gaussian profile model, our approach was able to emphasize the vessels presenting this characteristic of the central reflex, leading to a strong filter response of the vessel's entire diameter. Although developed only for the purpose of quantifying the vessels in a region in the close vicinity of the standard peripapillary ring of 3,4 mm in diameter, mainly because blood vessels at this region present less branching and have a large diameter, our method has shown very good results, with an excellent ICC, and an accurate segmentation of the outer diameter. The falsely detected outer boundaries occurred especially in the case of low contrast small vessel labeled as unknown. In the case of the inner boundary the detection failed where the contrast between the outer boundary and the inner one was too low to create a strong response in the vessel profile. We did not further investigate this method for the detection of the entire retinal vasculature because of the low response of our developed filter in small vessels, where the central reflex is no longer present. In those cases the MF approach would have provided a better result. To distinguish between the two cases, with and without central reflex, one could apply an error estimation in fitting the DG profile in a small window along the vessels. This would however increase the computational cost. The proposed algorithm showed a substantial potential in clinical applications, as described in the study presented in Subsection 3.2.3, in which we investigated the CCSVI hypothesis in the retinal vasculature. Our findings object a venous congestion as a possible disease mechanism in MS since one would expect larger, dammed veins rather than smaller veins, as it was the case in our study.

6.2 Detection of the entire retinal vasculature in cSLO images

We have presented three approaches to detect curvilinear structures, and applied these approaches in the detection of the entire retinal vessel network in cSLO images. The first approach adapted the proposed 2D Morlet filtering by [Soares et al., 2006] used for vessel segmentation in fundus photographs. Although providing good results in detecting the vessel boundaries and small vessels, it also shows responses arising from other linear structures, as cSLO, unlike fundus photographs, present certain texture features, that simulates the course of the ganglion cell axons. Also in this approach we have to account again for the central reflex that has the effect that large vessels can be misleadingly treated by the algorithm as two parallel smaller ones. To detect the large vessel inner and out diameter we made use of the second eigenvector of the Hessian matrix at each pixel, at large scales which in our case were set between 3 and 7 pixels. Notice that this computation had the effect of smoothing the vessel boundary giving a much larger response than the boundary observed in the original image. Thus, although we apply an extra normalization factor relative to the approximation of the diameter (2*scale) the response still slightly over-estimates the boundary. Further investigations will be needed to establish the influence on the vessel centerline and crossing points detection of this over-estimation, especially in the context of registration of follow-up images. In our second approach we reformulate the *vesselness* filter defined by [Frangi et al., 1998]. This method was developed for computer tomography angiography images, but it is applied in a wide variety of vessel segmentation algorithms and detection of tubular objects in different modalities. Despite being one of the most frequently used methods for detecting tubular structure in medical imaging as noted by [Olabarriaga et al., 2003], it is well known that the major drawback consists in the low response at vessel junctions. Our *vesselness* measure is able to overcome this by imposing a measure that incorporates the vessel direction. This has the advantage that it shifts the focus from a local point to a more global one defined by the vessel segment direction. Although it detects less small vessels compared to our first approach, it has the advantage of presenting less misidentified structures. Our last approach uses the OOF filter response introduced by [Law and Chung, 2008] to derive a measure based on the eigenvalues but also on the eigenvectors of the OOF. This extension of the OOF filter aids the *vesselness* defined, to provide a strong response inside the vessel as well as on the boundaries, and a low response at the non-vessel (background) areas, unlike the OOF filter that focuses only on detecting the centerline of the vessel. Compared to the other two approaches we notice that small vessels that have a weak contrast compared to the background are not detected. Nevertheless this approach is capable to model the vessel profile especially in vessels with a strong curvature and to distinguish between close vessels, because unlike the Hessian template, the OOF one is localized around the vessel boundary.

6.3 RPE lower boundary segmentation for ONH volume computation

We have developed an automatic segmentation approach for computing ONH volume and ONH maximum height from 3D SDOCT scans that is robust and applicable in healthy, but most importantly in swelled ONH. The main achievement of this method is the robust detection of the RPE lower boundary. In the case of extreme swelling like in IIH data, RPE detection can become extremely challenging. To our knowledge, direct ONH quantification as presented in our approach [Kadas et al., 2012a] has never been investigated in this special case at the time of publication. Our algorithm does not rely on the 3D contextual information, but rather performs the computation using only the 2D information from single B-scans. Our decision in taking the 2D approach was based on the observation that information about the RPE lower boundary can be missing especially in the cases of severe swelling in several B-scans, but also on the fact that there is a strong variation in RPE gray values between B-scans due to poor light penetration through the swelling, which would cause methods and feature definitions based on intensity values to fail. However we successfully integrated our algorithm in a 3D setting, for the BMO points detection method, see Chapter 5. From the clinical application point of view, quantifying ONH edema in IIH is potentially important for diagnosis and especially for monitoring progression and treatment effectiveness. Our algorithm provided very good results when tested in a clinical study in IIH patients as well as HC and was able to detect pronounced and significant differences between the groups [Kaufhold et al., 2012]. The discriminatory ability between untreated patients and HC was very good, with only very few patients and controls overlapping. In contrast, control standard measurements using RNFL thickness did not show differences between the groups.

These findings present several possibilities for using quantified ONH volume in practice. OCT could aid in diagnosis of IIH, providing an easy tool to quantify ONH swelling in patients with unclear symptoms. Automated 3D ONH assessment could also be useful for monitoring therapeutic effects of IIH treatment or for quantifying disease progression.

Furthermore, our algorithm was applied in another important clinical study [Albrecht et al., 2015] who investigated whether patients with moyamoya angiopathy without obvious retinal pathologies such as retinal infarction or the congenital morning glory anomaly may have subtle subclinical retinal changes. The main finding in the investigation was a pronounced reduction of the ONHV (computed with our algorithm) in moyamoya angiopathy compared with HC. These results were published in *Neurology* one of the most important neurology journals.

6.4 BMO points detection for ONH center and ONH volume computation

We presented a fully automated BMO points detection algorithm that is tailored to detect ONH features in very heterogeneous data in neurological disorders. As described in Section 5, we first have to account in our algorithm for different artifacts that are mostly caused by the difficulties in the acquisition process for certain patients with severe degree of disease. To this end we developed criteria to discard erroneous data, in order to use as many datasets as possible.

Also we reformulated the TPS fitting method, by using a two-stage approach which removes grid points that arise from motion artifacts in consecutive B-scans. TPS was introduced as a preprocessing step for a 3D intraretinal segmentation algorithm by [Garvin et al., 2008]. In their work, a 3D segmentation-based method that corrects motion artifacts by re-aligning the columns of the image with respect to a smooth “reference” plane is described. This reference plane is constructed by fitting a smoothing TPS to a surface segmented in a lower resolution. The small number of control points and the large regularization term used in the spline-fit process reduces the dependence on the segmentation result, but the spline is not able to model the fast variations seen along the z direction (the orientation axis of an 3D OCT scan are shown in Figure 2.13 B). A smaller regularization term would have provided a closer fit to the control points, but this would have increased the dependence of the artifact correction on the segmentation result. [Bhavna et al., 2014] improved the method presented by [Garvin et al., 2008] by addressing the characteristic artifacts along each axis separately while retaining the overall 3D context. This is done by incorporating *a priori* information regarding the different artifacts seen along these two axial directions and correcting them using dual- stage thin-plate splines fitted to a segmented surface. However, the application of these methods is restricted by the availability of the orthogonal scans, which are not typically acquired clinically.

In our approach we used in the second stage a lager regularization term λ than in the previous mentioned methods. Although a small regularization term and a coarser grid definition would have reduced the sensitivity of the fitting to the displacement in the B-scans, it would have also caused the resulting fitted surface to deviate form the natural scleral curvature of the retina, inducing a surface that is no longer directly related to the analyzed data.

Note that previously developed methods presented in Section 5.1 focus on detecting the BMO points, or the optic disc, in glaucoma patients. This disease, depending on the degree of the atrophy of the ONH, is characterized by a strong excavation of the ONH which extends beyond the RPE surface. This important aspect was incorporated in all the previously approaches in different ways. [Hu et al., 2010a] used a projection image from a thin layer at the RPE/BM complex and applied a graph based approach to segment the BMO and cup from the unwrapped image in polar coordinates. Although in this approach, cases with shallow cup were addressed, by switching from a two-boundary to the single-boundary graph search method, our data contained numerous examples of cases where BMO was visible in the B-scan but not on the projected image. This would cause the single-boundary search to detect an underestimated disc margin.

In another approach [Lee et al., 2010] incorporated the aspect of strong excavation of the ONH for the calculation of local features for the cup and rim classification in OCT volume in a k-NN classifier model. These features were not reproducible with our data.

[Bhavna et al., 2014] combined a graph-theoretic approach in the 3D SDOCT and a 2D projection image (C-mode image) from retinal layers by considering the BMO as a “hole” embedded with multiple surrounding surfaces in order to detect the BMO points. This approach is based on the same assumption of the existence of a clear defined cup.

Therefore caution should be taken when using projection images to detect the BMO as these, as seen in our investigation, might not always provide the full information contained in the 3D OCT. This aspect is similar to results described by [Reis et al., 2012] for fundus photographs and 3D OCT data.

Thus, in contrast to the above mentioned methods, which either use only information from 2D images, or create a 2D projection image (C-mode image) from the 3D volume, our algorithm is able to detect the BMO points in the 3D volume directly. The method presented in Chapter 5 does not require the segmentation of all the retinal layers, which often fails under the challenge of retinal pathologies. It only makes use of the ILM, which separates the retina from the vitreous and by such presents less difficulty in correctly detecting it, and the lower boundary of the RPE, which was proven to be a stable parameter even in the case of pathological images [Strouthidis et al., 2009a].

Because we detect the BMO points in the flattened volume, the Border tissue does not interfere in the extraction of their correct position as mentioned in the method proposed by [Bhavna et al., 2014].

Also note that we considerably reduce the computational costs, by subtracting a sub-volume from the original 3D data based on an ellipse fitted to the ONH region detected at a very early stage of our algorithm.

The last step in our BMO points detection algorithm consists of a modified *grow-cut* approach. It is known that the algorithm proposed by [Vezhnevets and Konouchine, 2005] converges slowly, especially when applied to 3D medical images because it traces through the entire image domain at each iteration [Zhu et al., 2014]. Compared to this approach, we were able to reduce the computational time by using *a priori* information about the positions of voxels belonging to the RPE, as well as by redefining the strength function to depend on the distance of unknown labeled voxels to the RPE voxels. Also we discarded voxels that were unlikely to belong to the RPE from the iteration. An improvement to our method would be achieved by considering an approximated formulation of the updating process presented in [Zhu et al., 2014] that can be solved very efficiently with the Dijkstra algorithm.

A major drawback of our method is the presence of blood vessels in the ONH region. Although we are able to correctly detect BMO in several cases where the shadows created by the blood vessel occur, by incorporating contextual textural feature in a 3D *grow-cut* approach, there are still some cases in which the detection fails.

Chapter 7

Conclusion and Outlook

The overarching theme of the work presented here has been the development of automated methods to segment and quantify structures in the retina from data of patients with neurological disorders as well as HC. The methods could provide clinicians additional parameters for further analysis and a better understanding of the disease course. The automated detection of structures in these images is, however, far from trivial as the images are prone to speckle noise and often show large artifacts caused by motion and acquisition errors. The presence of disease can also cause low contrast in these images, making it difficult to identify structures of interest. We have presented four algorithms to achieve this goal, and described their capabilities of overcoming the challenges described in our data.

The semi-automated vessel boundary detection algorithm describes a method to extract vessel inner and outer boundary in cSLO images. Although it detects these parameters only locally at the close vicinity of the peripapillary ring, it is able to address the central reflex present in cSLO images, by defining an appropriate profile model of the vessel. The proposed algorithm showed a substantial potential in clinical applications, as presented in the clinical study with MS and CIS data. To further investigate vessel characteristics in neurological disorders, by comprising several other parameters like vessel distribution, fractal dimension, tortuosity, features often used for detection of eye diseases, the segmentation of the whole blood vessel network would be required. This aspect was not further addressed in our work, because the initial study conducted showed no significant differences between MS patients and HC. However, in our second algorithm we propose three different approaches to extract the entire vasculature. The main motivation for this analysis arises from the need of detecting landmarks for the registration of different ONH scans. Although still in a developing phase, we have shown the capabilities of the proposed methods in detecting the main retinal vessel branches. The *vesselness* response developed in the second, new Hessian based *vesselness*, and third approach, the extended OOF based *vesselness*, could be further used in a fast marching setting, or minimal path method, for a better vasculature segmentation result. The RPE lower boundary detection algorithm presents a robust and accurate method to detect this boundary in 3D SDOCT scans centered on the ONH. The RPE boundary is used as a reference surface for further ONH volume computation. Although it uses 2D information only, this method has been shown to provide reliable results in HC, but most importantly in difficult scans that present different degrees of ONH swelling. In these special cases, methods developed for HC or patients with glaucoma occasionally fail to properly detect this boundary. The development of our algorithm focuses now on studying follow-up data from IIH patients and further improving the algorithm's reliability in repeated measurements, also in the analysis of the special case of ONH in the acute phase of ON, a highly interesting topic for its potential clinical application, also presenting swelling as its hallmark. The BMO points detection algorithm extends our RPE lower boundary extraction approach, in order to segment BMO points, for ONH center and volume computation directly from the 3D volume. We have presented several new approaches to achieve this goal. Our two stage TPS fitting is able to account for strong motion artifacts. In addition the incorporation of texture analysis in a 3D grow-cut setting provide our algorithm with the capability of detecting the BMO in most of the cases where vessels in the ONH region obstruct the information of the RPE. The most important aspect of our method is that it does not rely on the C-mode images, but on the 3D information itself. We have shown that our algorithm is able to detect the BMO points in a large variety of data, for atrophic, healthy and swelled ONH. The main disadvantage is represented by the presence of blood vessels. To address this issue we intend to use the information from the retinal vasculature in combination with the 3D volume to separately address the RPE region affected by the presence of vessels. One important future extension of this work will be the identification of appropriate volumetric features that can potentially help in differentiating between disorders, which the present work does not address. The best features may very well be "regional" in nature (quadrant volumes, and regional shape parameters). Importantly, the true 3D segmentation approach proposed in this work provides the flexibility to easily compute such regional volumetric features for use in future studies, as seen from the parameters already derived.

We plan to further develop tools that enable us to determine morphometrics and their changes in the ONH for HC, and patients with different neurological diseases. To achieve this goal we want to establishes one-to-one correspondence between the ONH surfaces for different time points within the data of the same subject. This is an important step in understanding first, the variation of the ONH shape associated with age and gender, in the group of HC, unknown to the present moment. Also, in a later stage, it would provide a modality of understanding and monitoring disease progression in patients. To this end we plan to extend the BMO points detection algorithm for ONH center and ONH volume computation presented in Chapter 5 to create a 3D shape model of the ONH from 3D SDOCT data. Also we want to further develop the entire vasculature algorithm presented in Section 3.3 to establish to best approach to extract vessel crossings as landmarks for registration purposes. On basis of this 3D template we plan to determine first, changes in the whole 3D measured volume, then identify specific topographic features and local shape landmarks on the surface that represents the upper plane of the volume. This will enable us to reveal clinically valuable information on the shape variation of the ONH.

In conclusion, our methods have proven their clinical applicability. The retinal structures detected in this work have the potential of providing better insights for the clinicians in the analysis of several neurological disorders.

Bibliography

M.D. Abràmoff, K. Lee, M. Niemeijer, W.L.M. Alward, E.C. Greenlee, M.K. Garvin, M. Sonka, and Y.H. Kwon. Automated segmentation of the cup and rim from spectral domain oct of the optic nerve head. *Investigative Ophthalmology and Visual Science*, 50(12):5778, 2009. doi: 10.1167/iovs.09-3790.

M.D. Abràmoff, M.K. Garvin, and M. Sonka. Retinal imaging and image analysis. *Biomedical Engineering, IEEE Reviews in*, 3:169–208, 2010. ISSN 1937-3333. doi: 10.1109/RBME.2010.2084567.

P. Albrecht, R. Fröhlich, H.-P. Hartung, B.C. Kieseier, and A. Methner. Optical coherence tomography measures axonal loss in multiple sclerosis independently of optic neuritis. *Journal of Neurology*, 254(11):1595–1596, 2007. ISSN 0340-5354. doi: 10.1007/s00415-007-0538-3.

P. Albrecht, C. Blasberg, S. Lukas, M. Ringelstein, A.-K. Müller, J. Harmel, E.M. Kadas, D. Finis, R. Guthoff, O. Aktas, H.-P. Hartung, F. Paul, A.U. Brandt, P. Berlit, A. Methner, and M. Kraemer. Retinal pathology in idiopathic moyamoya angiopathy detected by optical coherence tomography. *Neurology*, 85(6):521–527, 2015. doi: 10.1212/WNL.0000000000001832.

B. Anand-Apte and J.G. Hollyfield. Developmental anatomy of the retinal and choroidal vasculature. In Dean Bok Joseph C. Besharse, editor, *The Retina and Its Disorders*, pages 179–185. Academic Press, 2011.

J.P. Antoine, P. Carrette, R. Murenzi, and P. Piette. Image analysis with two-dimensional continuous wavelet transform. *Signal Processing*, 31(3):241 – 272, 1993.

S. Arseneau and J.R. Cooperstock. An improved representation of junctions through asymmetric tensor diffusion. In G. Bebis, R. Boyle, B. Parvin, D. Koracin, P. Remagnino, A. Nefian,

G. Meenakshisundaram, V. Pascucci, J. Zara, J. Molineros, H. Theisel, and T. Malzbender, editors, *Advances in Visual Computing*, volume 4291 of *Lecture Notes in Computer Science*, pages 363–372. Springer Berlin Heidelberg, 2006. ISBN 978-3-540-48628-2. doi: 10.1007/11919476_37.

L.J. Balcer. Optic neuritis. *New England Journal of Medicine*, 354(12):1273–1280, 2006. doi: 10.1056/NEJMcp053247. PMID: 16554529.

P. Bankhead, C.N. Scholfield, J.G. McGeown, and T.M. Curtis. Fast retinal vessel detection and measurement using wavelets and edge location refinement. *PLoS ONE*, 7(3):e32435, 03 2012. doi: 10.1371/journal.pone.0032435.

A.J. Bhavna, M.S. Miri, M.D. Abràmoff, Y.H. Kwon, and M.K. Garvin. Automated 3d segmentation of multiple surfaces with a shared hole: Segmentation of the neural canal opening in sd-oct volumes. In P. Golland, N. Hata, C. Barillot, J. Hornegger, and R. Howe, editors, *Medical Image Computing and Computer-Assisted Intervention – MICCAI 2014*, volume 8673 of *Lecture Notes in Computer Science*, pages 739–746. Springer International Publishing, 2014. ISBN 978-3-319-10403-4. doi: 10.1007/978-3-319-10404-1_92.

J.A. Bhavna, M.D. Abràmoff, M.M. Harper, W. Jeong, E.H. Sohn, Y.H. Kwon, R. Kardon, and M.K. Garvin. A combined machine-learning and graph-based framework for the segmentation of retinal surfaces in sd-oct volumes. *Biomed. Opt. Express*, 4(12):2712–2728, Dec 2013. doi: 10.1364/BOE.4.002712.

F. Bilger. Quantifizierung retinaler Gefäße bei Multipler Sklerose–kann sie einen Beitrag zur Untersuchung venöser Pathologien leisten? 2014.

F.L. Bookstein. Principal warps: thin-plate splines and the decomposition of deformations. *Pattern Analysis and Machine Intelligence, IEEE Transactions on*, 11(6):567–585, Jun 1989. ISSN 0162-8828. doi: 10.1109/34.24792.

T. Brox, J. Weickert, B. Burgeth, and P. Mrázek. Nonlinear structure tensors. *Image and Vision Computing*, 24(1):41–55, Jan. 2006.

A. Budai, R. Bock, A. Maier, J. Hornegger, and G. Michelson. Robust vessel segmentation in fundus images. *International Journal of Biomedical Imaging*, 2013. doi: 10.1155/2013/154860.

S. Chaudhuri, S. Chatterjee, N. Katz, M. Nelson, and M. Goldbaum. Detection of blood vessels in retinal images using two-dimensional matched filters. *IEEE Transactions on Medical Imaging*, 8(3):263–269, Sep 1989. ISSN 0278-0062. doi: 10.1109/42.34715.

J.S. Chiu, X.T. Li, P. Nicholas, and et al. Automatic segmentation of seven retinal layers in sdoct images congruent with expert manual segmentation. *Optic Express 19413*, 18(18), 2010.

A.M. Dascalu, C. Alexandrescu, R. Pascu, R. Ilinca, V. Popescu, R. Ciuluvica, L. Voinea, and C. Celea. Heidelberg retina tomography analysis in optic disks with anatomic particularities. *Journal of Medicine and Life*, 3(4):359–364, 2010.

C.I. Diaconu, D. Conway, R.J. Fox, and A. Rae-Grant. Chronic cerebrospinal venous insufficiency as a cause of multiple sclerosis: Controversy and reality. *Current Treatment Options in Cardiovascular Medicine*, 14(2):203–214, 2012. ISSN 1092-8464. doi: 10.1007/s11936-012-0168-7.

B. Dizdaro, E. Ataer-Cansizoglu, J. Kalpathy-Cramer, K. Keck, M.F. Chiang, and D. Erdogmus. Level sets for retinal vasculature segmentation using seeds from ridges and edges from phase maps. In *Machine Learning for Signal Processing (MLSP), 2012 IEEE International Workshop on*, pages 1–6, Sept 2012. doi: 10.1109/MLSP.2012.6349730.

DMSG. Deutsche Multiple Sklerose Gesellschaft (DMSG), Bundesverband e.v. URL `http://www.dmsg.de`.

Image Science Institute DRIVE. Digital retinal images for vessel extraction. URL `http://www.isi.uu.nl/Research/Databases/DRIVE/`.

L. Florack. The structure of scalar images, 1993.

A.F. Frangi, W.J. Niessen, K.L. Vincken, and M.A. Viergever. Multiscale vessel enhancement filtering. In *Medical Image Computing and Computer Assisted Interventation MICCAI1998*, volume 1496 of *Lecture Notes in Computer Science*, pages 130–137. Springer Berlin Heidelberg, 1998. ISBN 978-3-540-65136-9. doi: 10.1007/BFb0056195.

W.S. Franklin and E.S. Rajan. Computerized screening of diabetic retinopathy employing blood vessel segmentation in retinal images. *Biocybernetics and Biomedical Engineering*, 34(2): 117 – 124, 2014. ISSN 0208-5216. doi: http://dx.doi.org/10.1016/j.bbe.2014.01.004.

A.V.-D. Fuensanta and N. Doble. The human eye and adaptive optics, topics in adaptive optics. In Dr. Bob Tyson, editor, *topics-in-adaptive-optics*. inTech, 2012. ISBN 978-953-307-949-3. doi: 10.5772/31073.

L. Gang, O. Chutatape, and S.M. Krishnan. Detection and measurement of retinal vessels in fundus images using amplitude modified second-order gaussian filter. *IEEE Transactions on Biomedical Engineering*, 49(2):168–172, Feb 2002. ISSN 0018-9294. doi: 10.1109/10.979356.

M.K. Garvin, M.D. Abràmoff, Kardon R., S.R. Russell, Xiaodong Wu, and Sonka M. Intraretinal layer segmentation of macular optical coherence tomography images using optimal 3-d graph search. *Medical Imaging, IEEE Transactions on*, 27(10):1495–1505, Oct 2008. ISSN 0278-0062. doi: 10.1109/TMI.2008.923966.

E. Gibson, Mei Y., M.V. Sarunic, and M.F. Beg. Optic nerve head registration via hemispherical surface and volume registration. *IEEE Transactions on Biomedical Engineering*, 57(10): 2592–2595, 2010. ISSN 0018-9294. doi: 10.1109/TBME.2010.2060337.

Gordon-Lipkin, B. Chodkowski, D.S. Reich, S.A. Smith, M. Pulicken, L.J. Balcer, E.M. Frohman, G. Cutter, and P.A. Calabresi. Retinal nerve fiber layer is associated with brain atrophy in multiple sclerosis. *Neurology*, 69:1603–9, 2007. doi: 10.1212/01.wnl.0000295995.46586.ae.

A.J. Green and B.A.C. Cree. Distinctive retinal nerve fibre layer and vascular changes in neuromyelitis optica following optic neuritis. *Journal of Neurology, Neurosurgery and Psychiatry*, 80(9):1002–1005, 2009. doi: 10.1136/jnnp.2008.166207.

G. Heidary and J.F. Rizzo. Use of optical coherence tomography to evaluate papilledema and pseudopapilledema. *IEEE Trans on Pattern Analysis and Machine Intelligence*, pages 25(5–6):198–205, 2010.

A. Hoover, V. Kouznetsova, and M. Goldbaum. Locating blood vessels in retinal images by piecewise threshold probing of a matched filter response. *IEEE Transactions on Medical Imaging*, 19(3):203–210, March 2000. ISSN 0278-0062. doi: 10.1109/42.845178.

Z. Hu, M.D. Abràmoff, Y.H. Kwon, K. Lee, and M.K. Garvin. Automated segmentation of neural canal opening and optic cup in 3d spectral optical coherence tomography volumes of the optic nerve head. *Investigative Ophthalmology and Visual Science*, 51(11):5708, 2010a. doi: 10.1167/iovs.09-4838.

Z. Hu, D.A. Michael, H.K. Young, and et al. Automated segmentation of neural canal opening and optic cup in 3d spectral optical coherence tomography volumes of the optic nerve head. *Investigative Ophthalmology Visual Science*, 51(11), 2010b.

H. Ishikawa, D.M. Stein, G. Wollstein, S. Beaton, J.G. Fujimoto, and J.S. Schuman. Macular segmentation with optical coherence tomography. *Investigative ophthalmology & visual science*, 46(6):2012, 2005.

X. Juan, I. Hiroshi, W. Gadi, A.B. Richard, K. Larry, E.C. Jamie, A. Mackey David, W.H. Alex, and S.S. Joel. Automated volumetric evaluation of stereoscopic disc photography. *Opt. Express*, 18(11):11347–11359, May 2010. doi: 10.1364/OE.18.011347.

E.M. Kadas, F. Kaufhold, C. Schulz, F. Paul, K. Polthier, and A.U. Brandt. 3d optic nerve head segmentation in idiopathic intracranial hypertension. In *Bildverarbeitung für die Medizin 2012*, Informatik aktuell, pages 262–267. Springer Berlin Heidelberg, 2012a. ISBN 978-3-642-28501-1. doi: 10.1007/978-3-642-28502-8_46.

E.M. Kadas, T. Oberwahrenbrock, H. Zimmermann, S. Papazoglou, F. Paul, K. Polthier, and A.U. Brandt. Quantification of retinal vessels in multiple sclerosis. *ECTRIMS European Committee for treatment and research in multiple sclerosis (ECTRIMS Congress Lyon 2012)*, 2012b.

E.M. Kadas, J. Mikolajczak, W. Lagreze, H. Zimmermann, F. Paul, and A.U. Brandt. Robust optic nerve head analysis based on 3d optical coherence tomography. *NANOS North American Neuro-Ophthalmology society (NANOS Congress San Diego 2015)*, 2015.

F. Kaufhold, E.M. Kadas, C. Schmidt, H. Kunte, J. Hoffmann, H. Zimmermann, T. Oberwahrenbrock, L. Harms, K. Polthier, A.U. Brandt, and F. Paul. Segmentation of the optic disc in 3-d oct scans of the optic nerve head. *PLoS ONE*, 7(5), Jan 2012. doi: 10.1371/journal.pone.0036965.

J.J. Koenderink. The structure of images. *Biological Cybernetics*, 50(5):363–370, 1984. ISSN 0340-1200. doi: 10.1007/BF00336961.

H. Kolb. The organization of the retina and visual system. URL `http://webvision.med.utah.edu/`.

Y. Kotera, Y. Yasuno, M. Hangai, R. Inoue, H. Makita, S. Nakanishi, M. Yamanari, and N. Yoshimura. Comparison of spectral domain optical coherence tomography and color photographic imaging of the optic nerve head in management of glaucoma. *Ophthalmic Surg Lasers Imaging*, 40(3):255–63, 2009.

M.W.K. Law and A.C.S. Chung. Three dimensional curvilinear structure detection using optimally oriented flux. In David Forsyth, Philip Torr, and Andrew Zisserman, editors, *Computer Vision – ECCV 2008*, volume 5305 of *Lecture Notes in Computer Science*, pages 368–382. Springer Berlin Heidelberg, 2008. ISBN 978-3-540-88692-1. doi: 10.1007/978-3-540-88693-8_27.

J.J.G. Leandro, R.M.C. Junior, and H. Jelinek. Blood vessels segmentation in retina: Preliminary assessment of the mathematical morphology and of the wavelet transform techniques. In *Proceedings of the 14th Brazilian Symposium on Computer Graphics and Image Processing*, SIBGRAPI '01, pages 84–90, Washington, DC, USA, 2001. IEEE Computer Society. ISBN 0-7695-1330-1.

B.J. Lee and E.I. Traboulsi. Update on the morning glory disc anomaly. *Ophthalmic Genetics*, 29(2):47–52, 2008. doi: 10.1080/13816810801901876.

K. Lee, M. Niemeijer, M.K. Garvin, Y.H. Kwon, M. Sonka, and M.D. Abràmoff. Segmentation of the optic disc in 3-d oct scans of the optic nerve head. *Medical Imaging, IEEE Transactions on*, 29(1):159–168, Jan 2010. ISSN 0278-0062. doi: 10.1109/TMI.2009.2031324.

K. Lee, M.D. Abràmoff, M.K. Garvin, and M. Sonka. Parallel graph search: application to intraretinal layer segmentation of 3-d macular oct scans. *Proc. SPIE*, 8314:83141H–83141H–7, 2012. doi: 10.1117/12.911606.

T. Lindeberg. Scale-space theory: A basic tool for analyzing structures at different scales. *Journal of Applied Statistics*, 21(1-2):225–270, 1994.

T. Lindeberg. Edge detection and ridge detection with automatic scale selection. *International Journal of Computer Vision*, 30(2):117–156, 1998. ISSN 0920-5691. doi: 10.1023/A:1008097225773.

Massaro M., Thorarensen O., Liu G.T., Maguire A.M., Zimmerman R.A., and Brodsky M.C. Morning glory disc anomaly and moyamoya vessels. *Archives of Ophthalmology*, 116(2): 253–254, 1998.

Sandra M. and Paolo Z. Ccsvi is associated with multiple sclerosis. *Neurological Research*, 34 (8):770–779, 2012. doi: 10.1179/1743132812Y.0000000035. PMID: 22971467.

M.E. Martínez-Pérez, A.D. Hughes, A.V. Stanton, S.A. Thom, A.A. Bharath, and K.H. Parker. Retinal blood vessel segmentation by means of scale-space analysis and region growing. In *Proceedings of the Second International Conference on Medical Image Computing and Computer-Assisted Intervention*, MICCAI '99, pages 90–97, London, UK, UK, 1999. Springer-Verlag. ISBN 3-540-66503-X.

G. Medioni, M.S. Lee, and C.K. Tang. A computational framework for feature extraction and segmentation. *Amsterdam: Elseviers Science*, 2000.

J. Motte, F. Alten, C. Ewering, N. Osada, E.M. Kadas, A.U. Brandt, T. Oberwahrenbrock, C.R. Clemens, N. Eter, F. Paul, and M. Marziniak. Vessel labeling in combined confocal scanning laser ophthalmoscopy and optical coherence tomography images: Criteria for blood vessel discrimination. *PLoS ONE*, 9(9):e102034, 09 2014. doi: 10.1371/journal.pone.0102034.

A.K. Nayan and A.S. Deshpande. Review of retinal blood vessel segmentation techniques. *International Journal of Engineering and Technical Research (IJETR)*, 3(01), Jan 2015.

M. Nielsen, L. Florack, and R. Deriche. Regularization, scale-space, and edge detection filters. In Bernard Buxton and Roberto Cipolla, editors, *Computer Vision — ECCV '96*, volume 1065 of *Lecture Notes in Computer Science*, pages 70–81. Springer Berlin Heidelberg, 1996. ISBN 978-3-540-61123-3. doi: 10.1007/3-540-61123-1_128.

OBEL. Optical and biomedical engineering laboratory. URL `http://obel.ee.uwa.edu.au/`.

T. Oberwahrenbrock, M. Ringelstein, S. Jentschke, K. Deuschle, K. Klumbies, J. Bellmann-Strobl, J. Harmel, K. Ruprecht, S. Schippling, H.-P. Hartung, O. Aktas, A.U. Brandt, and F. Paul. Retinal ganglion cell and inner plexiform layer thinning in clinically isolated syndrome. *Multiple Sclerosis Journal*, 19(14):1887–1895, 2013. doi: 10.1177/1352458513489757.

S.D. Olabarriaga, M. Breeuwer, and W.J. Niessen. Evaluation of hessian-based filters to enhance the axis of coronary arteries in {CT} images. *International Congress Series*, 1256:1191 – 1196, 2003. ISSN 0531-5131. doi: http://dx.doi.org/10.1016/S0531-5131(03)00307-8. {CARS} 2003. Computer Assisted Radiology and Surgery. Proceedings of the 17th International Congress and Exhibition.

N. Otsu. A threshold selection method from gray level histograms. *Trans. Systems, Man and Cybernetics*, 9:62–66, mar 1979.

P. Perona and J. Malik. Scale-space and edge detection using anisotropic diffusion. *Pattern Analysis and Machine Intelligence, IEEE Transactions on*, 12(7):629–639, Jul 1990. ISSN 0162-8828. doi: 10.1109/34.56205.

A. Petzold, J.F. de Boer, S. Schippling, P. Vermersch, R. Kardon, A. Green, P.A. Calabresi, and C. Polman. Optical coherence tomography in multiple sclerosis: a systematic review and meta-analysis. *The Lancet Neurology*, 9(9):921–932, 2010. doi: 10.1002/ana.22005.

M.J.D. Powell. A thin plate spline method for mapping curves into curves in two dimensions. *Computational Techniques and Applications: CTAC95, RL May and AK Easton (Eds.), World Scientific: Singapore*, pages 43–57, 1996.

D. Purves, G.J. Augustine, and D. Fitzpatrick. *Neuroscience. 2nd edition.* Sunderland (MA): Sinauer Associates, 2001.

F.K.H. Quek and C. Kirbas. Vessel extraction in medical images by wave-propagation and traceback. *Medical Imaging, IEEE Transactions on*, 20(2):117–131, Feb 2001. ISSN 0278-0062. doi: 10.1109/42.913178.

H.A. Quigley and A.T. Broman. The number of people with glaucoma worldwide in 2010 and 2020. *British Journal of Ophthalmology*, 90(3):262–267, 2006. doi: 10.1136/bjo.2005.081224.

A.S.C. Reis, N. O'Leary, H. Yang, G.P. Sharpe, M.T. Nicolela, C.F. Burgoyne, and B.C. Chauhan. Influence of clinically invisible, but optical coherence tomography detected, optic disc margin anatomy on neuroretinal rim evaluation clinically invisible optic disc margin anatomy. *Investigative Ophthalmology and Visual Science*, 53(4):1852, 2012. doi: 10.1167/iovs.11-9309.

C.C. Reyes-Aldasoro and A. Bhalerao. The bhattacharyya space for feature selection and its application to texture segmentation. *Pattern Recogn.*, 39(5):812–826, May 2006. ISSN 0031-3203. doi: 10.1016/j.patcog.2005.12.003.

S. Ricco, M. Chen, H. Ishikawa, G. Wollstein, and J. Schuman. Correcting motion artifacts in retinal spectral domain optical coherence tomography via image registration. In G.-Z. Yang, D. Hawkes, D. Rueckert, A. Noble, and C. Taylor, editors, *Medical Image Computing and Computer-Assisted Intervention – MICCAI 2009*, volume 5761 of *Lecture Notes in Computer Science*, pages 100–107. Springer Berlin Heidelberg, 2009. ISBN 978-3-642-04267-6. doi: 10.1007/978-3-642-04268-3_13.

F. Rossant, I. Ghorbel, I. Bloch, and et al. Automated segmentation of retinal layers in oct imaging and derived ophthalmic measures. *Biomedical Imaging*, pages 1370 – 1373, 2009a.

F. Rossant, I. Ghorbel, I. Bloch, M. Paques, and S. Tick. Automated segmentation of retinal layers in oct imaging and derived ophthalmic measures. In *Biomedical Imaging: From Nano to Macro, 2009. ISBI '09. IEEE International Symposium on*, pages 1370–1373, June 2009b. doi: 10.1109/ISBI.2009.5193320.

S. Saidha, S.B. Syc, M.A. Ibrahim, C. Eckstein, C.V. Warner, S.K. Farrell, J.D. Oakley, M.K. Durbin, S.A. Meyer, L.J. Balcer, E.M. Frohman, J.M. Rosenzweig, S.D. Newsome, J.N.

Ratchford, Q.D. Nguyen, and P.A. Calabresi. Primary retinal pathology in multiple sclerosis as detected by optical coherence tomography. *Brain*, 134(2):518–533, 2011. ISSN 0006-8950. doi: 10.1093/brain/awq346.

R.E. Sakai, D.J. Feller, K.M. Galetta, S.L. Galetta, and L.J. Balcer. Vision in multiple sclerosis: The story, structure-function correlations, and models for neuroprotection. *Journal of Neuro-Ophthalmology*, 31(4), 2011. ISSN 1070-8022. 00020.

E. Schneider, H. Zimmermann, T. Oberwahrenbrock, F. Kaufhold, E.M. Kadas, A. Petzold, F. Bilger, N. Borisow, S. Jarius, B. Wildemann, K. Ruprecht, A.U. Brandt, and F. Paul. Optical coherence tomography reveals distinct patterns of retinal damage in neuromyelitis optica and multiple sclerosis. *PLoS ONE*, 8(6), 2013. doi: 10.1371/journal.pone.0066151.

J.S. Schuman. Spectral Domain Optical Coherence Tomography for Glaucoma. *Transactions of the American Ophthalmological Society*, (106):426–458, 2008.

C.J. Scott, R.H. Kardon, A.G. Lee, L. Frisén, and M. Wall. Diagnosis and grading of papilledema in patients with raised intracranial pressure using optical coherence tomography vs clinical expert assessment using a clinical staging scale. *Archives of Ophthalmology*, 128(6): 705–711, 2010. doi: 10.1001/archophthalmol.2010.94.

J.V.B. Soares, J.J.G. Leandro, R.M. Cesar, H.F. Jelinek, and M.J. Cree. Retinal vessel segmentation using the 2-d morlet wavelet and supervised classification. *Medical Imaging, IEEE Transactions on*, 25(9):1214–1222, Sept 2006. ISSN 0278-0062. doi: 10.1109/TMI.2006.879967.

M. Sofka and C.V. Stewart. Retinal vessel centerline extraction using multiscale matched filters, confidence and edge measures. *IEEE Transactions on Medical Imaging*, 25(12):1531–1546, Dec 2006. ISSN 0278-0062. doi: 10.1109/TMI.2006.884190.

J. Staal, M.D. Abràmoff, M. Niemeijer, M.A. Viergever, and B. van Ginneken. Ridge-based vessel segmentation in color images of the retina. *Medical Imaging, IEEE Transactions on*, 23(4):501–509, April 2004. ISSN 0278-0062. doi: 10.1109/TMI.2004.825627.

U.S. National Institutes of Health STARE. Structured analysis of the retina. URL `http://www.ces.clemson.edu/~ahoover/stare/`.

Stedman'sMedicalDictionary. The american heritage stedman's medical dictionary. Jul 2015.

N.G. Strouthidis, H. Yang, J.F. Reynaud, J.L. Grimm, S.K. Gardiner, B. Fortune, and C.F. Burgoyne. Comparison of clinical and spectral domain optical coherence tomography optic disc margin anatomy. *Investigative Ophthalmology and Visual Science*, 50(10):4709, 2009a. doi: 10.1167/iovs.09-3586.

N.G. Strouthidis, H. Yang, J.F. Reynaud, J.L. Grimm, S.K. Gardiner, B. Fortune, and C.F. Burgoyne. Comparison of clinical and spectral domain optical coherence tomography optic disc margin anatomy. *Investigative Ophthalmology and Visual Science*, 50(10):4709, 2009b. doi: 10.1167/iovs.09-3586.

C. Sun, G. Liew, J.J. Wang, P. Mitchell, S.M. Saw, T. Aung, E.S. Tai, and T.Y. Wong. Retinal vascular caliber, blood pressure, and cardiovascular risk factors in an asian population: The singapore malay eye study. *Investigative Ophthalmology and Visual Science*, 49(5):1784, 2008. doi: 10.1167/iovs.07-1450.

S.B. Syc, S. Saidha, S.D. Newsome, J.N. Ratchford, M. Levy, Ford E'Tona, C.M. Crainiceanu, M.K. Durbin, J.D. Oaklex, S.A. Meyer, E.M. Frohman, and P.A. Calabresi. Optical coherence tomography segmentation reveals ganglion cell layer pathology after optic neuritis. *Brain*, 135(2):521–533, 2012. ISSN 0006-8950. doi: 10.1093/brain/awr264.

L.S. Talman, E.R. Bisker, D.J. Sackel, D.A. Long, K.M. Galetta, J.N. Ratchford, D.J. Lile, S.K. Farrell, M.J. Loguidice, G. Remington, A. Conger, T.C. Frohman, D.A. Jacobs, C.E. Markowitz, G.R. Cutter, G.-S. Ying, Y. Dai, M.G. Maguire, S.L. Galetta, E.M. Frohman, P.A. Calabresi, and L.J. Balcer. Longitudinal study of vision and retinal nerve fiber layer thickness in multiple sclerosis. *Annals of Neurology*, 67(6):749–760, 2010. ISSN 1531-8249. doi: 10.1002/ana.22005.

UTHMedicalSchool. Neuroscience online. URL `http://neuroscience.uth.tmc.edu/index.htm`.

A. Vasilevskiy and K. Siddiqi. Flux maximizing geometric flows. *Pattern Analysis and Machine Intelligence, IEEE Transactions on*, 24(12):1565–1578, Dec 2002. ISSN 0162-8828. doi: 10.1109/TPAMI.2002.1114849.

V. Vezhnevets and V. Konouchine. Grow-cut - interactive multi-label n-d image segmentation. *Graphicon*, pages 150–156, 2005.

J. Weickert. Coherence-enhancing diffusion filtering. *International Journal of Computer Vision*, 31(2-3):111–127, 1999. ISSN 0920-5691. doi: 10.1023/A:1008009714131.

J. Weickert, S. Ishikawa, and A. Imiya. Linear scale-space has first been proposed in japan. *Journal of Mathematical Imaging and Vision*, 10(3):237–252, 1999. ISSN 0924-9907. doi: 10.1023/A:1008344623873.

A.P. Witkin. Scale-space filtering. In *Proceedings of the Eighth International Joint Conference on Artificial Intelligence - Volume 2*, IJCAI'83, pages 1019–1022, San Francisco, CA, USA, 1983. Morgan Kaufmann Publishers Inc.

W.H. Woon, F.W. Fitzke, A.C. Bird, and J. Marshall. Confocal imaging of the fundus using a scanning laser ophthalmoscope. *British Journal of Ophthalmology*, 76(8):470, 1992.

J. Xu, O. Chutatape, C. Zheng, and P.C.T. Kuan. Three dimensional optic disc visualisation from stereo images via dual registration and ocular media optical correction. *British Journal of Ophthalmology*, 90(2):181–185, 2006. doi: 10.1136/bjo.2005.082313.

J. Xu, H. Ishikawa, G. Wollstein, and J.S. Schuman. Retinal vessel segmentation on slo image. In *Engineering in Medicine and Biology Society, 2008. EMBS 2008. 30th Annual International Conference of the IEEE*, pages 2258–2261, Aug 2008. doi: 10.1109/IEMBS.2008.4649646.

R.A. Young. The gaussian derivative model for spatial vision: I. retinal mechanisms. *Spatial Vision*, 2(4):273–293, 1987.

Y. Yu, Z. Li, B. Liu, and X. Liu. An adaptive unimodal and hysteresis thresholding method. In Linqiang Pan, Gheorghe Păun, Mario J. Pérez-Jiménez, and Tao Song, editors, *Bio-Inspired Computing - Theories and Applications*, volume 472 of *Communications in Computer and Information Science*, pages 552–556. Springer Berlin Heidelberg, 2014. ISBN 978-3-662-45048-2. doi: 10.1007/978-3-662-45049-9_90.

B. Zhang, L. Zhang, L. Zhang, and F. Karray. Retinal vessel extraction by matched filter with first-order derivative of gaussian. *Computers in Biology and Medicine*, 40(4):438–445, 2015. doi: 10.1016/j.compbiomed.2010.02.008.

Y. Zheng, M. Grossman, S.P. Awate, and J.C. Gee. Automatic correction of intensity nonuniformity from sparseness of gradient distribution in medical images. In Guang-Zhong Yang, David Hawkes, Daniel Rueckert, Alison Noble, and Chris Taylor, editors, *Medical Image Computing and Computer-Assisted Intervention – MICCAI 2009*, volume 5762 of *Lecture Notes in Computer Science*, pages 852–859. Springer Berlin Heidelberg, 2009. ISBN 978-3-642-04270-6. doi: 10.1007/978-3-642-04271-3_103.

L. Zhu, I. Kolesov, Y. Gao, R. Kikinis, and A. Tannenbaum. An effective interactive medical image segmentation method using fast growcut. *MICCAI Workshop on Interactive Medical Image Computing*, 2014.

H. Zimmermann, A. Freing, F. Kaufhold, G. Gaede, E. Bohn, M. Bock, T. Oberwahrenbrock, K.-L. Young, J. Dörr, J. T Wuerfel, S. Schippling, F. Paul, and A.U. Brandt. Optic neuritis interferes with optical coherence tomography and magnetic resonance imaging correlations. *Multiple Sclerosis Journal*, 19(4):443–450, 2013. doi: 10.1177/1352458512457844.

H. Zimmermann, T. Oberwahrenbrock, A.U. Brandt, F. Paul, and Dörr J. Optical coherence tomography for retinal imaging in multiple sclerosis. *DovePress*, 4:153–162, 2014.

K. Zuiderveld. Graphics gems iv. chapter Contrast Limited Adaptive Histogram Equalization, pages 474–485. Academic Press Professional, Inc., San Diego, CA, USA, 1994. ISBN 0-12-336155-9.

Selbständigkeitserklärung

Gemäß §7 (4) der Promotionsordnung versichere ich hiermit, diese Arbeit selbständig verfasst zu haben. Ich habe alle bei der Erstellung dieser Arbeit benutzten Hilfsmittel und Hilfen angegeben. Diese Arbeit habe ich in keinem früheren Promotionsverfahren eingereicht.

Zusammenfassung

In der Retina, die dem zentralen Nervensystem zugeordnet wird, finden sich viele Zellarten und Strukturen, die auch im Gehirn vorkommen. Daher spielt die Erkennung struktureller Veränderungen der Retina eine wichtige Rolle in der Diagnose vieler neurologischer Erkrankungen. In den letzten Jahren haben innovative optische Verfahren die Bildgebung am Auge optimiert und ermöglichen die Erkennung solcher retinaler Veränderungen. Besonders die optische Kohärenztomographie hat sich als nützliches Bildgebungswerkzeug vor allem in der Augenheilkunde etabliert. OCT ist ein nicht-invasives Verfahren, welches in-vivo Aufnahmen von biologischem Gewebe und damit dreidimensionale (3D) Tiefenscans der Retina ermöglicht. Auf einen solchen 3D OCT Scan können 3D Modellierung und Detektionsmechanismen anwendet werden, um eine für den Anwender intuitivere Visualisierung und Quantifizierung der Strukturen zu erstellen, ähnlich wie 3D Verfahren für die Auswertung von Magnetresonanztomographie oder Computertomographieaufnahmen.

Derzeit wird OCT jedoch vor allem in der Diagnose und Quantifizierung ophthalmologischer Erkrankungen der Netzhaut genutzt, die Geräte bieten nur begrenzte Analyseverfahren, die sich für die Beurteilung der Veränderungen durch neurologische Erkrankungen eignen. Daher liegt der Fokus dieser Arbeit in der Entwicklung von neuen Segmentations und Analyseverfahren für die Quantifizierung zweier Bestandteile der Retina: Die retinalen Blutgefäße auf zweidimensionalen Konfokalen Scanning Laser Ophthalmoskopaufnahmen (cSLO), und den Sehnervenkopf (Optic nerve head, ONH) aus 3D OCT Volumenaufnahmen. Die Schwierigkeit in der Entwicklung robuster und akkurater Methoden für die Erkennung dieser Strukturen liegt in der Heterogenität der Daten, welche durch die natürliche anatomische Vielfalt, Artefakte während der Aufnahme, besonders bei Patienten im Vergleich zu gesunden Kontrollen, und vor allem wegen bestimmter struktureller Veränderungen im Krankheitsverlauf entsteht.

Wir präsentieren vier Ansätze für die Extrahierung von Eigenschaften der retinalen Vaskularisierung und des ONH in Multipler Sklerose, Neuromyelitis Optica Spektrum-erkrankungen und idiopatisch erhöhtem Hirndruck. Die ersten beiden Ansätze konzentrieren sich auf die Erkennung der Blutgefäße im SLO Bild. Wir stellen ein neues 2D Model des Gefäßprofils vor, welches den auf diesen Aufnahmen sichtbaren Zentralreflex der Gefäße miteinbezieht, um so den inneren und äußeren Gefäßdurchmesser zu quantifizieren. Darüber hinaus haben wir neue

Filter für die Hervorhebung der Blutgefäße, basierend auf Morlet-Wavelet, dem Hesse-Tensor und einem gerichteter Fluss-Ansatz, entwickelt und ihre Eignung für die korrekte Erkennung von inneren und äußeren Gefäßrändern und Krümmung der Blutgefäße, auch in Verzweigungen, geprüft. Für den ONH präsentieren wir einen robusten Ansatz für die Berechnung einer Referenz-oberfläche zur Volumenberechnung bei Schwellung und Atrophie. Zudem präsentieren wir einen neuen Algorithmus für die Erkennung des ONH Zentrums direkt im 3D Volumen. Die Grundidee der Methode ist die Nutzung von Informationen, die aus der Referenzoberfläche gewonnen wurden, um die Berechnung auf ein Sub-volumen um den ONH zu reduzieren. Darüber hinaus konnten wir mehrere Artefakte, die in unseren Daten zu finden waren, korrigieren: Bewegungsartefakte wegen Augen- und/oder Kopfbewegungen durch Nutzung eines modifizierten Thin Plate Spline Fittings, welches in der Lage ist die natürliche Krümmung der Retina zu modellieren, und durch Blutgefäße entstandene Schattenartefakte durch Texturanalyse mit einem Grow-cut Algorithmus.

Um die Effektivität unserer neuen Methoden zu zeigen, wurden sie in Studien mit verschiedenen Patientengruppen sowie gesunden Kontrollen angewendet.